Lightweight online Kalman-filter-based sensitivity estimator for distribution grids utilizing phasor measurements

Niek Sterenborg

October 27, 2023

University of Twente

Faculty of Electrical Engineering, Mathematics and Computer Science (EEMSC)
Computer Architecture for Embedded Systems (CAES) group

Lightweight online Kalman-filter-based sensitivity estimator for distribution grids utilizing phasor measurements

Niek Sterenborg

Master's Thesis: Electical Engineering (EE), Dependable Integrated Systems (DIS)

1. Supervisor A.R. Vadavathi Msc.
Mathematics of Operations Research (MOR)
University of Twente

2. Supervisor Dr. ir. G. Hoogsteen
Computer Architecture for Embedded Systems (CAES) /
Mathematics of Operations Research (MOR)
University of Twente

Chair Dr. ir. M.E.T. Gerards
Computer Architecture for Embedded Systems (CAES)
University of Twente

External member Dr. ir. D.J.G. Moonen
Power Electronics (PE)
University of Twente

October 27, 2023

Niek Sterenborg
Lightweight online Kalman-filter-based sensitivity estimator for distribution grids utilizing phasor measurements
October 27, 2023
Committee:
A.R. Vadavathi Msc.,
Dr. ir. G. Hoogsteen,
Dr. ir. M.E.T. Gerards, and
Dr. ir. D.J.G. Moonen

University of Twente
Computer Architecture for Embedded Systems (CAES) group
Faculty of Electrical Engineering, Mathematics and Computer Science (EEMSC)
Drienerlolaan 5
7522 NB and Enschede

Abstract

In recent years, the energy transition is posing new challenges for the Dutch electricity grid and its operation. The rapid increase in the number of small scale renewable energy sources (RESs) such as photovoltaics (PVs) has a significant effect on the electricity network. Under specific scenarios, the power generation from these devices can be so large that the grid capacity is exceeded which necessitates advanced control solutions. In residential areas, the lack of synchronisation between peak consumption and peak production of electrical energy can result in high currents flowing back into the grid, which in turn leads to an increase in local voltage levels. Since the structure of the electricity grid was not designed with these current in mind, this increase in voltage can exceed grid codes. The problem of an increasing voltage becomes worse with physical distance to the transformer, which may lead to unfair situations where prosumers further away from the transformer can generate less power compared to closer prosumers. Fair control mechanisms for this problem are an active area of research, and often require information on the surrounding low voltage (LV) grid. As this data is frequently unavailable, algorithms that can estimate it become essential.

This thesis introduces a lightweight sensitivity estimator designed for the implementation of fair curtailment algorithms. The estimator's primary objective is to estimate grid parameters based on phasor measurements, utilizing GPS-synchronized, real-time data. The design prioritizes computational efficiency to minimize implementation costs. To achieve this, a Kalman filter approach is employed, ensuring that the estimator operates autonomously without user intervention.

The performance of the estimator is compared to a benchmark method, and ground truth data. Using the sensitivity estimation, the voltage prediction is only up to $38mV$ RMS more compared to the ground truth voltage prediction. With this marginal increase in prediction error, this estimator presents a viable solution for applications like PV inverters, where user interaction cannot be relied upon.

Dankwoord

Het is al weer goed zeven jaar geleden dat ik begonnen ben met mijn studie, en nu zit ik met een tevreden gevoel dit dankwoord te schrijven. Na het afronden van de bachelor ging ik verder met de master, waarvan deze thesis het einde markeerd. Via deze weg wil ik iedereen die mij tijdens mijn studie periode heeft geholpen bedanken.

First of all, I would like to thank my supervisors Gerwin and Aswin for all discussions and meetings we had to bring this thesis to a successful ending. Gerwin, jou enthausiasme over het onderwerp en brede blik op de problematiek waren mede verantwoordelijk voor mijn keuze voor deze opdracht, en als ik tegen problemen aan liep wist jij vaak direct een suggestie in de goeie richting te geven. Aswin, working towards solutions for an implementation of your algorithm was a priviledge, I wish you the best for the future of your research.

Besides my daily supervisors, I would like to extend my thanks to all other colleagues at CAES and *the energygroup*. I enjoyed the coffee breaks, where my eyes were opened to sweet and savory snacks from all-around the world and dry jokes could be made (and were made) about any conversation topic.

Mijn dank gaat ook uit naar Dennis, die namens Smart State Technology het sensorbeheer voor het onderzoeksproject in handen heeft. Elk probleem waar ik tegen aan liep was maar een mailtje verwijderd van een oplossing, zo maakte je het complexe systeem werkbaar voor me.

Verder wil ik mijn studievrienden bedanken voor onze gezellige tijd samen. Ondanks mijn volle agenda en onze lange-afstand-relatie-achtige band heb ik herinneringen met jullie gemaakt die me mijn hele leven bij zullen blijven, en ik kan niet wachten om er een heleboel meer bij te maken.

Pap, mam, Koen, natuurlijk wil ik ook jullie bedanken. Jullie hebben mij de mogelijkheid gegeven om mijn studie te volgen, en hebben me gesteund in al mijn beslissingen. Ik kan ik jullie inhoudelijk niet altijd alles uitleggen wat ik uit spook, maar jullie hadden altijd belangstelling naar de voortgang, en ik heb het dankzij júllie basis zo ver weten te schoppen.

Tot slot wil ik Paulien bedanken. Jij doorstaat mijn chaotische studentenleven al een aantal jaar en staat achter al mijn keuzes, ongeacht wat ze voor jou betekenen. Paulien, je bent mijn vaste rots in de branding, en nog lang niet van me af.

Contents

Introduction

1

Historically, the LV electricity grid in the Netherlands has a radial structure where power is centrally generated by large power plants connected to the high voltage (HV) and medium voltage (MV) grids[1]. In this situation, power only flows from there to consumers on the MV and LV grids. Recently, the energy transition has resulted in a fundamental change in the power flow however [2]–[4]. Due to the increase in smaller scale RESs (e.g. PV or wind generation) connected to the MV and LV grid, a shift towards decentralised energy generation can be observed. This shift implies that power now has to flow in both directions in the grid. Small amounts of return currentpose not problems to the the existing electricity grid, however the increasing number of electrical devices both that produce energy on a local level has resulted in a significantly increased power injection into the grid which does pose challenges. In the Netherlands, the number and severity of congestion problems is already rising due to an increase in renewable distributed energy resources (DERs) in residential areas [5], [6]. This effect is amplified even more due to the inflexible nature of RESs compared to traditional power generators. Since the electricity grid has very little storage capacity, production and consumption has to be balanced continuously. If this balance is not maintained, blackouts will occur due to the changing grid frequency [7]. Traditionally centralised power plants provide ancillary services to achieve this balance, since their power output can be regulated to follow the energy demand. Energy generation by turbines and solar farms however greatly depends on the weather and time of the day, resulting in a bigger challenge when maintaining the grid balance when they take up an increasing share of the energy generation. Furthermore, balancing the grid from a central generation perspective is easier since global power demands can be predicted more precisely than local demands. On the global scale, deviations in power demand cancel with one another whereas on a local scale a single device turning on or off can result in a relatively large change in power demand.

An additional challenge with residential PV generation is in the mismatch of peak PV-production compared to the peak power consumption, illustrated in figure 1.1. It can be observed that during night hours from 00:00 to 06:00 the power consumption is relatively low, which can be expected. During the day, the power demand increases, with an observable peak around 20:00. Furthermore, the energy consumption is higher in darker, colder months, as more energy is required for heating and lighting. Figure 1.1b shows an average of the solar irridiance in recent years. Solar irridiance is low in the night, and peaks slightly after noon. Furthermore, it is highest in the summer months and lower winter months. Figures 1.1a and 1.1b illustrate the lack of synchronisation between solar energy generation and energy consumption in residential areas. Since the timing of peak solar generation is at a point at which residential electricity demand is relatively low, locally generated power can exceed power demands resulting in current flowing back into the grid. Even more so; the reverse flow can be much higher than the load for which the grid was originally designed.

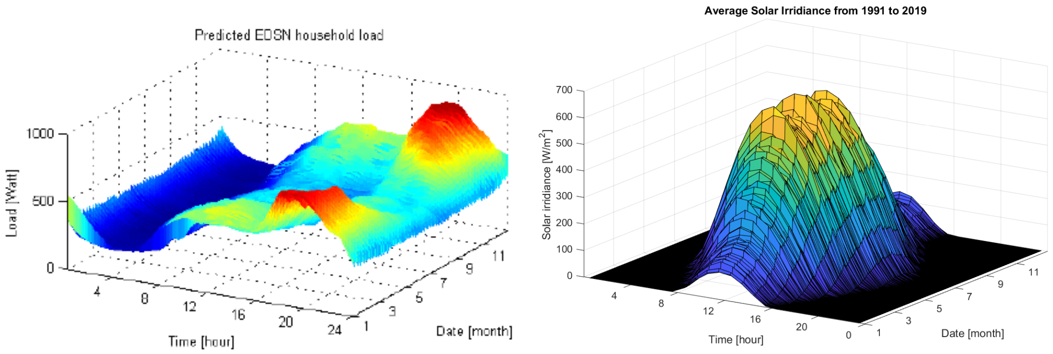

(a) Load profile of an average 3.500 kWh residential connection. Figure taken from[8]

(b) Average solar irridiance in Gelderland from 1991 to 2019. Data obtained from TU Delft's meteorological data portal[9]

Fig. 1.1.: Comparison between residential load profile and solar irridiance profile

When current flows back into the grid, local grid voltages increase. Grid codes pose an upper limit to this increase in voltage. When PV-production is high enough, this upper limit can be exceeded if no control mechanism is in place to enforce it. Next to physical limitations, PV inverters are required by law to turn off if they detect and overvoltage [10] which is often not necessary. Power generation can be curtailed instead, to minimize the loss in production. Mechanisms that curtail energy production instead of completely turning the inverter off do exist, however they often lack the ability to solve the bigger issue on the scale of the local distribution grid. Changing the power at a certain node affects the voltage at all other nodes on the feeder. In situations where multiple PV-installations are connected to the same feeder, the situation can be unfair among prosumers since the voltage increase becomes more severe with greater physical distance from the transformer. Installations located at the end of the feeder are curtailed more than installations that are closer to the transformer. Especially in the countryside, where distances between connected farms are larger, and PV-installations are sometimes part of a business plan, unfair curtailment can be very problematic.

Solutions that curtail power generation fairly among prosumers are therefore an active topic of research. The techniques that are used for fair curtailment require some degree of knowledge on the local grid layout and parameters. Their methods need to know how the nodes in the system are affected by power generation changes at other nodes. This requires knowledge on the grid layout, as well as the grid parameters like impedance. This information is often difficult to obtain, or even unavailable altogether. Curtailment mechanisms that try to control the fairness as well as the voltage therefore call for additional, real-time measurements and algorithms that are able to estimate this grid layout information. This thesis covers such an estimation method to obtain local grid parameters.

1.1 Thesis applications

The problem addressed in this thesis is the estimation of required grid parameters in the application of residential . This is done within the scope of a research project titled *Fairplay*, which is an ongoing project with collaboration of the University of Twente and other partners. In this project, the fairness in PV-curtailment across connections on a single feeder is investigated, and curtailment is done as fair as possible. A test-site is available near Markelo, a village in the East of the Netherlands as part of the project. The LV-feeder that connects multiple farms with PV-installations is monitored, and can be used to test any theories.

The goal of this thesis is to contribute towards the fair control method developed for this project [11] by providing the estimated grid parameters. The control method is based on sensitivity i.e. the change in voltage at some node in the network as a result of the change in power at another (or the same) node. With the sensitivity, the change in voltage can be predicted for a given change in power, which is the core concept of fair curtailment techniques. Essentially, this sensitivity unveils the relation between grid nodes and hence the properties of the LV grid. Since the parameter estimation method of this thesis is intended for use at the inverter, the assumption is made that phasor measurement unit (PMU)-measurements are available. PMUs have been used in transmission grids for a longer time, and are now becoming more and more popular in distribution grids as well due to the challenges that come with the adoption of RES smart grid and the electrification. The phasor information is used to make estimations on local grid parameters. One of the project partners, Smart State Technology (SST) [12], provides the PMUs that are used in this thesis. This measurement system is explained in more detail in Chapter 3. Furthermore, if multiple estimators are present at different nodes in a local grid, it is assumed for the content of this research that they are able to communicate and that measurement samples are synchronized among sensors. Together they are able to estimate more grid parameters.

1.2 Research questions

The problem illustrated above calls for an estimator that is able to determine the sensitivity in LV grids with PV connections. The goal is for the estimator to be installed and function in real time (i.e. online) with no additional required user interaction. The main research question this thesis addresses is therefore:

How can the sensitivity between residential distribution grid connections be accurately estimated in an online approach?

This problem is subdivided into the following sub-questions:

- How can the sensitivity parameter be modelled?
- What information is needed to estimate the sensitivity?
- How many samples are required to find an accurate estimation?
- To what degree of accuracy can the sensitivity be found by the estimator?
- What hardware is required to run the estimator online?

1.3 Thesis structure

The remainder of this thesis is subdivided in four chapters. First, **Chapter 2** presents background information and related work relevant to this thesis which can be used to address the first sub-question. **Chapter 3** explains the use-case of the thesis and elaborates on the practical implementation. This section describes the test location and the sensors that are used, and the data that they provide which is relevant for the second sub-question. Next, **Chapter 4** explains the design of the estimator and how it functions, and explains the validation method for the results of the estimator, after which **Chapter 5** presents the results of the estimator and compares them to benchmark results. The information of these two chapters is used to answer sub-questions three, four, and fife. Lastly, **Chapter 6** formulates the conclusions to the research questions introduced in Section 1.2.

2 Background and Related Work

This section provides the background knowledge on which the content of this thesis is build. Furthermore, related work to the problem is presented here to put the thesis in perspective. First, some basic information about the electricity grid is presented in Section 2.1, the three-phase system is explained in Section 2.3, and the grid regulations are presented in Section 2.2. Next, the overvoltage problem is explained in Section 2.4 and related work on a solution for it in Section 2.5. Section 2.6 presents parameter and state estimation techniques, and Section 2.7 presents filtering techniques related to estimators. Lastly, Section 2.8 summarizes and concludes this chapter.

2.1 Grid structure

To understand the problem addressed in this thesis, knowledge on the structure of the electricity grid is required. Detailed background information on the Dutch electricity grid is provided in [13]. Generally, the electricity network in the Netherlands consists of the following distinct parts.

- The *interconnection grid* handles transport of electrical energy on a national level. This interconnection also includes international connections to neighbouring countries.
- The *transmission grid* connects the interconnection grid to the distribution grids. Power plants, large turbine parks and very large industrial connections with powers of more than approximately 10 MVA are connected to this grid.
- The *regional distribution grids* are the third level in grid hierarchy. These grids traditionally receive power from the transmission grids. Connected to this grid are generators like wind turbines and heat-power plants with powers between 0.3 and 10 MVA. Furthermore it offers connections to large industrial consumers. This grid provides power to the local distribution grid.
- Lastly, the *local distribution grids* supply power to the smallest connections in terms of power. This grid includes all residential connections.

2.1.1 Grid topology

Different levels of the electricity grid have adopted different network topologies based on their usecase. In [13], these different topologies are also explained. The existing topologies are shown in Fig. 2.1. A radial network structure shown in Fig. 2.1a only branches out from the centre. Fig. 2.1b shows a ring-shaped network containing loops that connecting multiple branches together. Crucially, these loops are only connected at one point. Meshed grid topologies allow more of these connections so that the nodes are connected in a mesh structure as shown in Fig. 2.1c. Lastly, a meshed network can have an outlier like in Fig. 2.1d which can only be reached via one specific node.

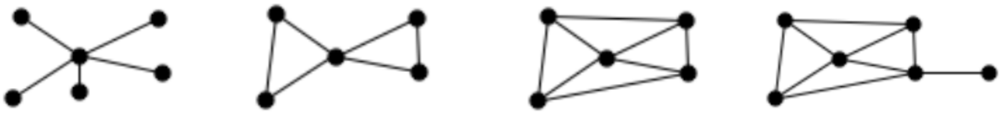

(a) Radial network

(b) Ring-shaped network

(c) Meshed network

(d) Outlier network

Fig. 2.1.: Different possible grid topologies (from [13])

Distribution grids in the Netherlands are generally radially operated like Fig. 2.1a, meaning that it branches out from the center and does not loop around. This is also illustrated in Fig. 2.2. In some older cities meshed networks still exist as a leftover from older electricity grids. The transmission and interconnection grid are of a meshed structure.

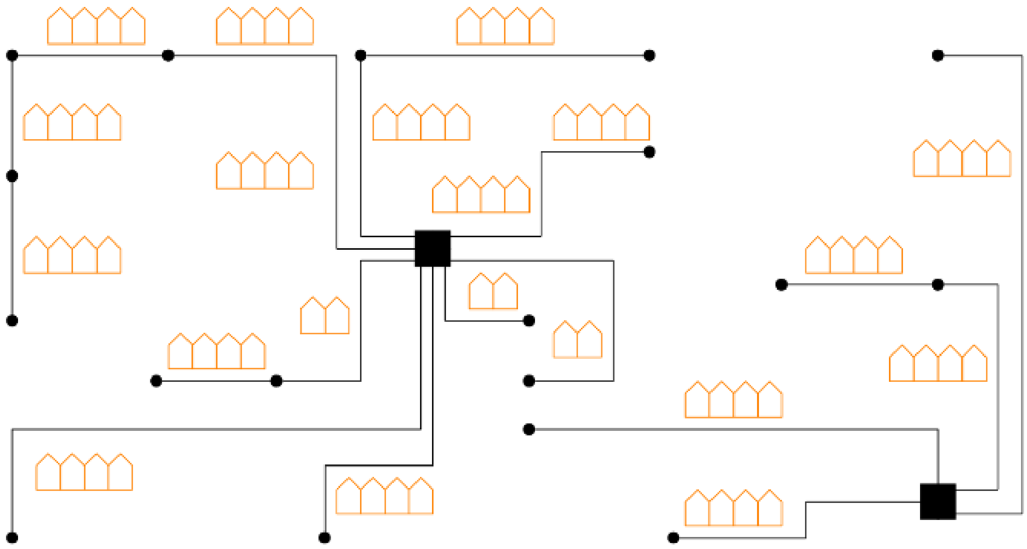

Fig. 2.2.: Structure of a LV-distribution grid in the Netherlands (from [13])

As can be seen in Fig. 2.2, houses connect to a feeder (illustrated with black dots on the black lines) which runs to a central transformer (illustrated as a black square). These feeders are never connected to other feeders. Traditionally, power was generated at a higher level, resulting in current flowing from the transformers to the consumers. With the energy transition, DER in residential areas introduce a shift in power flow, where power is generated locally, and any excess power is injected back into the grid through the transformer.

2.2 Electricity grid regulations

Devices connected to the grid rely on certain power quality (PQ) assumptions related to voltage level and balance across phases. In order to enforce PQ in the grid, distribution system operators (DSOs) have to ensure that distribution grids adhere to PQ-standards. The EN 50160 [14] specifies the requirements on PQ in Europe. It incorporates regulations for both voltage limits and phase unbalance. Specifically, the following regulations on PQ in LV networks apply:

Tab. 2.1.: PQ requirements as stated in NEN EN 50160 (from [14])

	Requirement
Voltage	- $U_{nom} \pm 10\%$ for 95% of 10 minute averages during one week - $U_{nom} \pm 10\%$ and -15% for all 10 minute averages during one week
Asymmetry	- The negative component of the voltage $< 2\%$ of the positive component for 95% of 10 minutes measurements during 1 week - The negative component of the voltage $< 3\%$ of the positive component for all 10 minutes measurements during 1 week

2.3 Three-phase system

The LV-grid in the Netherlands is a 50Hz , three-phase, alternating current (AC) system. This system consists of three sinusoidal voltages with a phase difference of $120°$ each. Fig. 2.3 depicts the three phase voltages over time (Fig. 2.3a) and as phasor representation (Fig. 2.3b).

If the angle between the three phasors is indeed $120°$ and the magnitude of the phasors is equal, the system is called a balanced system. In practice however, these phasors can differ from the theoretical definition due to differences in loads among phases. If the electrical load on phases is different the phase signals may be attenuated differently resulting in a difference in magnitude, or the angle may be

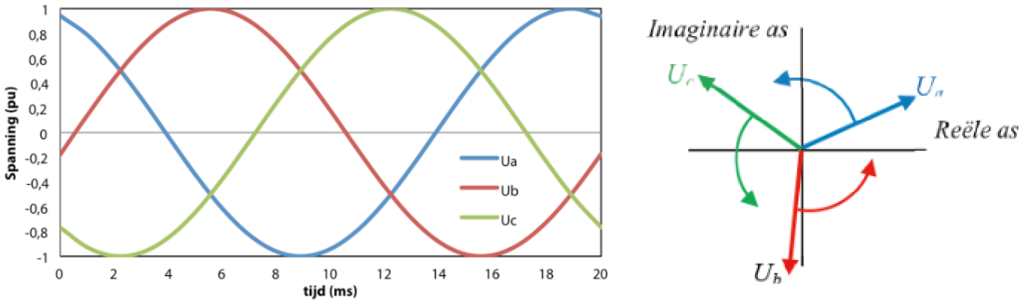

(a) Three phase signals over time

(b) Three-phase phasor representation

Fig. 2.3.: Three-phase system [13]

changed due to inductive or capacitive loads, resulting in uneven angles between the phasors. In a situation where the phasors are not equal, the system is called an unbalanced system.

2.3.1 Fortescue Transform

Analysis on unbalanced phasor systems is difficult. To make analysis on such systems possible, the Fortescue transform can be used as a simpler representation of the unbalanced system. In 1918, Charles Legeyt Fortescue presented the method to express any set of unbalanced phasors in symmetrical components [15]. The methods splits a power system into positive-, negative-, and zero-sequence components. The technique applies to any poly-phase system. Considering the example of a three-phase system, the voltage is subjected to transformation as:

$$V_{abc} = \begin{bmatrix} V_a \\ V_b \\ V_c \end{bmatrix} = \begin{bmatrix} V_{a,0} \\ V_{b,0} \\ V_{c,0} \end{bmatrix} + \begin{bmatrix} V_{a,1} \\ V_{b,1} \\ V_{c,1} \end{bmatrix} + \begin{bmatrix} V_{a,2} \\ V_{b,2} \\ V_{c,2} \end{bmatrix} \tag{2.1}$$

where a, b, and c represent the three phases and 0, 1, and 2 represent the zero-, positive-, and negative-component respectively. A phasor rotation operator α is then defined as:

$$\alpha = e^{\frac{2}{3}\pi i} \tag{2.2}$$

Note that, $\alpha^3 = 1$ and $\alpha^{-1} = \alpha^2$. The zero-sequence components are defined to have equal magnitude and the same angle:

$$V_0 = V_{a,0} = V_{b,0} = V_{c,0} \tag{2.3}$$

The positive-sequence components are defined to have equal magnitude and a $120°$ phase angle in the counterclockwise direction.

$$V_1 = V_{a,1} = \alpha V_{b,1} = \alpha^2 V_{c,1} \tag{2.4}$$

The negative-sequence components are defined to have equal magnitude and a $240°$ phase angle in the counterclockwise direction.

$$V_2 = V_{a,2} = \alpha^2 V_{b,2} = \alpha V_{c,2} \tag{2.5}$$

Fig. 2.4 gives a visual phasor representation of the sequence components.

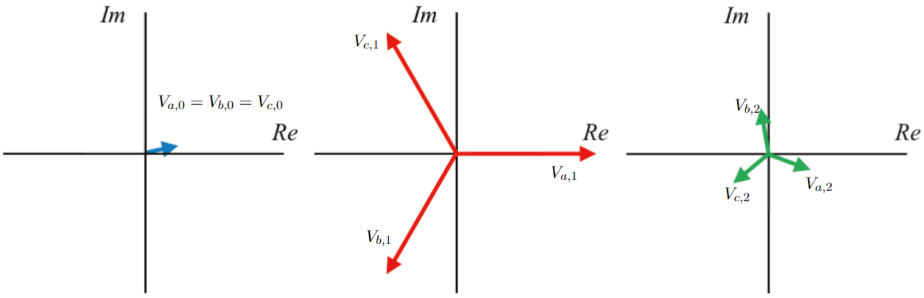

Fig. 2.4.: Visual representation of sequence components [13]

With the sequence components defined, V_{abc} can be written as:

$$V_{abc} = \begin{bmatrix} V_0 \\ V_0 \\ V_0 \end{bmatrix} + \begin{bmatrix} V_1 \\ \alpha^2 V_1 \\ \alpha V_1 \end{bmatrix} + \begin{bmatrix} V_2 \\ \alpha V_2 \\ \alpha^2 V_2 \end{bmatrix} = \begin{bmatrix} 1 & 1 & 1 \\ 1 & \alpha^2 & \alpha \\ 1 & \alpha & \alpha^2 \end{bmatrix} \begin{bmatrix} V_0 \\ V_1 \\ V_2 \end{bmatrix} \tag{2.6}$$

An example of how this would look is shown in Fig. 2.5.

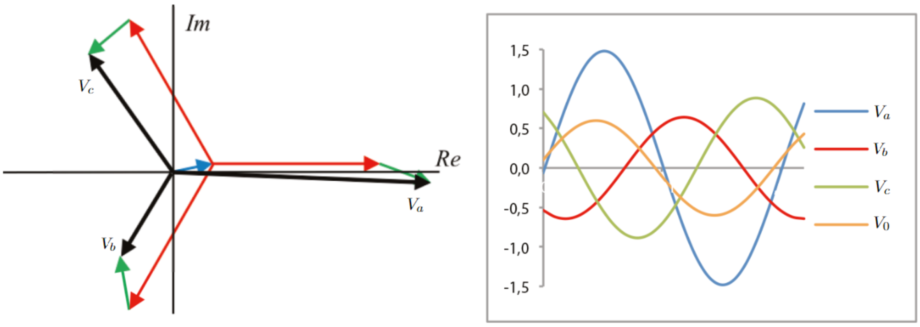

Fig. 2.5.: Visual representation of unbalanced system[13]

As depicted in Fig. 2.5, the unbalanced system is represented by a set of sequence components that have equal magnitude for all phases, and only differ in angle. In Fig. 2.5, V_0 is also illustrated. In an unbalanced system, the neutral current increases as the unbalance increases since the phase currents cancel with each other in the neutral conductor in a balanced system.

2.4 Overvoltage problem

As explained in Section 1, the mismatch in time between peak solar generation and peak power demand causes power to flow into the grid during periods of high production. This can cause problems in local LV-grids where the maximum voltage exceeds network limits. Fig. 2.6 shows a generic model of a LV-grid with houses connected to a LV-feeder.

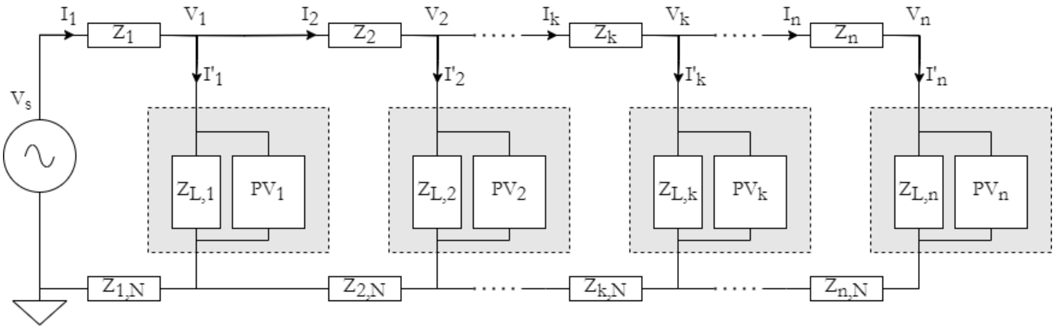

Fig. 2.6.: Local LV grid model

With the LV-grid model shown in Fig. 2.6 the overvoltage problem can be illustrated. In Fig. 2.6, V_s is the transformers voltage, Z_i represents the feeder impedance between neighbouring houses, $Z_{i,N}$ the neutral feeder impedance, $Z_{L,i}$ represents the impedance of a house to ground, which represents power consumption at a certain point in time, and PV_i represents the PV-installation of a connection i. During periods of high solar production and low load, the power consumed by a house is lower than the power generated by the PV-installation resulting in current flowing from the houses back to the transformer ($I_i < 0$). Using Kirchhoff's current law (KCL) and Kirchhoff's voltage law (KVL) it can be found that this creates an increase in voltage at the houses due to the feeder impedance, for instance the voltage increase at V_1 as an effect of a negative I_2 current can be found with:

$$V_1 = V_s - Z_1 I_1 \tag{2.7}$$

where:

$$I_1 = I_1' + I_2 \tag{2.8}$$

Combining Equations 2.7 and 2.8 gives:

$$V_1 = V_s - Z_1 \left(I_1' + I_2\right) \tag{2.9}$$

In Equation 2.9, it can be seen that for a given I_1', V_1 changes due to changes in I_2 proportional to Z_1, and that negative I_2 currents result in an increase in voltage.

This problem is most severe in rural LV-grids since the cable impedance is high due to larger distance between connections. Furthermore, houses at the end of the LV-feeder have a distinct disadvantage compared to houses close to the transformer. The increase in voltage is more severe at the end of the feeder due to the larger feeder impedance from the connection to the transformer.

With an increasing PV-penetration in local grids, current injected in the grid also increases. This in turn increase the voltage more and more, to a point where the grid limits explained in Section 2.2 are exceeded. Currently, PV-inverters often turn off when this voltage limit is reached to ensure that the grid regulations are enforced. This approach has two disadvantages however. First, the inverter generally does not have to turn off but a reduction in power generation can be sufficient. Section 2.5 will explain this in more detail. Second, since the voltage increases with distance to the transformer, PV-installations towards the end of the feeder will shut off or curtail power generation first. This causes unfair production between neighbouring prosumers.

2.5 Techniques for voltage regulation

The ideal solution to the overvoltage problem is to reduce feeder impedance, so that any excess solar power that cannot be consumed locally can be distributed for consumption elsewhere. This can be achieved by utilizing thicker cables, or multiple cables in parallel. This solution is however very costly and time-consuming to implement. Another solution is to implement local energy storage to reduce current in the feeder and move electricity in time to where it is consumed. Various research is being done on residential energy storage [16], [17]. While results in this direction are promising, storage solutions are also costly to implement. The cost of batteries for instance adds to the cost of the total system, increasing the cost of investment for customers.

A cost-effective solution is to reduce the output power of PV inverters when grid limits are exceeded. This is often called active power curtailment (APC), which requires an algorithm that minimizes curtailment, but keeps the grid within the allowed limits. Some applications of APC will be discussed here.

In both [18] and [19], a reactive power based control strategy is proposed to regulate the grid voltage. They only take into account single-phase inverters however, and requires a 10% over-sizing ratio of the PV inverters. Furthermore, voltage control based methods outperform reactive power based methods since the distribution network is more sensitive to changes in active power due to the high R/X ratio [20], [21]. A method based on optimal power flow (OPF) is proposed in [22]. This method minimizes energy loss, making it an efficient solution if variations in power delivery across multiple PV inverters is not an issue.

Previously mentioned regulation methods [18], [19], [22] achieve their goal of adhering to voltage regulations by reducing solar power, however they all fail to curtail individual PV installations equally. Prosumers in more sensitive parts of the grid are curtailed more, making these algorithms unfair to some prosumers. Solutions to this unfairness problem exist in the form of methods that regulate the power generation while keeping this fairness among prosumers in mind. These methods divide curtailment among contributing parties, and often work at the cost of some additional curtailment [23]. These methods are more suited for residential areas where stakeholders could otherwise be at a distinct disadvantage compared to their neighbours.

[24] proposes a method to distribute curtailment fairly across all prosumers. The method uses droop control to achieve this, and is able to realize fair curtailment. [25] adopts a decentralized *volt-watt* and *volt-var* control scheme with equal curves for all connections to enforce fairness. Various OPF-based methods are proposed in [26]. It also uses Jain's fairness index [27] to assess the achieved fairness of multiple methods. While [24], [25], and [26] all achieve some degree of fairness among prosumers, the energy loss of the APC methods is higher compared to other, non-fair methods.

This research aims to contribute to the APC method proposed in [11] which is a fair APC method that also aims to balance the phases in the grid. The method combines overvoltage control with neutral current compensation and achieves a balanced grid with fair curtailments among prosumers. For an implementation of this method, knowledge of local grid parameters is essential, which is the scope of this thesis.

2.6 Parameter and state estimation

APC algorithms can be used to control the power output of PV-generators, however they often require the local grid parameters and/or topology to be known. These required parameters are often unknown to the inverter, or can even be unavailable since DSOs do no make this information publicly available. This section presents related work on estimating the required parameters. Estimations generally fall into either of two categories, parameter estimation or state estimation. Algorithms that combine both estimations techniques also exist.

2.6.1 Parameter estimation

Parameter estimation is the process of estimating unknown parameters in a system based in measurements on the system. In the application of this thesis it is used to estimate grid parameters around the point of interest. Generally, the interest lies in knowing line impedances in a local network or the combined Thévenin grid impedance.

An overview of existing impedance estimation methods and comparisons between them are provided in [28]. The estimation method can be either active- or passive. Passive methods do not disturb the system and perform measurement based analysis. Active estimators have the ability to actively control the system. While this generally yields more accurate results, it is invasive to the system. Furthermore, in an application where both parameter estimation and state estimation (SE) (Section 2.6.3) is required, typically either of two approaches is used: 1) joint estimation, in which a single, more complex estimator for both parameters and states is used; 2) dual estimation, where different, individual estimators tailored to either state estimation or parameter estimation are used for both estimations [29].

A parameter estimator for supply impedance of grid-connected inverters is proposed in [30]. It includes a sophisticated method to estimate the inductance, that includes variations in supply inductance. An automated method to estimate all impedances in a local network is proposed in [31]. It does however require the topology of the local network, and computes all impedance values, so this method is better suited to an application where one single computation unit computes the parameters for a whole neighbourhood. [32] analyses harmonic impedance estimation for grid parameters. They conclude however that load models should be very accurate for harmonic estimation to function properly, which is information that is often unavailable. Finally, [33] proposes a hybrid event based estimation method. The method consist of observing the voltage until a certain change in magnitude triggers an event. The event will enable the active estimation method, which means that PQ variations are only induced by the system shortly after events. The method produces accurate results, and with less PQ disturbances compared to other active methods, however since it is an active method it is not applicable in all situations. Grid disturbances caused by the method are not always desired, and hardware for them is also not always available.

2.6.2 Thévenin equivalent

A subclass of parameter estimation has to do with estimating the Thévenin equivalent (TE). The grid can be modeled from the inverters perspective with the TE as shown in Fig. 2.7. Z_{load} represents the impedance of the house, and V_{th}, I_{th}, and Z_{th} represent the grid to which the house is connected.

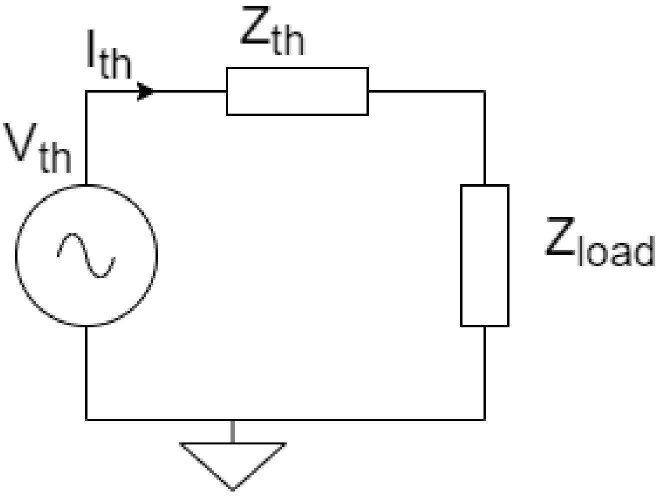

Fig. 2.7.: Thevenin equivalent model

Various least squares based TE estimation methods exist. A robust linear method is proposed in [34], that has increased accuracy over a classical least squares method since it assumes additional noise in the measurements. Similarly, [35] demonstrates both a linear and non-linear recursive least squares algorithm, where the non-linear variant provides more accurate results at the cost of an increase in required computation power. A bigger scale TE estimator is proposed in [36], where the method is tested on a multiport IEEE bus system. This method is suited for a centralized estimation application, and requires synchronised phasor measurements.

A PMU based method that is able to make an accurate estimation is proposed in [37]. It does however require PMU measurements from all system busses. Since this is not always possible, they propose to do a state estimation before doing the TE estimation. A method which takes phase drift into account is proposed in [38]. This method also only relies on a single PMU measurement at the bus of interest, making it an interesting option for distributed systems that each compute their own estimate. Similar to [38], the method proposed in [39] also only relies on measuring phasors at the point of common coupling (PCC). It induces active variations in power at the node and computes resistive and inductive line impedances based on samples with different power delivery. It shows that the method becomes more accurate if the difference in power between the samples is larger.

The TE provides a computationally efficient solution for some applications, since estimating it often is relatively straightforward. It might for some applications simplify the system too much, however. Changes in the topology of the grid will have an immediate effect on the estimation, and especially when energy can come from multiple DERs and/or the local transformer, only knowing the TE might not be sufficient. A potentially problematic scenario is shown in Fig. 2.8.

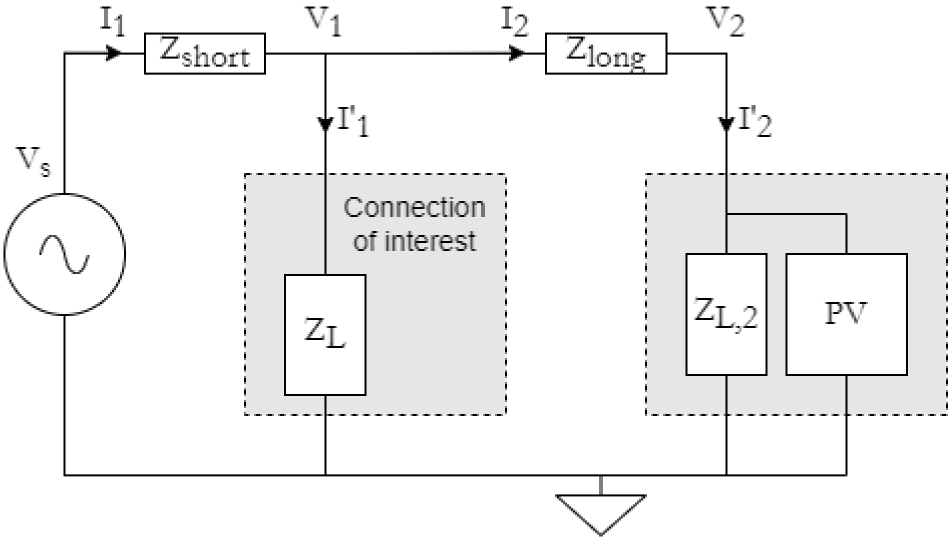

Fig. 2.8.: TE problematic scenario

Suppose there is a connection of interest in a local grid as shown in Fig. 2.8 at which the TE is estimated. In this specific scenario, the connection is relatively close to the transformer, and there is another connection much further down the feeder with a PV installation. The power consumed by the connection of interest is provided by the transformer when solar generation is low, and the PV installation further down the feeder provides the power when solar generation is high. In both situations the TE can be computed, however they will differ significantly, because of the difference in feeder length to the transformer and the PV installation. Depending on the application, this can induce problems, since the parameters no longer represent what is expected. Algorithms that need some time to stabilize could have a period in which the estimation is changing from one state to another when the power flow switches. Furthermore, the application should be aware that the estimation changes over time, and is not constant anymore.

2.6.3 State estimation

State estimation (SE) is the field of determining the state of a complex system, based on the available measurements of the system. States can include things like the position, orientation, and speed of a drone, or the voltages, currents, and impedances of a network. A lot of research is available on the topic of SE. An overview of relevant work within the field of power systems was published by an IEEE task-force on Power System Dynamic State and Parameter Estimation, which also provides a unified framework for future work [29]. It subdivides SE algorithms in a few distinct groups, dynamic state estimation (DSE), forecasting-aided state estimation (FASE), tracking state estimation (TSE), and static state estimation (SSE).

Dynamic State Estimation

In DSE, states of dynamic system are estimated using state space equations:

$$x_k = f(x_{k-1}, y_{k-1}, u_k, p) + w_k \tag{2.10}$$

$$z_k = h(x_k, u_k, p) + v_k, \tag{2.11}$$

where x_k is the system state vector, y_k the algebraic state vector that includes inputs of the system that are not tracked as states, z_k the measurement vector, u_k is the system input vector, p are the model parameters, f is the non-linear state transition, h is the non-linear measurement function, and w_k and v_k are the noise, usually assumed to be normally distributed zero-mean. [29]

DSE algorithms often make predictions for the state, based on previous measurements. Various filter types within the Kalman filter framework (Section 2.7) are used for the estimation. These filters typically consist of two steps, an predict step based on 2.10 and a update step based on 2.11.

Forecasting-aided state estimation

FASE is an application of DSE where the dynamics of x_k are sufficiently small to be neglected, and the state-transition is assumed to be linear, resulting in:

$$y_k = A_k y_{k-1} + \zeta_{k-1} + w_k \tag{2.12}$$

$$z_k = h(y_k, p) + v_k, \tag{2.13}$$

where A_k is the state transition matrix, and ζ_{k-1} is the trend vector [29].

FASE works well under Quasi-steady-state operating conditions, where states evolve smoothly. During transient conditions however, it may take some time to adapt to the new situation [40].

Tracking state estimation

TSE assumes A_k in 2.12 to be the identity matrix, reducing Equation 2.12 to:

$$y_k = y_{k-1} + w_k. \tag{2.14}$$

In TSE implementations, the state remains unchanged during prediction steps except for additive noise w_k.

Static state estimation

SSE is a further simplification of TSE where the prediction step is omitted entirely. Therefore it has no memory of previous states, and is not able to track system dynamics like DSE. It can work very well in the presence of quick changes however.

Applications of DSE

[41] proposes a non-iterative SE algorithm for grid state estimation. Due to it being non-iterative, the computational burden is lower compared to Monte Carlo solutions. An overview of distribution system state estimators is presented in [42]. Differences between various methodologies are discussed, as well as their use cases. Since a lot of DSE methods involve some form of a state tracking filter, more applications of DSE are mentioned in Section 2.7. Most of these state tracking solutions rely on PMU measurements for the measurement step of the filter.

2.7 Filtering techniques

For state estimation, state tracking filters are often used to estimated states over time. Depending on the application these filters use measurements of the states, or related parameters to the state they try to estimate. Since these measurements always include noise, a filter that deals with this noise is required to make an accurate estimation. The noise characteristics of the measurements is used in the estimation process. Perhaps the best known filter option is the Kalman filter family. Originally, the Kalman filter was used to track linear states in problems in which noise is Gaussian [43]. Various advancements in the research field have extended the filter family to much more problems, however. The following sections will elaborate on existing filter types.

2.7.1 Traditional Kalman filter

As mentioned, the traditional Kalman filter (KF) is an optimal filter that can be used to track states in a linear process of the form:

$$x(n+1) = Fx(n) + w(n), \tag{2.15}$$

where $x(n)$ is the state vector of the process at time n, F is the state transition matrix of the process and $w(n)$ is the noise in the process with known covariance. The filter models measurements of the form:

$$z(n) = Hx(n) + v(n), \tag{2.16}$$

where $z(n)$ is the measurement vector at time n, H is the measurement matrix which connects the state vector $x(n)$ to the measurement vector, and $v(n)$ is the measurement error with known covariance.

If the process is of the form described in 2.15 and 2.16, the Kalman filter can estimate the states based on the measurements and using the known characteristics of the noise. The filter works in two distinct steps, the predict step and update step.

Predict step

The predict step uses the state transition matrix F to predict the next state based on the previous state. Equation 2.17 shows the state prediction equation where $u(n)$

is the prediction control input and G is the control matrix which maps the control input to the state vector.

$$x(n+1) = Fx(n) + Gu(n) \tag{2.17}$$

Additionally, the Kalman filter keeps track of the uncertainty of the state estimate. Since the noise in both the process and the measurement is known, the uncertainty can be updated at every filter step. Equation 2.18 shows the uncertainty prediction equation where $P(n)$ is the uncertainty matrix, and Q is the process noise matrix.

$$P(n+1) = FP(n)F_T + Q. \tag{2.18}$$

With equations 2.17 and 2.18, the filter makes a prediction of the states based on the previous state.

Update step

The update step of the Kalman filter uses a measurement to update the state estimate and its uncertainty. Equation 2.19 shows the state update equation where K is the Kalman gain matrix.

$$x(n) = x(n-1) + K(z(n) - Hx(n-1)) \tag{2.19}$$

The Kalman gain is a measure of confidence that the filter places in both the state prediction and the measurement. K always has a value between 0 and 1. Based on the uncertainty of the prediction and the noise characteristics of the measurement, K is used to determine how much confidence is placed in a new measurement. If K is low, more confidence is placed in the prediction and/or the measurement is considered very noisy. If K is high, more confidence is placed in the measurement and/or the measurement is considered very accurate.

Equation 2.20 shows the update equation for the state uncertainty matrix. As shown in equation 2.20, K is also used to update the uncertainty in the state vector.

$$P(n) = P(n-1) - KHP(n-1) \tag{2.20}$$

Finally, the equation to obtain K is shown in equation 2.21 where R is the measurement noise matrix.

$$K = P(n-1)H_T \left(HP(n-1)H_T + R\right)^{-1} \tag{2.21}$$

As can be seen in equation 2.21, K is essentially of the form $K = \frac{P}{P+R}$ for every state in the state vector, which shows where the value ranges from 0 to 1 comes from. If $R \gg P$ then $K \to 0$ and if $R \ll P$ then $K \to 1$.
In an application the flow of the filter is as shown in Fig. 2.9.

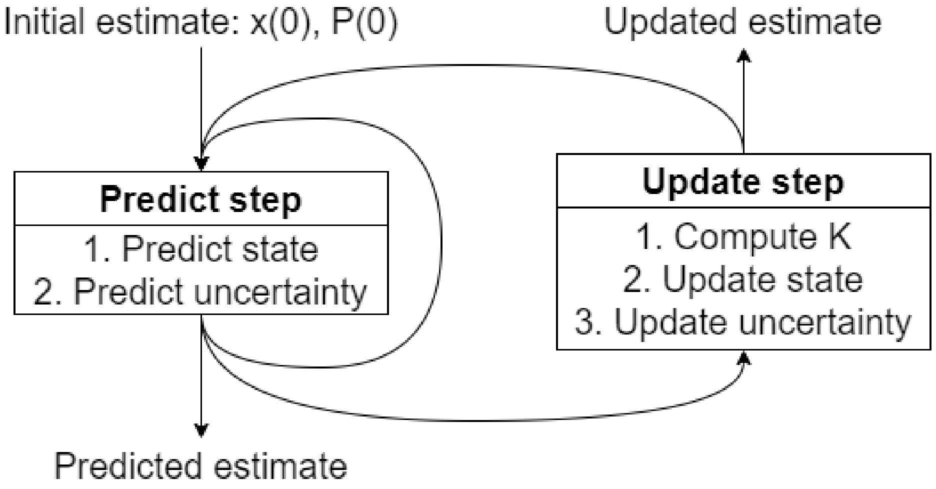

Fig. 2.9.: Flow of the Kalman filter in an application

The filter has to be instantiated with an initial estimate. Then, predict and update steps are taken to track the estimate. A prediction step consists of two parts; predict the state (equation 2.17) and the uncertainty (equation 2.18). An update step consists of three parts; compute the Kalman gain (equation 2.21), update the state (equation 2.19) and the uncertainty (equation 2.20).

Depending on the application, predict- and update steps are run one after the other, or multiple predict steps are run before an update step. This is especially relevant in applications where an accurate state estimation is needed at a much higher frequency compared to the measurements. The state can be predicted every time it is needed, and updated every time a measurement is available.

Applications of Kalman filter (KF)

In [44], a regular KF is used to filter a grid resistance and inductance estimate. The authors chose to limit the number of system states, because it results in a filter that is easier to tune for practical implementations. [45] demonstrates that a KF is able to track impedance of the human body over time. Although the application is different, it shows that the KF is able to track the impedance as a state. Most applications however include more complex states in the filter, which make the linearity constraint of the KF problematic.

2.7.2 Extended Kalman filter

The extended Kalman filter (EKF) is as the name applies an extension to the original filter. It enables the filter to be used in applications where the process and measurement forms are nonlinear as shown in equations 2.22 and 2.23 where f and h are nonlinear differentiable functions.

$$x(n+1) = f\left(x(n)\right) + w(n) \tag{2.22}$$

$$z(n) = h\left(x(n)\right) + v(n) \tag{2.23}$$

Since the process is no longer linear, some changes have to be made to equations 2.17, 2.18, 2.19, 2.20 and 2.21 also have to change to accommodate for this. The changes are to the state transition matrix and the measurement matrix as shown in equations 2.24 and 2.25.

$$F(n) = \left(\frac{\partial f}{\partial x}\right) \tag{2.24}$$

$$H(n) = \left(\frac{\partial h}{\partial x}\right) \tag{2.25}$$

Note that F and H are now no longer constant as in the linear implementation, but linearization in a moment in time. It should also be noted that the filter is no longer optimal due to the linearization.

Applications of extended Kalman filter (EKF)

The EKF is a very popular state tracking filter. For many applications it strikes a good balance between computational complexity and accurate modelling. [46] shows an application of EKF for estimating grid impedance and voltage. However, the filter is limited to inductive-resistive networks, as their grid model does not include capacitive components. [47] shows a similar application, and also utilizes an EKF to estimate impedances. Both [46] and [47] acknowledge that tuning the filters is a trial and error procedure that could be a time-consuming task in a practical implementation. In [48], multiple test cases of specific bus events are tested which show that EKFs can be used in more extensive power system state estimation applications. Similarly, [49] demonstrates the filters capabilities in a battery impedance tracking application, which features an impedance changing over time.

2.7.3 Unscented Kalman filter

The EKF can be viewed as a first order approximation of the process. The unscented Kalman filter (UKF) tries to address the problems that come with this [50]. It is an extension of the unscented transformation where sigma points are used to calculate the statistics of the random process and noise variables. Where in the EKF only one point is propagated to the nonlinear process model, the unscented Kalman filter (UKF) propagates multiple points. Usually, $2n + 1$ points are used, where n is the dimensional of the state space. When these points are propagated through the process model, the random variable statistics are computed from the propagated points. The fact that multiple points are used instead of only a single point makes this filter type more accurate compared to the EKF [51].

Applications of unscented Kalman filter (UKF)

In [52], multiple variants of Kalman filters are tested for a multi-area distributed state estimation. While both the regular KF and EKF implementations also yield acceptable results, the UKF implementation has the lowest estimation error, since it is better suited to the non-linear application of the large area. [53] does a similar experiment, comparing the performance of an EKF to an UKF in a distribution net state estimation application. The results are very similar between the two filters, indicating that an EKF implementation can be better suited to a problem, especially since it is computationally more efficient.

2.7.4 Ensemble Kalman filter

The ensemble Kalman filter (EnKF) is a particular adaptation of the KF that is useful applications with a lot of states to track. It is a Monte Carlo implementation that approximates the regular KF. The state distribution is represented by a sample, or ensemble, which is propagated through time. This ensemble is a dimension reduction of the state, making this filter computationally feasible for very high dimensional problems. [54]

Applications of ensemble Kalman filter (EnKF)

Since the EnKF is particularly useful in situations where a lot of states have to be tracked, the applications here are slightly different compared to the application of this thesis. [55] and [56] both demonstrate the benefits of an EnKF in high dimensional applications. The EnKF is used for both parameter estimation and state estimation in these two papers. Additionally, [55] compares the performance to an EKF shortly. Background information on the EnKF is explained very thoroughly in this paper as well, so readers that are interested in the technical parts of the EnKF are pointed to [55].

2.7.5 Particle filter

A well known alternative to the KF is the particle filter (PF). Similar to the EnKF this is a filter that relies on sequential Monte Carlo methodology to estimate the state. Since it does not assume linearity it is more flexible compared to a KF, however this comes at the cost of required computation power [57].

Applications of particle filter (PF)

In [58], a particle filter is used to do parameter estimation in a non-linear process. It demonstrates superior performance compared to an EKF, however CPU load for the PF is almost 50% higher compared to the EKF. [59] uses a PF to estimate the phase angles in a distribution grid. In this application, the filter is implemented on a low cost microprocessor, demonstrating that efficient computation of such a filter is possible.

2.8 Conclusion

As the amount of DERs increase, and PV-penetration in residential areas rises, local overvoltage problems can occur during specific times in a day. This results in inverters turning off if no solution to this problem is implemented. This is especially problematic for connections towards the end of the feeder, since their inverters experience overvoltage issues first. APC algorithms can be used to make curtailment as efficient and fair as possible, however these algorithms often require information of the surrounding grid. This information is often not available or very difficult to obtain, creating a need for algorithms able to estimate the required information. The remainder of this thesis will present a lightweight KF solution to estimate grid parameters based on PMUs measurements.

3 Use-case

This Chapter details the test site and sensor platform that is utilized to test the proposed estimator this thesis. Section 3.1 elaborates on the test site layout and what information is available on the LV cables. Sections 3.2 shows the sensors that are used and the available data.

3.1 Test site

As part of the Fairplay project, a rural LV-feeder near the village of Markelo in the east of the Netherlands is equipped with some PMU sensors from Smart State Technology (SST) [12]. In the feeder, two connections are equipped with PMUs, and unmeasured connections are present on the feeder before, in-between, and after the measured connections. There are no sensors at the transformer. The data of these sensors can be accessed through their internet connection. The test site is shown in Figure 3.1.

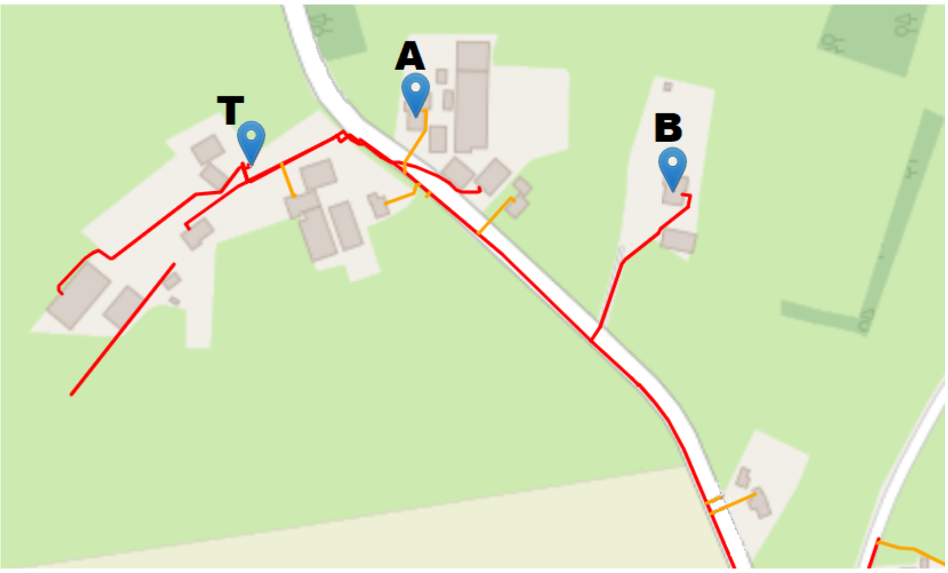

Fig. 3.1.: Test site location

Annotated in Figure 3.1 are the two measured connections A and B, and the MV-LV transformer T. As can be seen in the figure, there are additional unmeasured connections between the transformer and node A and B, in between node A and B, and after node A and B. The information on the specific cables is available in the form of grid documentation. The file that specifies the lengths and types of the cables is shown in Figure 3.2.

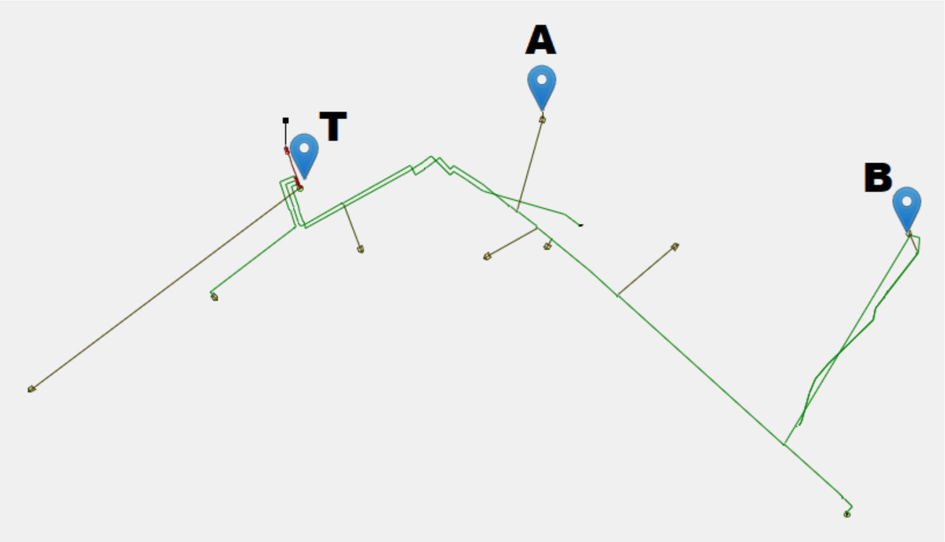

Fig. 3.2.: Cable information file

As in Figure 3.1, in Figure 3.2 A, B, and T again depict the measured connections and the transformer. Each of the cable segments shown in Figure 3.2 contains information on the length and type of the cable, from which the grid parameters can be obtained. Figure 3.3 shows a graphical model of the test site.

Since the cable type and length for Z_A, Z_B, Z_{FA}, and Z_{FB} is known, the theoretical impedance from transformer to A and A to B can be determined. The cable information is shown in Table 3.1. Z_B consists of 2 different cable types, as indicated in Table 3.1 by Z_{B1} and Z_{B2}.

Tab. 3.1.: Cable types and lengths on site

	Cable type	**Length** (m)	**Cabletype Impedance** (Ω/km)	**Cable impedance** $(m\Omega)$
Z_A	1166 GPLKh 4x6mm2 Cu + 4x1.5mm2 Cu	47	$3.061 + 0.1i$	$143.867 + 4.7i$
Z_{B1}	1182 GPLKh 4x10mm2 Cu + 4x1.5mm2 Cu	10.999	$1.837 + 0.088i$	$20.205 + 0.968i$
Z_{B2}	1166 GPLKh 4x6mm2 Cu + 4x1.5mm2 Cu	98.435	$3.061 + 0.1i$	$301.310 + 9.844i$
Z_{FA}	1428 VMvKh 4x50mm2 Al + 4x2.5mm2 Cu	135.585	$0.641 + 0.085i$	$86.910 + 11.525i$
Z_{FB}	1428 VMvKh 4x50mm2 Al + 4x2.5mm2 Cu	159.603	$0.641 + 0.085i$	$102.306 + 13.566i$

This information on the cables is used in Section 5.2 to validate the results of the estimator.

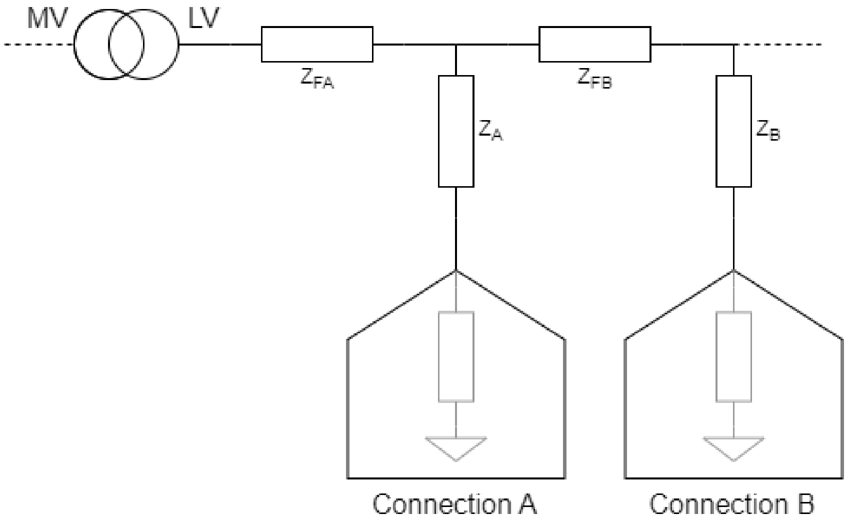

Fig. 3.3.: Graphical model of the test site

3.2 Sensor system

The test site is equipped with GPS-synchronized PMUs made by Smart State Technology (SST). The sensors contain an Orange-PI, a Raspberry-PI like Arm single board computer with a shield that contains an additional microcontroller. The measurements are synchronized to a GPS-beacon with a phase locked loop estimation algorithm.

On the two measured connections, the voltage and current for each phase, including the neutral, is measured at a frequency of $4kHz$. These values of voltage and current are then used by the many available included DSP solutions to calculate phasors, frequency, RMS, thd, and much more. For this thesis, the calibrated phasors are used.

3.2.1 PMU data

The PMU data used for the experiments of this thesis is measured with the sensors from SST. It consists of 4 current- and voltage-phasors for each of the two measured LV prosumers, three for each phase and one for the neutral. The data from the sensors can be accessed via their network connection. SST provides a web portal shown in Figure 3.4 where the data can be visualized and downloaded. Data can also be streamed using an API.

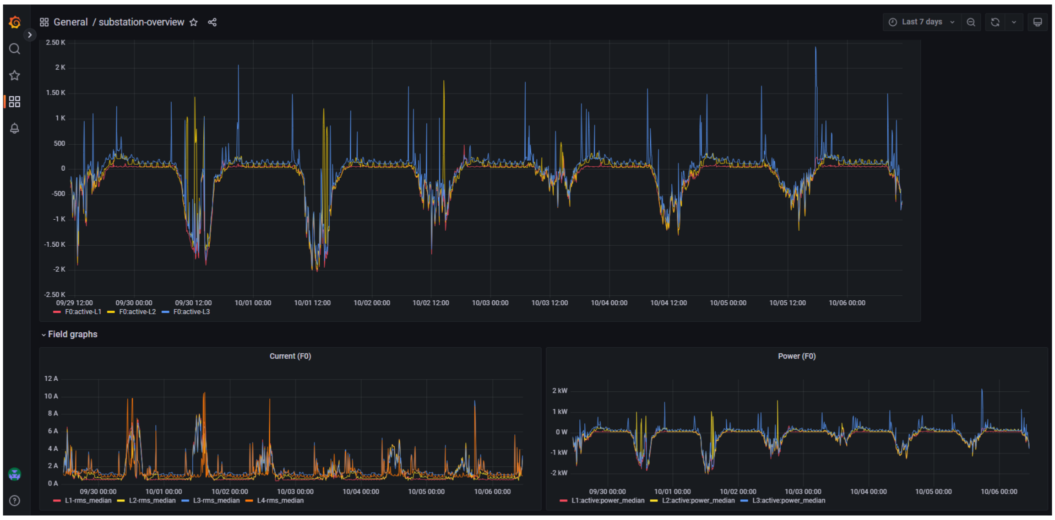

Fig. 3.4.: Data portal for the PMUs (from SST [12])

Almost 12.5 million samples are gathered from all available sensors in different times of the year 2023. The periods of data that are used are:

Tab. 3.2.: Available data periods

Start		End		Duration	File-size (MB)
March 20	13:06:35	March 20	13:06:50	00:00:15	0.464
March 20	13:08:02	March 20	13:09:05	00:01:03	1.858
March 20	13:12:26	March 20	13:13:27	00:01:01	1.669
March 20	13:14:29	March 20	13:21:39	00:07:10	9.175
March 20	13:21:59	March 20	16:43:40	03:21:41	29.986
March 22	10:46:53	March 22	21:12:16	10:25:23	104.014
April 21	09:09:22	April 21	17:04:23	07:55:01	875.441
May 24	16:41:43	May 26	10:48:48	42:07:05	4,671.101
June 06	01:25:58	June 06	19:31:06	18:05:08	1,999.147

It can be observed in Table 3.2, that there is data missing for March 20th, with gaps of a few minutes between the measurements. Furthermore, the file-size is not consistent with the covered duration of the file for the data from March 22nd. It spans almost 10.5 hours, however the file-size indicates that a lot of data is missing.

Using these measurements, the online behaviour of the estimator is simulated in a controlled way. The information available to the estimator is identical to the real world application, and the same recorded data is used by benchmark estimators to provide a fair comparison.

Estimator design and design choices

4

The method of the online parameter estimator is explained in this chapter. First, in Section 4.1, the sensitivity parameter will be defined. Section 4.2 explains the design of the estimator. Next, Section 4.3 explains the noise characteristics of the measurements. Section 4.4 explains how the estimator is made robust to both one- and three-phase devices. Lastly, Section 4.5 explains the benchmark estimations techniques to which the estimator results are compared.

4.1 Sensitivity

The method of APC that inspired this thesis utilizes the sensitivity from one LV-connection to another. The term *sensitivity* is defined in [11] as:

$$\xi^{kj}_{a,P}(t) = \frac{\Delta V^{kj}_{aN,P}(t)}{\Delta P^{j}_{a}(t)} \tag{4.1}$$

where $\xi^{kj}_{a,P}(t)$ is the sensitivity at time t at phase a in the network, $\Delta P^{j}_{a}(t)$ is the change in power at node j, and $\Delta V^{kj}_{aN,P}(t)$ is the change in voltage at node k. The sensitivity is thus defined as the changed in voltage at node k due to the change in power at node j. For this thesis, the definition of sensitivity is changed slightly, from change in power to change in current, since it incorporates the same information and now has a direct analogy to impedance.

$$\xi^{kj}_{a}(t) = \frac{\Delta V^{k}_{a}(t)}{\Delta I^{j}_{a}(t)} \tag{4.2}$$

The sensitivity $\xi^{kj}_{a}(t)$ is now the change in voltage at time t in phase a and at node k as an effect of the change in current at time t in phase a at node j. Knowing this value enables the prediction of a certain required change in current at node j so that the voltage at node k reaches a desired value. Furthermore, this sensitivity is divided in its real and imaginary part:

$$\xi^{kj}_{a,real}(t) = \frac{\Delta V^k_a(t)}{\Delta I^j_{a,real}(t)} \tag{4.3}$$

$$\xi^{kj}_{a,imag}(t) = \frac{\Delta V^k_a(t)}{\Delta I^j_{a,imag}(t)} \tag{4.4}$$

Theoretically, the sensitivity values are constant, since they represent an impedance in the network. In real-life applications however, changes in power consumption at other nodes add noise to the measurements.

4.2 Estimator

The estimator is an implementation of a Kalman filter, with a variable measurement variance based on the measured difference in power. The choice for a KF is made to keep the application deployable in an online, distributed fashion on lightweight hardware. Furthermore, the filter should be sufficient since the sensitivity is constant. A KF is able to estimate the value of a constant with noise in the measurements.

The filter equations are shown and explained in the following sections. In all equations, x denotes the state vector, P the estimate uncertainty matrix, F the state transition matrix, G the control matrix, u the prediction control input variable, Q the process noise matrix, H the measurement matrix, and R the measurement noise matrix. x' and P' denote the state and uncertainty after the prediction step, and x and P denote them after the update step.

4.2.1 State vector

The state vector x of the estimator is defined as:

$$x = \begin{bmatrix} \xi_{v,real} \\ \xi_{v,imag} \\ v \end{bmatrix} \tag{4.5}$$

where $\xi_{v,real}$ is the sensitivity with respect to the real current, $\xi_{v,imag}$ is the sensitivity with respect to the imaginary current, and v is the voltage phasor at the position of interest.

4.2.2 Predict step

The general KF equations for the predict step are:

$$x(n+1) = Fx(n) + Gu(n) \tag{4.6}$$

$$P(n+1) = FP(n)F_T + Q \tag{4.7}$$

The state transition matrix F is defined as the identity matrix, which means that $Fx(n)$ simply copies the previous state to the next prediction. The control input $u(n)$ is used as:

$$u(n) = \begin{bmatrix} \Delta I_{real} \\ \Delta I_{imag} \end{bmatrix} \tag{4.8}$$

The control matrix matrix G can then be defined as:

$$G = \begin{bmatrix} 0 & 0 \\ 0 & 0 \\ \xi_{v,real} & \xi_{v,imag} \end{bmatrix} \tag{4.9}$$

where $\xi_{v,real}$ and $\xi_{v,imag}$ are the current sensitivity estimations from the state vector. This means that the current sensitivity estimations are used to predict the voltage for the next step.

Lastly, the process noise matrix Q is defined as:

$$Q = \begin{bmatrix} \gamma_{\xi_{v,real}} & 0 & 0 \\ 0 & \gamma_{\xi_{v,imag}} & 0 \\ 0 & 0 & \gamma_v \end{bmatrix} \tag{4.10}$$

A non-zero number for $\gamma_{\xi_{v,real}}$, $\gamma_{\xi_{v,imag}}$, and γ_v results in an increase in uncertainty for the estimation every step, through Equation 4.7. This means that the estimator cannot get stuck on a wrong parameter. The values have to be chosen sufficiently small enough to let the filter approach to a correct estimate.

4.2.3 Update step

The general KF equations for the update step are:

$$K = P(n-1)H_T\left(HP(n-1)H_T + R\right)^{-1} \tag{4.11}$$

$$x(n) = x(n-1) + K(z(n) - Hx(n-1)) \tag{4.12}$$

$$P(n) = P(n-1) - KHP(n-1) \tag{4.13}$$

Measurements for the filter are defined of the following form:

$$z = \begin{bmatrix} \xi_{v,real} \\ \xi_{v,imag} \\ v \\ \Delta I_{real} \\ \Delta I_{imag} \end{bmatrix} \tag{4.14}$$

The measurement contains the sensitivities with respect to the real and imaginary current. The noise around these parameters is filtered out by the estimator. Next to this, the measurement vector also contains v, which is used to update the state vector. Lastly, the measurement vector includes ΔI_{real} and ΔI_{imag}, which are used to determine the confidence in the measurement.

The measurement matrix H is:

$$H = \begin{bmatrix} 1 & 0 & 0 \\ 0 & 1 & 0 \\ 0 & 0 & 1 \\ 0 & 0 & 0 \\ 0 & 0 & 0 \end{bmatrix} \tag{4.15}$$

which copies all measured states to the state vector. The measurement noise matrix R is defined as:

$$R = \begin{bmatrix} \alpha & 0 & 0 & 0 & 0 \\ 0 & \beta & 0 & 0 & 0 \\ 0 & 0 & \sigma_v^2 & 0 & 0 \\ 0 & 0 & 0 & 0 & 0 \\ 0 & 0 & 0 & 0 & 0 \end{bmatrix} \tag{4.16}$$

where σ_v^2 is the variance in the voltage measurements and α and β contain the information on the noise as found in Section 4.3. Using this equation in the measurement noise matrix R results in different confidence levels in the measurements based on ΔI. Measurements where the change in current is small contain more noise, so the filter uses their information less. Measurements where the change in current is large contain less noise, so the filter uses their information more. Therefore, a region around 0 change in I is created with the interval:

$$-0.5A < \Delta I < 0.5A \tag{4.17}$$

in which the measurement is discarded.

4.3 Noise characteristics

A vital part of using the KF successfully means having knowledge on the noise characteristics of the measurements. This section is dedicated to explaining the noise in the measurements. Figure 4.1 shows typical sensitivity measurements on the system described in Chapter 3.

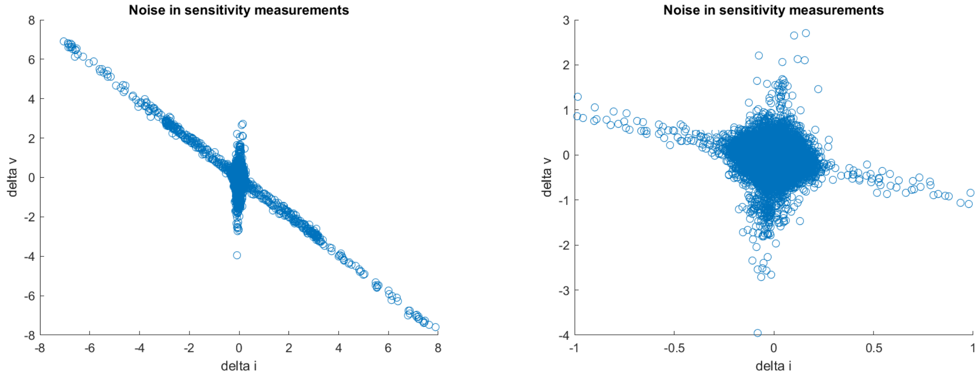

(a) Full range view

(b) Area around $\Delta i = 0$

Fig. 4.1.: Measurements on the system and their noise

As can be seen in Figure 4.1a, there seems to be a clear linear relation between Δv and Δi, but there is noise in the measurements. The noise increases significantly around $\Delta i = 0$. Figure 4.1b shows this area in more detail.

Looking at the definition of the sensitivity as presented in Equation 4.2, it becomes clear that the increase in noise around $\Delta I = 0$ becomes significantly worse, since result goes to infinity for small currents. Figure 4.2 shows the sensitivity measurements and the noise.

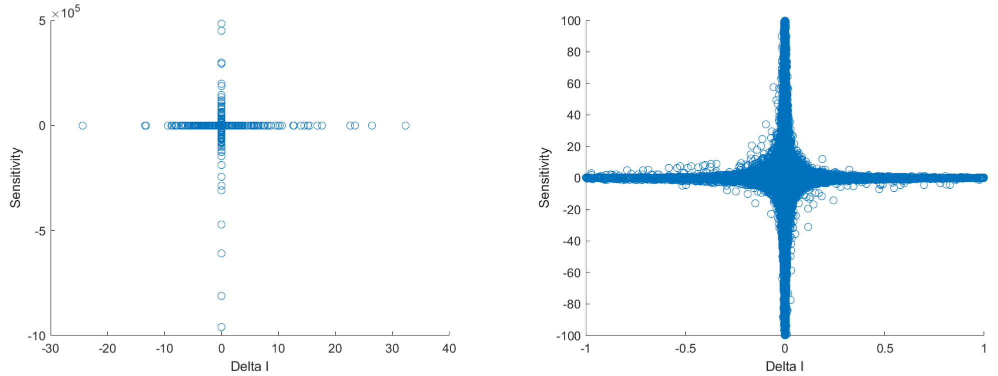

(a) Full range view

(b) Area around $\Delta i = 0$

Fig. 4.2.: Sensitivity measurements on the system with noise

As is depicted in Figure 4.2a, the noise goes to infinity when ΔI goes to 0. Figure 4.2b shows a zoomed in version of the noise, which shows an exponential relation in the noise compared to ΔI. This information on the noise present in the measurements can be used in the filter equations to adapt the estimators behaviour to the noise. Section 5.4.1 explains how this is done for the test case.

4.4 One-phase versus three-phase devices

To get the voltage, real current, and imaginary current used by the estimator, the incoming phasor measurements are processed. Equation 4.18 shows the equation for the real current. To get the real current, the angle of the voltage phasor is subtracted from the current phasor. The angle of the current phasor is now the angle difference between the voltage and the current. Taking the real part of this current phasor gives the active current:

$$I_{real} = real\left(I_{phasor} \cdot e^{-i \cdot \theta_{V_{phasor}}}\right) \tag{4.18}$$

For the voltage, the magnitude of the phasor can simply be taken, since the phase information is already taken into account with the current.

$$V = \|V_{phasor}\| \tag{4.19}$$

Next, the difference in voltage and current is taken, since the interest lies in difference in voltage as a function of difference in current.

$$\Delta I_{real} = I_{real}(n) - I_{real}(n-1) \tag{4.20}$$

$$\Delta V = V(n) - V(n-1) \tag{4.21}$$

Figure 4.3 shows a scatter plot of ΔV_{phase1} versus $\Delta I_{real,phase1}$ shows the relation.

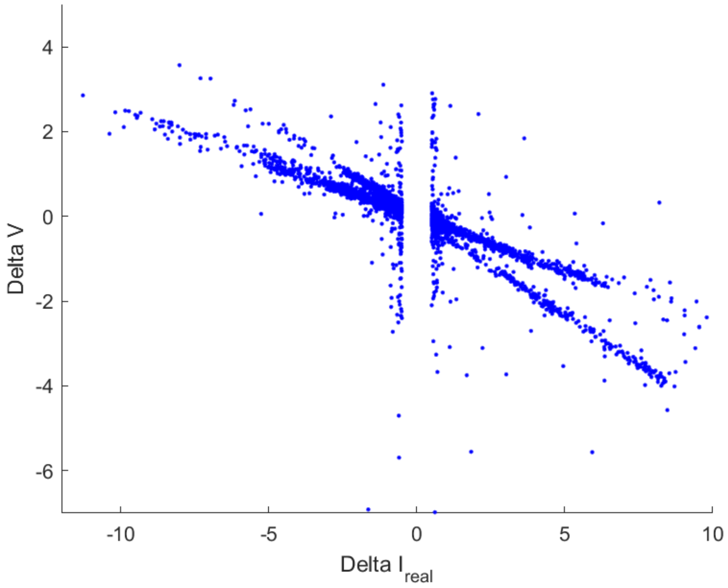

Fig. 4.3.: Scatter plot of the sensitivity, ΔV_{phase1} versus ΔI_{phase1}

The data in the interval $-0.5A < \Delta I < 0.5A$ is left out of the data, since the noise increases exponentially around zero as presented in Section 4.3.

It can be observed that two lines seem to exist in the plot. These two lines indicate single- or three-phase equipment. When a three-phase device changes power, the neutral current remains the same, since the power in- or decrease is the same in all phases. When a single-phase device changes power however, the current in the neutral phase is affected since it increases with the unbalance in the system. Since the change in current is then happening twice (both on the phase- and neutral-wire), the resulting line is approximately 2 times steeper compared to the three-phase line. This makes sense if the graph is translated to impedance where for a single phase device, the found impedance would be twice as big, since the impedance of the phase wire and the neutral wire add up.

In order to fix this, both lines can be mapped together by also taking the change in neutral current into account. Changing the definition of sensitivity as given in equation 4.2 in Section 4.1 to include the neutral current gives the following relation.

$$\xi_a^{kj}(t) = \frac{\Delta V_a^k(t)}{\Delta I_a^j(t) + \Delta I_N^j(t)} \tag{4.22}$$

where $\Delta I_N^j(t)$ is the neutral current at time t and node j. Figure 4.4 shows the plot where the neutral current is taken into account.

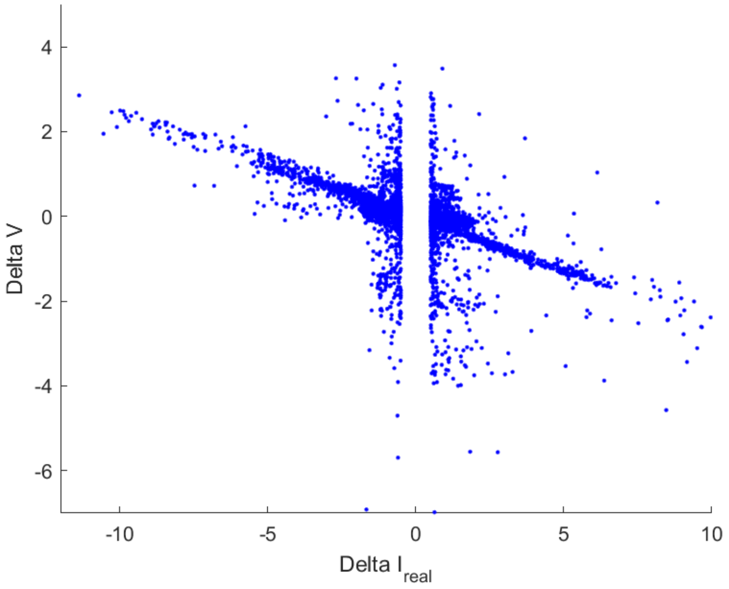

Fig. 4.4.: Scatter plot of the sensitivity, ΔV_{phase1} versus ΔI_{phase1}

As can be observed in Fig. 4.4, the noise in the data has increased compared to Fig. 4.3. This is due to the change in neutral current as an effect of the other two phases, which is now added as noise to the denominator of the sensitivity as shown in Equation 4.22.

Next to the change in voltage as effect of the real part of the current, the imaginary part also has an effect. The imaginary part of the current is taken similar to the active current in equation 4.18.

$$I_{imag} = imaginary\left(I_{phasor} \cdot e^{-i \cdot \theta_{V_{phasor}}}\right) \tag{4.23}$$

after which the difference can be computed again, similar to 4.20.

$$\Delta I_{imag} = I_{imag}(n) - I_{imag}(n-1) \tag{4.24}$$

Figure 4.5 shows a plot of I_{imag}.

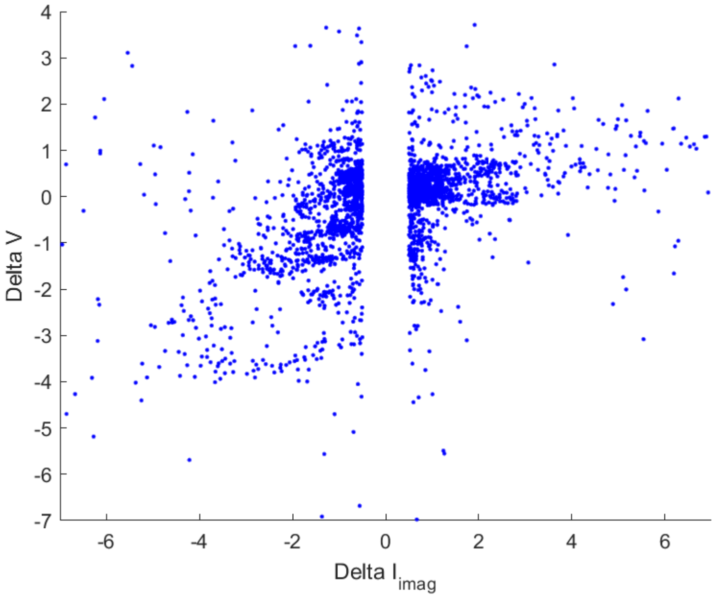

Fig. 4.5.: Scatter plot of the sensitivity with respect to the imaginary part of the current, ΔV_{phase1} versus ΔI_{phase1}

As can be seen in Figure 4.5, the imaginary sensitivity does not seem to have an nearly linear relation to the change in current as observed for the real sensitivity. The cause of this is likely phase drift [38], but further analysis is outside the scope of this thesis. Additionally, while the imaginary part of the sensitivity does have an effect on the voltage, its contribution is significantly less compared to the real part. In Table 3.1, it can be seen that the imaginary part of the impedance is much smaller than the real part.

4.5 Ground truth and benchmark estimations

In order to be able to quantify the performance of the estimator, a ground-truth- and benchmark-estimator are used to compare the results with the estimator designed in this thesis. These are the cable-data estimation and the linear-fit estimation.

4.5.1 Ground truth: cable-data-based estimation

This estimation is based on the known data on the cables in the system. Information on cable length and type is often not available, however for this research project, the information is available to compare results to. The known cable impedance Z as depicted in Table 3.1 in Section 3.2 is used to predict the voltage as:

$$v(n+1) = v(n) + Z_{real} \cdot \Delta I(n) \tag{4.25}$$

where ΔI is the real part of the current, and Z_{real} is only the real part of the known impedance to keep the results comparable with the designed estimator. This estimation is viewed as a ground truth estimation, however it should be noted that impedance values this can still be wrong. In real-world applications, many factors such as temperature and surrounding materials can affect cable impedance values.

4.5.2 Benchmark: linear-fit-based estimation

A benchmark method is used since information for the cables is often not available. This method consist of a linear fit through the estimation data. As Section 4.4 already showed, the relation for the sensitivity seems to be linear. The linear fit is made with a least-squares algorithm through the data of April 21st. This day is chosen since the amount of data of this day is enough to determine the linear relation. Shorter time periods do not provide enough data, and longer would result in less data to test the filter on. This linear fit is then used to predict the voltage for the remainder of the data.

Performance of the estimator 5

This section explains how the performance of the designed estimator is tested and discusses the results. The estimator estimates the sensitivity ξ_a^{kj} on a voltage in phase a at node k with respect to the current in phase a at node j as defined in Section 4.1. Since there are two measured connections on the feeder with three phases, the estimator can estimate for $a \in 1, 2, 3$ where $1, 2, 3$ represent the three phases and $k, j \in A, B$ where A and B are the two individual connections as indicated in Section 3.2.

First, Section 5.1 explains the error comparison method used to assess the performance of the estimator. Section 5.2 and Section 5.3 explain the ground-truth- and benchmark estimation results respectively. Section 5.4 shows the results of the online estimator, after which the three estimation methods are compared in Section 5.5. Section 5.6 shortly discusses the magnitude of the error and Section 5.7 looks at the computational efficiency and options to deploy the estimator for online applications in the field. Finally, Section 5.8 concludes this chapter and summarizes the results.

5.1 Error comparison method

This section describes how the errors of the three methods will be compared. Figures in this sections are merely there to illustrate how the error figures are generated, and why that choice is made. Actual results can be found beyond this section.

To quantify the performance of the estimator, the error in voltage prediction is compared to the error of the voltage prediction of the ground-truth- and benchmark estimators. For all three methods, the voltage at time $n+1$ is predicted based on the voltage at time n and the change in current from n to $n+1$. The error is given as

$$Error(n) = |V_{measured}(n) - V_{predicted}(n)| \tag{5.1}$$

where the error is thus the absolute value of the difference between the predicted voltage $V_{predicted}(n)$ and the actual measured voltage $V_{measured}(n)$. An example plot of such an error is shown in Figure 5.1.

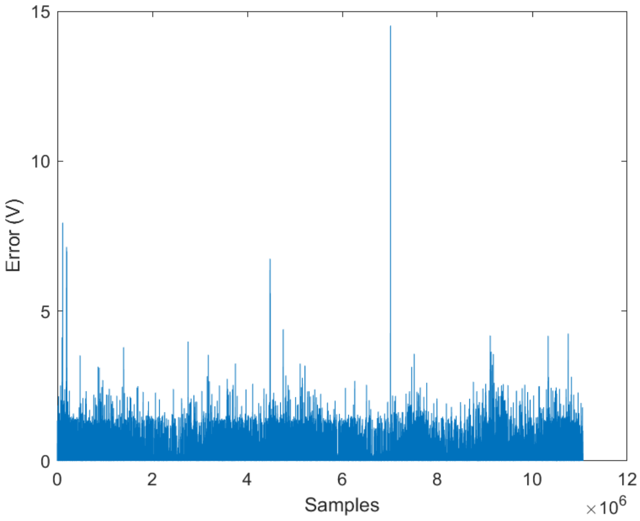

Fig. 5.1.: Error figure example, error in the cable-data estimation ξ_1^{BB}

As can be seen in Figure 5.1, the large number of samples makes these figures difficult to interpret. To make interpretation possible, the individual error samples are ordered from small to large. The result is an increasing line, which shape can be compared to other estimation methods. Figure 5.2 shows the sorted error of the example Figure 5.1.

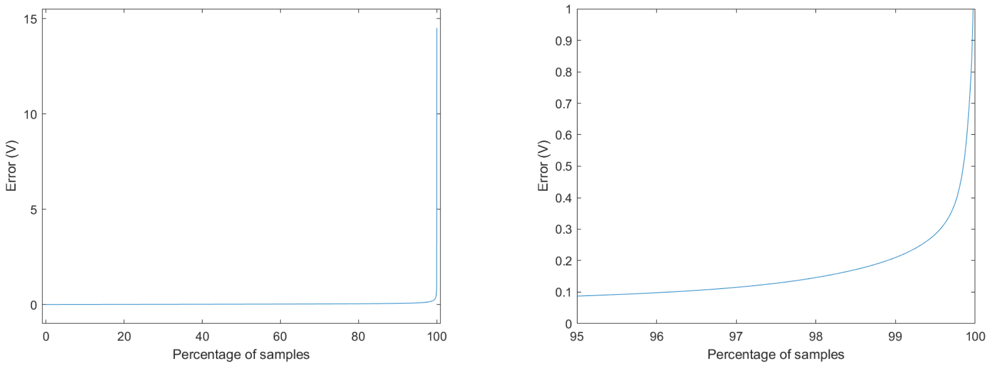

(a) Complete range of error

(b) Zoomed image

Fig. 5.2.: Sorted error figure example, error in the cable-data estimation ξ_1^{BB}

As is visible in Figure 5.2, the error is now a clear line. The x-axis has been changed from samples to percentage of samples. For all three methods such error graphs are created, and the performance is compared in Section 5.5. Lastly, to make comparison between the methods concrete, the root-mean-square error (RMSE) is also computed as:

$$RMSE = \sqrt{\frac{\sum_{n=1}^{N} (Error(n))^2}{N}} \tag{5.2}$$

where $Error(n)$ is the error at sample n as given by Equation 5.1 and N is the total number of samples.

5.2 Ground truth - cable-data estimation

To find the theoretical sensitivity for the cable-data estimation, the data on the test site as presented in Section 3.2 can be recalled. Figure 5.3 shows the model of the test site.

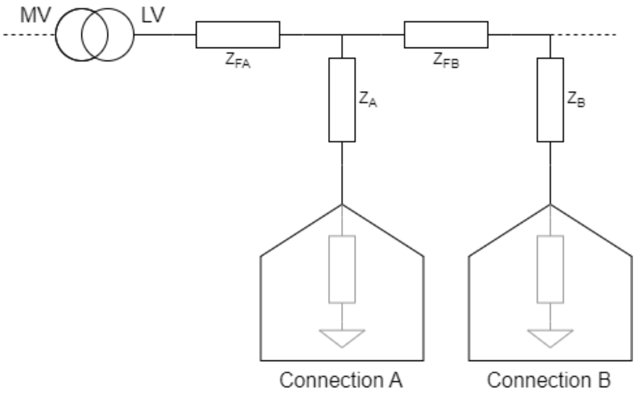

Fig. 5.3.: Graphical model of the test site

Since there are two measured nodes, there are four different sensitivity options, as shown in Table 5.1. The values in the table are taken from Table 3.1 according to what impedance the sensitivity represents and converted from $m\Omega$ to Ω. They only include the real part to keep results comparable with the online filter implementation.

Tab. 5.1.: Sensitivity values for cable-data benchmark estimation

	Sensitivity (Ω)
ξ_a^{AA}	-0.230777
ξ_a^{AB}	-0.08691
ξ_a^{BA}	-0.08691
ξ_a^{BB}	-0.510731

The sorted error curves are generated as explained in Section 5.1. These curves can be seen in Appendix A.1 and will be used and discussed in Section 5.5.

5.3 Benchmark - linear fit estimation

For the benchmark estimation, a linear relation is estimated using a linear fit in Matlab as explained in Section 4.5.2. Two examples of such linear fits are shown in Figure 5.4, all linear fit plots can be found in Appendix A.2.

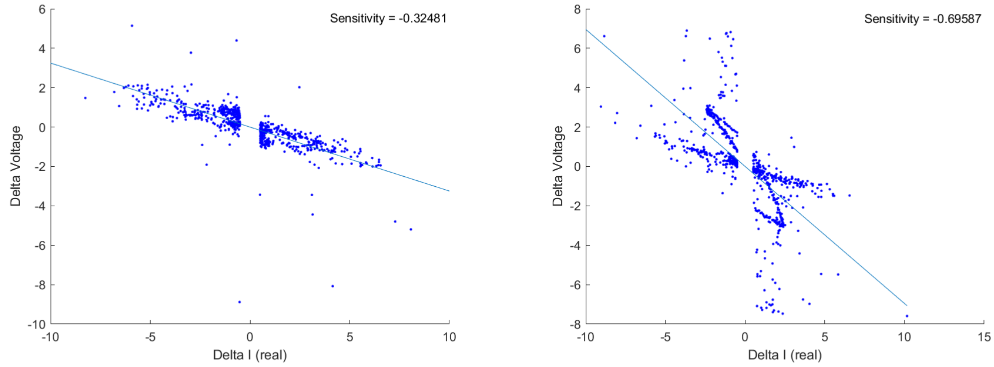

(a) Linear fit for ξ_2^{BB}

(b) Linear fit for ξ_1^{BB}

Fig. 5.4.: Linear fit results

As can be seen in Figure 5.4, the fitting a linear curve sometimes does not yield the expected result. In Figure 5.4a, a linear fit for the sensitivity ξ_2^{BB} for phase 2 is made. As can be seen, the data can be described by the linear fit. In Figure 5.4b however, the same is done for the sensitivity ξ_2^{BB} at phase 3. An unknown event which was not visible in phase 2 caused numerous data points that cannot be covered by a linear relation. The linear fit therefore does not represent the data that it was supposed to, and the results may give a larger error.

Tab. 5.2.: Linear fit sensitivity estimation

	Linear-fit sensitivity	Cable-data sensitivity
ξ_1^{AA}	-0.1309	-0.230777
ξ_2^{AA}	-0.3036	
ξ_3^{AA}	-0.1722	
ξ_1^{AB}	-0.1008	-0.08691
ξ_2^{AB}	-0.0446	
ξ_3^{AB}	-0.0397	
ξ_1^{BA}	-0.0379	-0.08691
ξ_2^{BA}	-0.0953	
ξ_3^{BA}	-0.0566	
ξ_1^{BB}	-0.6959	-0.510731
ξ_2^{BB}	-0.3248	
ξ_3^{BB}	-0.3194	

The resulting sensitivity value from the linear fit for each of measurements is shown in Table 5.2. The table also shows the value that was expected from the cable-data.

As can be observed from Table 5.2, the linear fit can result in quite different sensitivity values compared to the expected value from the cable data. All linear fit figures can be seen in Appendix A.2, together with the error between the predicted and measured voltage as explained in Section 5.1.

5.4 Online Kalman estimator

The estimator design is ran on the datasets for each of the possible combinations of a, k, and j. The data from April 21st is not used to keep the benchmark results comparable to the estimator result.

5.4.1 Estimator parameters

The choice for the estimator parameters that model the noise is explained here. Specifically, α and β that include the measurement noise characteristics, and $\gamma_{\xi_{v,real}}$, $\gamma_{\xi_{v,imag}}$, and γ_v that specify the process noise are explained here.

Process noise

The values of $\gamma_{\xi_{v,real}}$, $\gamma_{\xi_{v,imag}}$, and γ_v can be used to set the filters sensitivity to disturbances and speed of convergence. If the values are chosen larger the filter increases the uncertainty of the estimate more every predict-step, meaning that the filter tracks variations in system state more. Keeping the value lower, means that the filter is slower to change, so noisy outliers in the measurements don't throw the filter off. For the results in this thesis, the following values are used: $\gamma_{\xi_{v,real}} = \gamma_{\xi_{v,imag}} = 1e-15$, which ensures that the sensitivity estimates are gradually adapting to the measurements. $\gamma_v = 0.002$, which means that the filter tracks changes in voltage quicker. These values are obtained empirically by sweeping these values until the filter adapts to state changes at the desired speed.

Measurement noise

The values of α and β should reflect the noise characteristics of the measurements as explained in Section 4.3. To achieve this, an exponential fit is made with Matlab through the variance of this noise, which can be used in the KF to better estimate the noise. The sensitivity samples are divided in bins with an equal number of samples. The relation is fitted through the variance of these bins. The fitted relation is depicted in Figure 5.5.

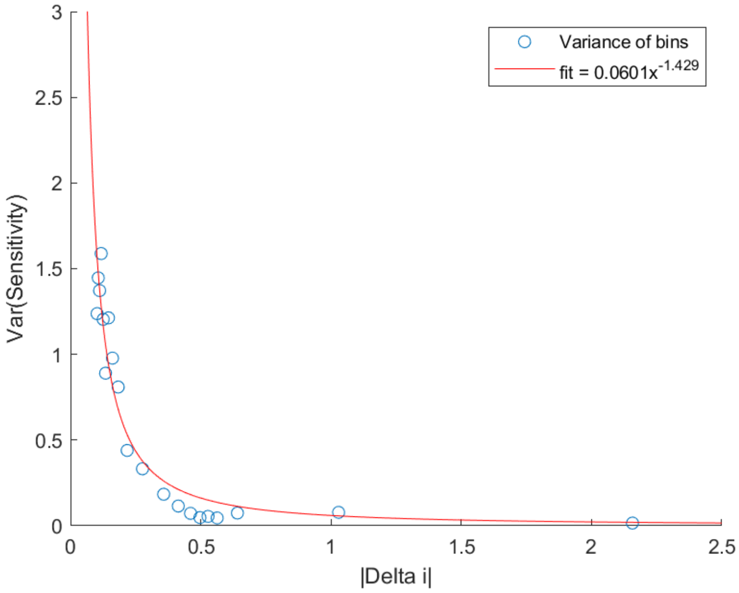

Fig. 5.5.: Exponential fit on the measurement noise

The relation that is found for α is:

$$\alpha = 100 * (0.0601 \Delta I_{real}^{-1.429}) \tag{5.3}$$

Since the imaginary part of the estimation does not yield the expected results as explained in Section 4.4, the fit for β is discarded. To keep the computational load for the estimator as if it would work, the relation for β is set equal to that of α as shown in Equation 5.4.

$$\beta = 100 * (0.0601 \Delta I_{imag}^{-1.429}) \tag{5.4}$$

5.4.2 Estimation results

Using the parameters as described above, the filter is tested on the data. Figure 5.6 shows estimations of the sensitivity that is predicted using the filter. All other estimations can be found in Appendix A.3. The expected value of these estimations is the real part of the cable impedance, as shown in Table 5.1, and is shown in the caption of the figures.

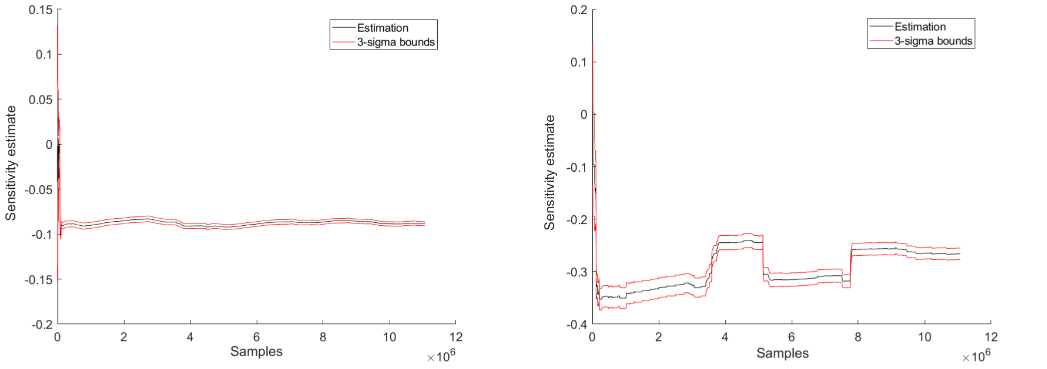

(a) Sensitivity estimate of ξ_2^{BA} with 3σ confidence, expected value from cable data: -0.08691

(b) Sensitivity estimate of ξ_3^{BB} with 3σ confidence, expected value from cable data: -0.510731

Fig. 5.6.: Kalman estimations

As can be observed in Figure 5.6, the behaviour of the filter differs between scenarios. In Figure 5.6a the filter converges, however in Figure 5.6b the estimation moves around much more. Furthermore, the confidence bounds are much more narrow for the estimation in Figure 5.6a compared to Figure 5.6b. This is due to the fact that the data for Figure 5.6b contains much less changes in power. Since the confidence in the measurement increases with an increase in change in current, the filter relies on larger changes in power to get to a more certain estimate.

5.4.3 Estimator startup behaviour

Initially, the sensitivity estimate of the filter is very uncertain. After a while, the KF will use the measurements to increase the certainty on the estimate, which can be observed in Figure 5.7.

As is depicted by the red 3σ confidence bounds in Figure 5.7, the confidence in the estimation increases after some time. Eventually, the filter reaches a certain steady state in which the confidence stays approximately constant. In Figure 5.7

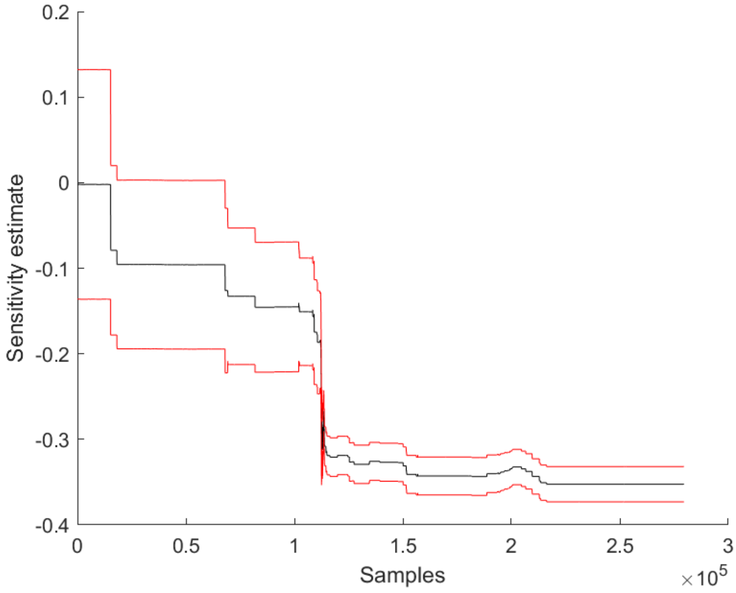

Fig. 5.7.: Startup behaviour of the estimator for ξ_3^{BB} with 3σ confidence

this can be seen at approximately $1.2 \cdot 10^5$ samples, which equals 40 minutes, given the $50Hz$ rate of the PMUs. How many samples are required to reach this steady state is dependant on the chosen filter parameters, and on the measurements. Since measurements with a high change in power increase the confidence most, a few of these samples are required to reach steady state. Obtaining these measurements is purely chance based, since there is no way of predicting the change in power. The longest observed time is $1.5 \cdot 10^5$ samples, or 50 minutes.

5.5 Comparing the results

To compare the results of the three estimation methods, the sorted errors are plotted together. Figure 5.8a shows the comparison for two sensitivity estimations. The comparison figures for all other estimations can be found in Appendix A.4.

As can be seen in Figure 5.8, the cable-data error and linear-fit error are approximately identical. The error from the estimator is different compared to these two. For some experiments the errors cross around 99% samples (as in Figure 5.8a), and for some experiments the online filter error always stays above the other two (as in Figure 5.8b). Specifically, this crossover of the errors is happening for the experiments where the voltage sensor of node A was used. The crossover is not present in the experiments where the voltage sensor of node B was used.

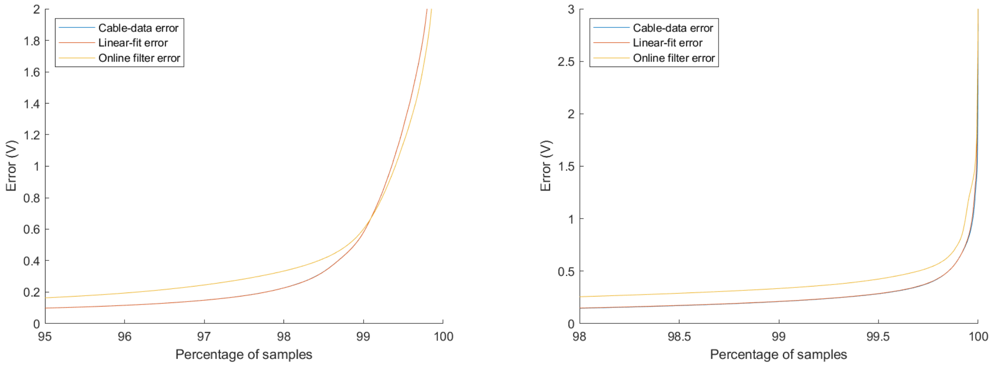

(a) ξ_3^{AB} comparison

(b) ξ_1^{BB} comparison

Fig. 5.8.: Comparison of errors in prediction

Figure 5.9 shows how close the cable-data- and linear-fit errors are. The figure shows approximately the first 80% of the figure, since the difference can then be observed.

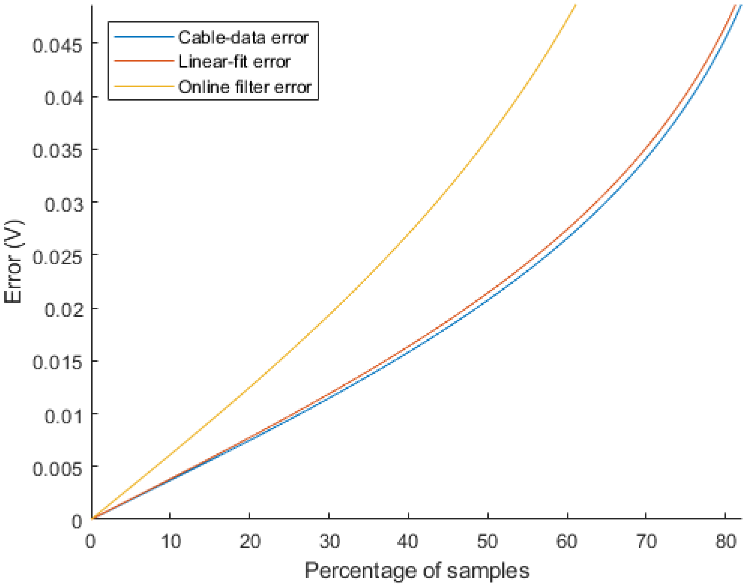

Fig. 5.9.: Comparison of cable-data and linear-fit error for ξ_1^{AA}

To allow concrete comparison between the methods, the RMSE is shown in Table 5.3.

As is depicted in Table 5.3, the linear-fit benchmark estimation performs similar to the cable-data ground truth, with a maximum deviation of $2.1mV$ for ξ_1^{BB}. For estimations BA and BB, the crossover behaviour is not present, and the online estimator has up to $30.8mV$ (for ξ_3^{BA} and ξ_1^{BB}) more RMSE compared to the ground

Tab. 5.3.: RMS of the errors

	Cable-data (V	Linear-fit (V)	Online estimator (V)
ξ_1^{AA}	0.2734	0.2735	0.2615
ξ_2^{AA}	0.2709	0.2711	0.2548
ξ_3^{AA}	0.2633	0.2632	0.2484
ξ_1^{AB}	0.2748	0.2748	0.2615
ξ_2^{AB}	0.2719	0.2719	0.2549
ξ_3^{AB}	0.2650	0.2651	0.2485
ξ_1^{BA}	0.0599	0.0604	0.0895
ξ_2^{BA}	0.0620	0.0620	0.0878
ξ_3^{BA}	0.0654	0.0653	0.0962
ξ_1^{BB}	0.0587	0.0608	0.0895
ξ_2^{BB}	0.0636	0.0625	0.0881
ξ_3^{BB}	0.0670	0.0662	0.0962

truth. For AA and AB however, the crossover behaviour is present, and the online estimator has up to $17.0mV$ (for ξ_2^{AB}) less RMSE compared to the ground truth. This does not provide the full picture however, since two distinct regions are present in the experiments where the errors cross. Therefore, additionally to the RMSE values presented in Table 5.3, Table 5.4 shows the RMSE of the data left and right of the split.

Tab. 5.4.: RMS of the errors with crossover behaviour where L and R denote the data left and right of point where the errors cross respectively

		Cable-data (V	Linear-fit (V)	Online estimator (V)
ξ_1^{AA}	L	0.1010	0.1018	0.1273
	R	3.1024	3.1000	2.7903
ξ_2^{AA}	L	0.0844	0.0844	0.1087
	R	2.9796	2.9824	2.669
ξ_3^{AA}	L	0.0838	0.0837	0.1058
	R	2.8544	2.8540	2.5713
ξ_1^{AB}	L	0.0986	0.0986	0.1220
	R	2.8760	2.8759	2.5946
ξ_2^{AB}	L	0.0874	0.0874	0.1091
	R	2.9203	2.9203	2.6138
ξ_3^{AB}	L	0.0808	0.0808	0.1006
	R	2.6597	2.6599	2.3950

As can be seen in the table, for the data left of the crossover point the online estimator has up to $26.3mv$ more RMSE (for ξ_1^{AA}). For the data right of the crossover however, the online estimator has up to $312.1mv$ less RMSE (for ξ_1^{AA}).

5.6 Magnitude of the error

Regardless of the estimation method, the error can reach relatively high values. This can be seen best in the unsorted error figures, as shown in Figure 5.10.

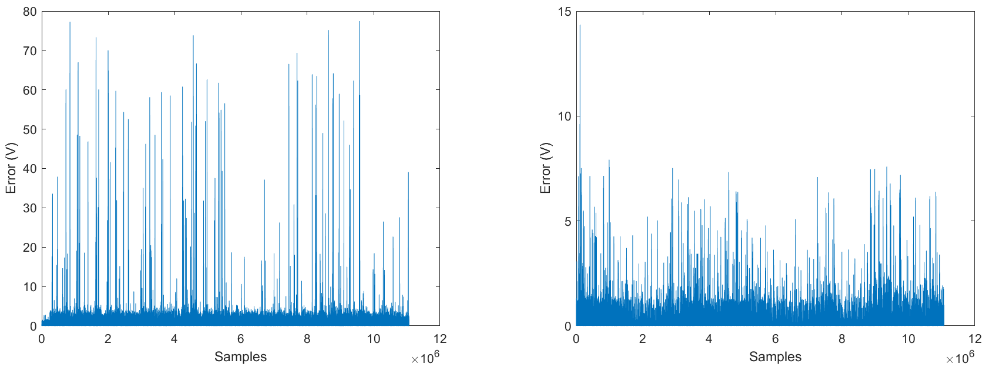

(a) Error for ξ_3^{AA} **(b)** Error for ξ_3^{BB}

Fig. 5.10.: Error in the cable-data estimations

Figure 5.10 shows that the error reaches relatively high values. For estimations where the voltage sensor at node A is used, the errors all look similar to Figure 5.10a with multiple peaks around $70V$, whereas for estimations where the voltage sensor at node B is used, the errors all look similar to Figure 5.10b, with peaks around $8V$. To explain where these large errors come from, Figure 5.11 shows ΔV and ΔI for the data with which Figure 5.10 was generated.

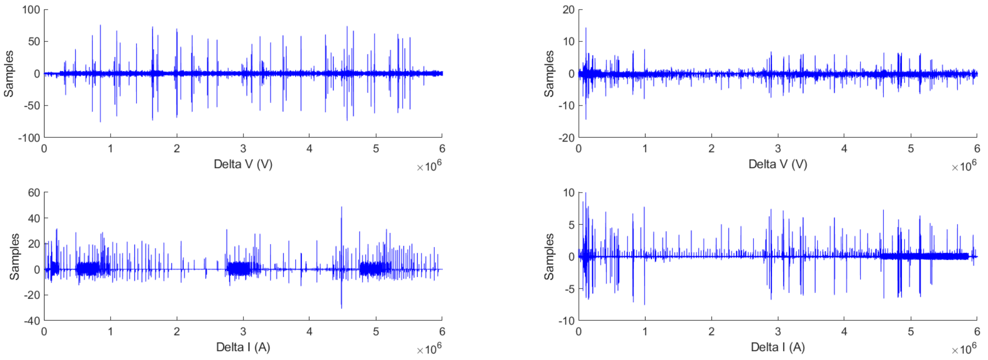

(a) Data for ξ_3^{AA} **(b)** Data for ξ_3^{BB}

Fig. 5.11.: Delta v and Delta I comparison

In Figure 5.11b, the maximum peaks in the ΔV data are approximately 5 to 10V, and a peak in can be seen in the ΔI data at the same time. In Figure 5.11a however, the voltage peaks have a much greater magnitude, of up to approximately $70V$, and the ΔI data does not always show a peak at the same time. Furthermore, the data for ΔI sometimes shows fairly high peaks, where ΔV is approximately 0. This results in the situation where sometimes a high change in voltage is predicted due to a high change in current, but not measured with the voltage sensors. Or the other way around, where it is not predicted, since the change in current is low, however the voltage sensor reports a very high peak. This data explains the high errors that can be found in some of the results.

5.7 Hardware requirements

Deploying the estimator on device is out of scope of this thesis, however the design is such that it can be deployed on lower level hardware like single board computers or microcontrollers. To analyze the hardware requirements, the required computational power and the memory requirement are investigated.

5.7.1 Computational load

This can be explained by looking at the required calculations for a filter iteration as specified in Section 4.4 and 4.2. In general, a distinction can be made between a naive- and optimized implementation. This distinction is explained with Equation 5.5 below.

$$x(n+1) = Fx(n) + Gu(n) \tag{5.5}$$

Since x is a vector of length 3, F a 3x3 matrix, u a vector of length 2 and G a 3x2 matrix, the naive implementation would result in 15 multiplications (9 for the Fx and 6 for Gu) and 3 additions. Looking more closely to the designed estimator however shows that this is not necessary. Since F is an identity matrix, and G has a value of 0 for 4 out of its 6 positions, the optimized implementation would result in 2 multiplications (for Gu) and 3 additions.

Table 5.5 shows the required number of operations for both a naive- and optimized implementation of the algorithm. For the total analysis, the concept of floating point operations (FLOPs) is used as an estimate of the computational complexity. The assumption is made that additions, multiplications, divisions, exponents, and arctan calculations consist of 1, 1, 5, 15, and 30 FLOPs respectively [60].

As is depicted in Table 5.5, the difference between a naive and optimized implementation can be substantial. Especially the matrix calculations for the predict- and

Tab. 5.5.: FLOPs for each calculation

		Naive						Optimized				
Equation number		Addition	Multiplication	Division	Exponent	Arctan	Matrix inversion	Addition	Multiplication	Division	Exponent	Arctan
Phasor processing	4.4	0	1	0	15	30	0	0	1	0	15	30
	4.18 and 4.23	1	2	0	0	0	0	1	2	0	0	0
	4.19	1	0	0	0	0	0	1	2	0	0	0
	4.20	1	0	0	0	0	0	1	0	0	0	0
	4.21	1	0	5	0	0	0	2	0	0	0	0
	4.22	1	0	0	0	0	0	1	0	5	0	0
	4.24	0	0	5	0	0	0	1	0	0	0	0
Predict step	4.6	3	15	0	0	0	0	3	2	0	0	0
	4.7	45	54	0	0	0	0	0	3	0	0	0
Update step	4.11	290	245	0	0	0	225	5	3	25	0	0
	4.12	30	30	0	0	0	0	6	3	0	0	0
	4.13	63	72	0	0	0	0	3	3	0	0	0
	5.3	0	1	0	15	0	0	0	1	0	15	0
	5.4	0	1	0	15	0	0	0	1	0	15	0
FLOPs per iteration							**1167**					**152**
kFLOPs per second							**58.35**					**7.6**

update step can be optimized very efficiently since many matrix positions contain 0. Additionally, the 5x5 matrix inversion that has to be done for Equation 4.11 can be replaced by 5 divisions since it is a diagonal matrix.

The number of FLOPs per second is obtained by multiplying the FLOPs per iteration with the data rate, which is $50Hz$ as explained in Section 3.2. Comparing this to the performance of the Raspberry-PI 4, it becomes clear that running the estimator on smaller scale hardware is possible. A list of FLOP rates of some hardware platforms is available at [61], where it can be seen that modern hardware platforms can reach in the range of GFLOPs per second, with the a Raspberry-Pi 4 that can reach approximately 9 to 10 GFLOPs per second. Compared to the required rate of 58.35 kFLOPs for the estimator or even 7.6 kFLOPs for an optimized implementation, the power that a single board computers provides is sufficient for this implementation.

5.7.2 Memory requirement

To have an estimate on the memory requirement of the estimator, all elements that need to be stored in memory can be summed. For this, the assumption is made that all numbers are stored as 32-bit floating point numbers. For this estimation, again a naive implementation is evaluated, where all required parameters are stored at the same time. In practice, a more optimized implementation is again feasible. Table 5.6 shows the required number of floating point numbers for the estimator.

Tab. 5.6.: Number of floating point numbers

Variable	x	P	F	G	u	Q	H	R	z	V_{phasor}	I_{phasor}	V	I_{real}	I_{imag}	I_0	ΔV	ΔI_{real}	ΔI_{imag}	ΔI_0
No. floats	3	9	9	6	2	9	15	25	5	2	2	1	1	1	1	1	1	1	1
																		Total	**95**

Multiplying the total number of floating point numbers from Table 5.6 with 32 bits, it becomes clear that there is a memory requirement of:

$$95 * 32bit = 3.04kbit = 0.38kB \tag{5.6}$$

Comparing this memory requirement to the same device list as presented in Section 5.7.1 [61], it can be seen that the memory requirement can also be satisfied. The Raspberry Pi 4 comes in multiple models which all have $> 1GB$ RAM available, showing that deployment of this estimator design is feasible on smaller scale hardware.

5.8 Conclusion

To summarize the results, looking at the error comparison it becomes clear that the online estimator performs worse than the linear-fit benchmark. Only in situations where the crossover in errors can be seen, the estimator outperforms the benchmark estimation in approximately the last 1% of samples. This behaviour is suspicious however, since it is only present in the situations where the ΔV peaks are very high, as explained in Section 5.6. Next to that, it also outperforms the ground truth estimation in this situation. While this is certainly possible because there is no guarantee that the ground truth is completely correct as explained in Section 4.5.1, understanding why the estimation is better than ground truth is required. Further investigation on any relation between these observations is needed, but out of scope of this thesis.

Although the online estimator does not perform as well as the linear-fit benchmark, the value of the error is not so high that the estimation is always unusable. The increase in error might be acceptable in certain use-cases, where other benefits of the method might be more important. Since the estimator keeps tracking the sensitivity, it can never get stuck on a completely wrong estimation for ever, whereas other methods might need user interaction to prevent this. Combined with the fact that the implementation is indeed lightweight and tailored towards deployment on smaller-scale hardware, this estimator can be a adequate solution for specific applications.

6 Conclusion

In this study, the sensitivity between residential distribution grid connections was estimated using an online Kalman filter approach. The results of this thesis are used to answer the main research question:

How can the sensitivity between residential distribution grid connections be accurately estimated in an online approach?

To best answer the main research question, all sub-questions are addressed individually first.

How can the sensitivity parameter be modelled?
In literature, various definitions of the sensitivity parameter are defined. The definition as given in [11] is used for the estimator in this thesis with the adaptation of changing the power to the current as explained in Section 4.1:

$$\xi^{kj}_{a,real}(t) = \frac{\Delta V^k_a(t)}{\Delta I^j_{a,real}(t)} \tag{6.1}$$

$$\xi^{kj}_{a,imag}(t) = \frac{\Delta V^k_a(t)}{\Delta I^j_{a,imag}(t)} \tag{6.2}$$

What information is needed for estimating the sensitivity?
The parametric definition of the sensitivity requires voltage and current phasors, real-time PMU measurements at $50Hz$ from synchronised sensors are sufficient to make the estimation.

How many samples are required to find an accurate estimation?
The estimators accuracy converges to its best value after approximately $1.2 \cdot 10^5$ samples, with a maximum observed value of $1.5 \cdot 10^5$ samples as explained in Section 5.4.3. Since the phasor measurements are sampled at $50Hz$, this means a maximum observed time of 50 minutes before the filter reaches its stable accuracy.

To what degree of accuracy can the sensitivity be found by the estimator?
The performed experiments showed that the online estimator is able to provide the estimation with up to $38mV$ additional RMSE over all datasets, however the estimator performs better compared to the benchmark in specific scenarios. In

experiments where the sorted errors cross, the online estimator has lower estimation errors for approximately the last 1% of samples.

What hardware is required to run the estimator online?
Finally, the fourth sub-question is addressed with the results of Section 5.7. Deploying the estimator on device was out of scope of this thesis due to the available time, however theoretically this question can be answered. Since the estimator is a regular Kalman filter, estimator steps consist of a few matrix/vector calculations. Furthermore, the estimator tracks only 3 states for a given sensitivity, which means that these matrix calculations are relatively lightweight, especially when a more optimized implementation is constructed. Additionally, the fact that the filter combines all previous knowledge in the current estimate means that no additional data has to be stored, keeping the memory requirement low as well. Altogether, this estimator is very lightweight, and low level hardware platforms such as microcontrollers or single board computers are more than capable to facilitate deployment.

In conclusion, coming back to the main research question; accurately estimating the sensitivity between residential distribution grid connections in an online approach requires a comprehensive understanding of the grid's behavior, the use of real-time data, and appropriate modeling techniques. The findings of this research offer valuable guidance for designing effective sensitivity estimators, which can play a crucial role in ensuring fairness in residential PV-curtailment applications. As the field of smart grids continues to evolve, the insights gained from this study facilitate further advancements and optimizations in grid management and operation.

6.1 Future work and Recommendations

This section presents ideas and directions for future work based on observations done in this thesis for the field of estimating LV-grid parameters.

6.1.1 Active estimation

In this thesis, a passive, non-invasive estimation method is used by utilizing PMUs. In applications where some grid disturbance is tolerated, active estimation methods are a really nice fit to the PV-inverter application. Active methods can be applied very efficiently in the case of a PV-inverter since all required hardware for achieving this is in-place in the form of solar panels and their inverter. Generating discrete steps in output power for instance yields minimal grid disturbance, since the power consumption or production might change during normal operation as well, and can give significant information to the estimator.

6.1.2 Required sensors

For this research, PMU measurements have been used to make the estimation. While these measurements are becoming more and more common in the distribution grid as an effect of the energy transition, an estimator relying on more easily obtainable data might be possible. Experiments with e.g. smart meter data could provide the insight in whether or not this is possible, potentially simplifying the estimator and making an implementation less expensive.

6.1.3 Imaginary part of impedance estimation

As shown in Section 5.3, the method does not function as expected for the imaginary part of the impedance estimation. This is likely a result of phase drift in the PMU measurements. A part of the change in phase in the measurements is an effect of the imaginary part of the feeder impedance, however another part is due to the difference in sample rate and grid frequency. This problem is addressed in the paper on parameter estimation with compensation for phase drift [38].

This implementation was not feasible for this thesis unfortunately due to time constraints. Furthermore, the data used for the estimator in this thesis does not include the required frequency information. The sensors that are used in the project are capable of outputting this data however, so testing this solution is possible with the current measurement setup.

6.1.4 Separate or combined estimation

For this work, the PMU measurements are separated in a real and imaginary part before the estimator. It might also be worthwhile to investigate if a combined estimator works better compared to a separate estimator. A combined estimator would track the complex sensitivity as a single state, as opposed to the two separate sensitivities as presented in this thesis.

Bibliography

[1] G. A. Pagani and M. Aiello, “From the grid to the smart grid, topologically,” *Physica A: Statistical Mechanics and its Applications*, vol. 449, pp. 160–175, 2016, ISSN: 0378-4371. DOI: https://doi.org/10.1016/j.physa.2015.12.080. [Online]. Available: https://www.sciencedirect.com/science/article/pii/S0378437115011085.

[2] H. Sadeghian, M. H. Athari, and Z. Wang, “Optimized solar photovoltaic generation in a real local distribution network,” in *2017 IEEE Power & Energy Society Innovative Smart Grid Technologies Conference (ISGT)*, 2017, pp. 1–5. DOI: 10.1109/ISGT.2017.8086067.

[3] IEA, *Energy transitions Tracking progress in clean energy transitions through key indicators across fuels and technologies*. [Online]. Available: https://www.iea.org/topics/energy-transitions (last visted at 09/29/2023).

[4] Irena, *Energy transition outlook*. [Online]. Available: https://www.irena.org/Energy-Transition/Outlook (last visted at 09/29/2023).

[5] NOS. “Knipperende lampen of zelfs uitval: Alliander waarschuwt voor vol stroomnet.” (Mar. 2023), [Online]. Available: https://nos.nl/artikel/2466776-knipperende-lampen-of-zelfs-uitval-alliander-waarschuwt-voor-vol-stroomnet (last visted at 09/29/2023).

[6] Alliander. “Ook elektriciteitsnet in woonwijk loopt tegen grenzen aan.” (Mar. 2023), [Online]. Available: https://www.alliander.com/nl/financieel-nieuws/ook-elektriciteitsnet-in-woonwijk-loopt-tegen-grenzen-aan/ (last visted at 09/29/2023).

[7] Sibelga, *Why does the electricity grid have to stay in balance?* [Online]. Available: https://www.energuide.be/en/questions-answers/why-does-the-electricity-grid-have-to-stay-in-balance/2136/ (last visted at 09/29/2023).

[8] E. Klaassen, J. Frunt, and H. Slootweg, “Assessing the impact of distributed energy resources on LV grids using practical measurements,” *CIRED 23rd International Conference on Electricity Distribution*, Jun. 2015.

[9] M. Klement, V. Schepel, and A. Tozzi, *Meteorologische data portaal*. [Online]. Available: https://www.tudelft.nl/?id=59090 (last visted at 09/29/2023).

[10] “RfG (Requirements for Generators) Regulations (EU) 2016/631.” (2016), [Online]. Available: https://eur-lex.europa.eu/legal-content/EN/TXT/?uri=OJ%3AJOL_2016_112_R_0001 (last visted at 09/29/2023).

[11] A. Vadavathi, G. Hoogsteen, and J. Hurink, “PV Inverter Based Fair Power Quality Control,” *IEEE Transactions on Smart Grid*, pp. 1–1, 2023. DOI: 10.1109/TSG.2023.3244601.

[12] SST. “Smart State Technology website.” (2023), [Online]. Available: https://smartstatetechnology.nl/ (last visted at 09/29/2023).

[13] P. van Oirsouw, *Netten voor distributie van elektriciteit*, ISBN: 9789081798310. [Online]. Available: https://phasetophase.nl/boek/index.html (last visted at 07/03/2023).

[14] NEN, “EN 50160:2022 Spanningskarakteristieken in openbare elektriciteitsnetten,” 2022. [Online]. Available: https://www.nen.nl/nen-en-50160-2022-en-305139 (last visted at 09/29/2023).

[15] C. L. Fortescue, “Method of Symmetrical Co-Ordinates Applied to the Solution of Polyphase Networks,” *Transactions of the American Institute of Electrical Engineers*, vol. XXXVII, no. 2, pp. 1027–1140, 1918. DOI: 10.1109/T-AIEE.1918.4765570.

[16] B. Zakeri, S. Cross, P. Dodds, and G. C. Gissey, “Policy options for enhancing economic profitability of residential solar photovoltaic with battery energy storage,” *Applied Energy*, vol. 290, p. 116 697, 2021, ISSN: 0306-2619. DOI: https://doi.org/10.1016/j.apenergy.2021.116697. [Online]. Available: https://www.sciencedirect.com/science/article/pii/S0306261921002221.

[17] J. Liu, X. Chen, S. Cao, and H. Yang, “Overview on hybrid solar photovoltaic-electrical energy storage technologies for power supply to buildings,” *Energy Conversion and Management*, vol. 187, pp. 103–121, 2019, ISSN: 0196-8904. DOI: https://doi.org/10.1016/j.enconman.2019.02.080. [Online]. Available: https://www.sciencedirect.com/science/article/pii/S0196890419302900.

[18] Y. Z. Gerdroodbari, R. Razzaghi, and F. Shahnia, “Improving Voltage Regulation and Unbalance in Distribution Networks Using Peer-to-Peer Data Sharing Between Single-Phase PV Inverters,” *IEEE Transactions on Power Delivery*, vol. 37, no. 4, pp. 2629–2639, 2022. DOI: 10.1109/TPWRD.2021.3113011.

[19] C. G. Bajo, S. Hashemi, S. B. Kjsær, G. Yang, and J. Østergaard, “Voltage unbalance mitigation in LV networks using three-phase PV systems,” in *2015 IEEE International Conference on Industrial Technology (ICIT)*, 2015, pp. 2875–2879. DOI: 10.1109/ICIT.2015.7125522.

[20] S. Paudyal, B. P. Bhattarai, R. Tonkoski, S. Dahal, and O. Ceylan, “Comparative Study of Active Power Curtailment Methods of PVs for Preventing Overvoltage on Distribution Feeders,” in *2018 IEEE Power & Energy Society General Meeting (PESGM)*, 2018, pp. 1–5. DOI: 10.1109/PESGM.2018.8585526.

[21] A. Agrawal, K. Rahimi, R. P. Broadwater, and J. Bank, “Performance of PV generation feedback controllers: Power factor versus Volt-VAR control strategies,” in *2015 North American Power Symposium (NAPS)*, 2015, pp. 1–6. DOI: 10.1109/NAPS.2015.7335080.

[22] Q. Nguyen, H. V. Padullaparti, K.-W. Lao, S. Santoso, X. Ke, and N. Samaan, "Exact Optimal Power Dispatch in Unbalanced Distribution Systems With High PV Penetration," *IEEE Transactions on Power Systems*, vol. 34, no. 1, pp. 718–728, 2019. DOI: 10.1109/TPWRS.2018.2869195.

[23] A. R. Vadavathi, G. Hoogsteen, and J. L. Hurink, "Comparison of Fairness based Coordinated Grid Voltage Control Methods for PV Inverters," in *2021 IEEE PES Innovative Smart Grid Technologies Europe (ISGT Europe)*, 2021, pp. 1–5. DOI: 10.1109/ISGTEurope52324.2021.9639982.

[24] R. Tonkoski, L. A. C. Lopes, and T. H. M. El-Fouly, "Coordinated Active Power Curtailment of Grid Connected PV Inverters for Overvoltage Prevention," *IEEE Transactions on Sustainable Energy*, vol. 2, no. 2, pp. 139–147, 2011. DOI: 10.1109/TSTE.2010.2098483.

[25] Y. Z. Gerdroodbari, R. Razzaghi, and F. Shahnia, "Decentralized Control Strategy to Improve Fairness in Active Power Curtailment of PV Inverters in Low-Voltage Distribution Networks," *IEEE Transactions on Sustainable Energy*, vol. 12, no. 4, pp. 2282–2292, 2021. DOI: 10.1109/TSTE.2021.3088873.

[26] M. Z. Liu, A. T. Procopiou, K. Petrou, *et al.*, "On the Fairness of PV Curtailment Schemes in Residential Distribution Networks," *IEEE Transactions on Smart Grid*, vol. 11, no. 5, pp. 4502–4512, 2020. DOI: 10.1109/TSG.2020.2983771.

[27] R. Jain, D. Chiu, and W. Hawe, *A Quantitative Measure Of Fairness And Discrimination For Resource Allocation In Shared Computer Systems*, 1998. arXiv: cs/9809099 [cs.NI].

[28] M. K. De Meerendre, E. Prieto-Araujo, K. H. Ahmed, O. Gomis-Bellmunt, L. Xu, and A. Egea-Àlvarez, "Review of Local Network Impedance Estimation Techniques," *IEEE Access*, vol. 8, pp. 213 647–213 661, 2020. DOI: 10.1109/ACCESS.2020.3040099.

[29] J. Zhao, A. Gómez-Expósito, M. Netto, *et al.*, "Power System Dynamic State Estimation: Motivations, Definitions, Methodologies, and Future Work," *IEEE Transactions on Power Systems*, vol. 34, no. 4, pp. 3188–3198, 2019. DOI: 10.1109/TPWRS.2019.2894769.

[30] B. Arif, L. Tarisciotti, P. Zanchetta, J. C. Clare, and M. Degano, "Grid Parameter Estimation Using Model Predictive Direct Power Control," *IEEE Transactions on Industry Applications*, vol. 51, no. 6, pp. 4614–4622, 2015. DOI: 10.1109/TIA.2015.2453132.

[31] S. Han, D. Kodaira, S. Han, B. Kwon, Y. Hasegawa, and H. Aki, "An Automated Impedance Estimation Method in Low-Voltage Distribution Network for Coordinated Voltage Regulation," *IEEE Transactions on Smart Grid*, vol. 7, no. 2, pp. 1012–1020, 2016. DOI: 10.1109/TSG.2015.2489199.

[32] V. Ćuk, J. F. G. Cobben, W. Kling, and P. F. Ribeiro, "Considerations on harmonic impedance estimation in low voltage networks," in *2012 IEEE 15th International Conference on Harmonics and Quality of Power*, 2012, pp. 358–363. DOI: 10.1109/ICHQP.2012.6381250.

[33] N. Mohammed, T. Kerekes, and M. Ciobotaru, "An Online Event-Based Grid Impedance Estimation Technique Using Grid-Connected Inverters," *IEEE Transactions on Power Electronics*, vol. 36, no. 5, pp. 6106–6117, 2021. DOI: 10.1109/TPEL.2020.3029872.

[34] H.-Y. Su and T.-Y. Liu, "Robust Thevenin Equivalent Parameter Estimation for Voltage Stability Assessment," *IEEE Transactions on Power Systems*, vol. 33, no. 4, pp. 4637–4639, 2018. DOI: 10.1109/TPWRS.2018.2821926.

[35] U. Hashmi, R. Choudhary, and J. G. Priolkar, "Online thevenin equivalent parameter estimation using nonlinear and linear recursive least square algorithm," in *2015 IEEE International Conference on Electrical, Computer and Communication Technologies (ICECCT)*, 2015, pp. 1–6. DOI: 10.1109/ICECCT.2015.7225946.

[36] M. Moghimi Haji and W. Xu, "Online Determination of External Network Models Using Synchronized Phasor Data," *IEEE Transactions on Smart Grid*, vol. 9, no. 2, pp. 635–643, 2018. DOI: 10.1109/TSG.2016.2559486.

[37] P. Abdi, M.-E. Hamedani-Golshan, H. H. Alhelou, and F. Milano, "A PMU-Based Method for On-Line Thévenin Equivalent Estimation," *IEEE Transactions on Power Systems*, vol. 37, no. 4, pp. 2796–2807, 2022. DOI: 10.1109/TPWRS.2021.3125007.

[38] B. Alinezhad and H. Kazemi Karegar, "On-Line Thévenin Impedance Estimation Based on PMU Data and Phase Drift Correction," *IEEE Transactions on Smart Grid*, vol. 9, no. 2, pp. 1033–1042, 2018. DOI: 10.1109/TSG.2016.2574765.

[39] A. V. Timbus, P. Rodriguez, R. Teodorescu, and M. Ciobotaru, "Line Impedance Estimation Using Active and Reactive Power Variations," in *2007 IEEE Power Electronics Specialists Conference*, 2007, pp. 1273–1279. DOI: 10.1109/PESC.2007.4342176.

[40] J. Zhao, G. Zhang, Z. Y. Dong, and M. La Scala, "Robust Forecasting Aided Power System State Estimation Considering State Correlations," *IEEE Transactions on Smart Grid*, vol. 9, no. 4, pp. 2658–2666, 2018. DOI: 10.1109/TSG.2016.2615473.

[41] A. Arefi, G. Ledwich, and B. Behi, "An Efficient DSE Using Conditional Multivariate Complex Gaussian Distribution," *IEEE Transactions on Smart Grid*, vol. 6, no. 4, pp. 2147–2156, 2015. DOI: 10.1109/TSG.2014.2385871.

[42] A. Primadianto and C.-N. Lu, "A Review on Distribution System State Estimation," *IEEE Transactions on Power Systems*, vol. 32, no. 5, pp. 3875–3883, 2017. DOI: 10.1109/TPWRS.2016.2632156.

[43] R. E. Kalman, "A New Approach to Linear Filtering and Prediction Problems," *Transactions of the ASME–Journal of Basic Engineering*, vol. 82, no. Series D, pp. 35–45, 1960.

[44] J. Fang, H. Deng, and S. M. Goetz, "Grid Impedance Estimation Through Grid-Forming Power Converters," *IEEE Transactions on Power Electronics*, vol. 36, no. 2, pp. 2094–2104, 2021. DOI: 10.1109/TPEL.2020.3010874.

[45] M. Vauhkonen, P. Karjalainen, and J. Kaipio, "A Kalman filter approach to track fast impedance changes in electrical impedance tomography," *IEEE Transactions on Biomedical Engineering*, vol. 45, no. 4, pp. 486–493, 1998. DOI: 10.1109/10.664204.

[46] N. Hoffmann and F. W. Fuchs, “Minimal Invasive Equivalent Grid Impedance Estimation in Inductive–Resistive Power Networks Using Extended Kalman Filter,” *IEEE Transactions on Power Electronics*, vol. 29, no. 2, pp. 631–641, 2014. DOI: 10.1109/TPEL.2013.2259507.

[47] J. Ye, Z. Zhang, A. Shen, J. Xu, and F. Wu, “Kalman filter based grid impedance estimating for harmonic order scheduling method of active power filter with output LCL filter,” in *2016 International Symposium on Power Electronics, Electrical Drives, Automation and Motion (SPEEDAM)*, 2016, pp. 359–364. DOI: 10.1109/SPEEDAM.2016.7525967.

[48] Z. Huang, K. Schneider, and J. Nieplocha, “Feasibility studies of applying Kalman Filter techniques to power system dynamic state estimation,” in *2007 International Power Engineering Conference (IPEC 2007)*, 2007, pp. 376–382.

[49] D. V. Do, C. Forgez, K. El Kadri Benkara, and G. Friedrich, “Impedance Observer for a Li-Ion Battery Using Kalman Filter,” *IEEE Transactions on Vehicular Technology*, vol. 58, no. 8, pp. 3930–3937, 2009. DOI: 10.1109/TVT.2009.2028572.

[50] E. Wan and R. Van Der Merwe, “The unscented Kalman filter for nonlinear estimation,” in *Proceedings of the IEEE 2000 Adaptive Systems for Signal Processing, Communications, and Control Symposium (Cat. No.00EX373)*, 2000, pp. 153–158. DOI: 10.1109/ASSPCC.2000.882463.

[51] G. A. Terejanu, “Unscented Kalman Filter Tutorial,” *University at Buffalo, Buffalo*, May 2011.

[52] M. J. Hossain and M. Naeini, “Multi-Area Distributed State Estimation in Smart Grids Using Data-Driven Kalman Filters,” *Energies*, vol. 15, no. 19, 2022, ISSN: 1996-1073. DOI: 10.3390/en15197105. [Online]. Available: https://www.mdpi.com/1996-1073/15/19/7105.

[53] N. Veerakumar, D. Ćetenović, K. Kongurai, M. Popov, A. Jongepier, and V. Terzija, “PMU-based Real-time Distribution System State Estimation Considering Anomaly Detection, Discrimination and Identification,” *International Journal of Electrical Power & Energy Systems*, vol. 148, p. 108 916, 2023, ISSN: 0142-0615. DOI: https://doi.org/10.1016/j.ijepes.2022.108916. [Online]. Available: https://www.sciencedirect.com/science/article/pii/S0142061522009127.

[54] M. Katzfuss, J. R. Stroud, and C. K. Wikle, “Understanding the Ensemble Kalman Filter,” in *The American Statistician*, vol. 70, Taylor & Francis, 2016, pp. 350–357. DOI: 10.1080/00031305.2016.1141709.

[55] G. Evensen, “The ensemble Kalman filter for combined state and parameter estimation,” *IEEE Control Systems Magazine*, vol. 29, no. 3, pp. 83–104, 2009. DOI: 10.1109/MCS.2009.932223.

[56] W. S. Rosenthal, A. M. Tartakovsky, and Z. Huang, “Ensemble Kalman Filter for Dynamic State Estimation of Power Grids Stochastically Driven by Time-Correlated Mechanical Input Power,” *IEEE Transactions on Power Systems*, vol. 33, no. 4, pp. 3701–3710, 2018. DOI: 10.1109/TPWRS.2017.2764492.

[57] P. Djuric, J. Kotecha, J. Zhang, *et al.*, “Particle filtering,” *IEEE Signal Processing Magazine*, vol. 20, no. 5, pp. 19–38, 2003. DOI: 10.1109/MSP.2003.1236770.

[58] T. Chen, J. Morris, and E. Martin, “Particle filters for state and parameter estimation in batch processes,” *Journal of Process Control*, vol. 15, no. 6, pp. 665–673, 2005, ISSN: 0959-1524. DOI: https://doi.org/10.1016/j.jprocont.2005.01.001. [Online]. Available: https://www.sciencedirect.com/science/article/pii/S095915240500017X.

[59] J. Zhu, Z. Shi, H. Liang, R. Lu, and X. Shen, “Particle filter based grid synchronization with voltage unbalance and frequency variation in smart grid,” in *2013 International Conference on Wireless Communications and Signal Processing*, 2013, pp. 1–6. DOI: 10.1109/WCSP.2013.6677079.

[60] L. Atkinson. “A simple benchmark of various math operations.” (Nov. 2014), [Online]. Available: https://latkin.org/blog/2014/11/09/a-simple-benchmark-of-various-math-operations/ (last visted at 09/29/2023).

[61] V. Weaver. “The GFLOPS/W of the various machines in the VMW Research Group.” (), [Online]. Available: https://web.eece.maine.edu/~vweaver/group/green_machines.html (last visted at 10/02/2023).

Acronyms

AC alternating current. 7

APC active power curtailment. 12, 13, 23, 29

DER distributed energy resource. 1, 7, 15, 23

DSE dynamic state estimation. 16, 17

DSO distribution system operator. 7, 13

EKF extended Kalman filter. 21–23

EnKF ensemble Kalman filter. 22, 23

FASE forecasting-aided state estimation. 16, 17

FLOP floating point operation. 50, 51

HV high voltage. 1

KCL Kirchhoff’s current law. 10

KF Kalman filter. 18, 20, 22, 23, 30–33, 44, 45

KVL Kirchhoff’s voltage law. 10

LV low voltage. v, 1, 3, 4, 7, 10, 11, 25–27, 29, 54, 65

MV medium voltage. 1, 26

OPF optimal power flow. 12

PCC point of common coupling. 15

PF particle filter. 23

PMU phasor measurement unit. 3, 15, 17, 23, 25, 27, 28, 46, 53–55, 65

PQ power quality. 7, 14, 68

PV photovoltaic. v, 1–4, 10–13, 15, 16, 23, 54

RES renewable energy source. v, 1, 3

RMSE root-mean-square error. 41, 47, 48, 53

SE state estimation. 13, 16, 17

SSE static state estimation. 16, 17

SST Smart State Technology. 3, 25, 27, 28, 65

TE Thévenin equivalent. 14–16, 65

TSE tracking state estimation. 16, 17

UKF unscented Kalman filter. 22

List of Figures

List of Tables

Appendix

A

A.1 Cable-data results figures

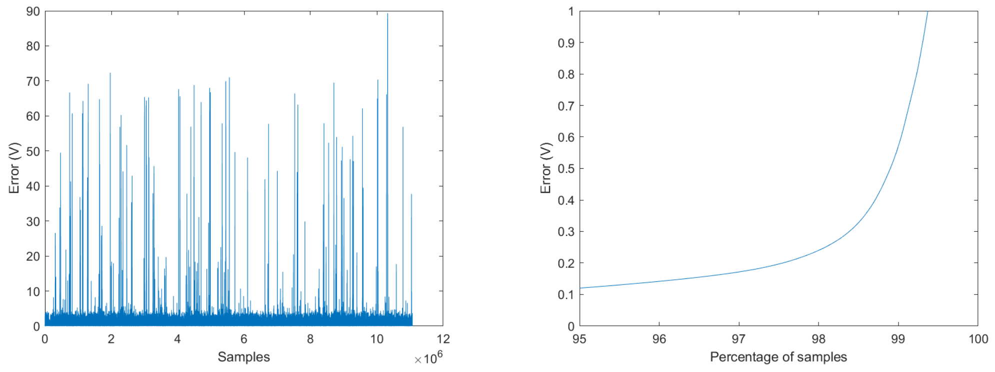

(a) Unsorted error

(b) Sorted error

Fig. A.1.: Error in the cable-data estimation ξ_1^{AA}

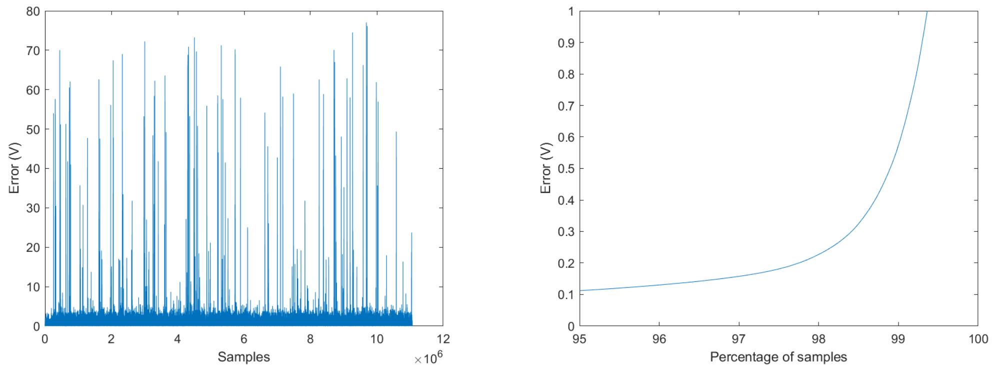

(a) Unsorted error

(b) Sorted error

Fig. A.2.: Error in the cable-data estimation ξ_2^{AA}

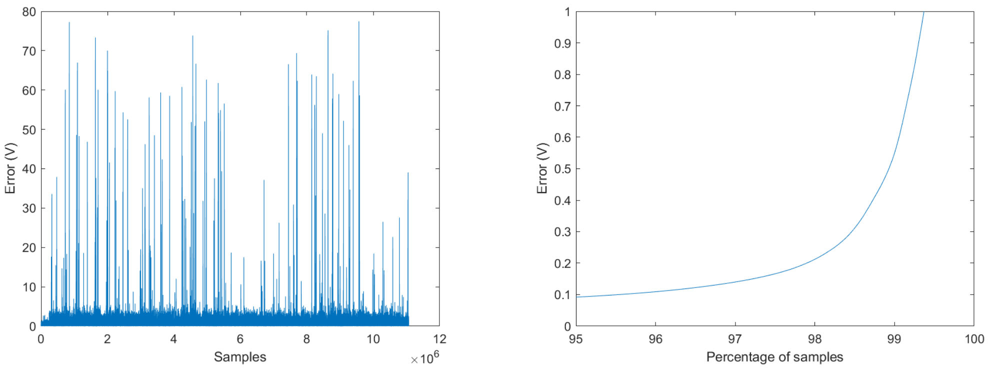

(a) Unsorted error

(b) Sorted error

Fig. A.3.: Error in the cable-data estimation ξ_3^{AA}

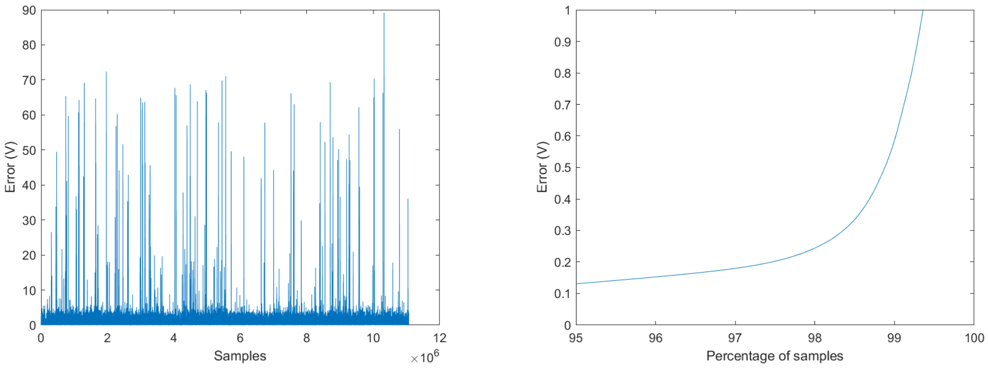

(a) Unsorted error

(b) Sorted error

Fig. A.4.: Error in the cable-data estimation ξ_1^{AB}

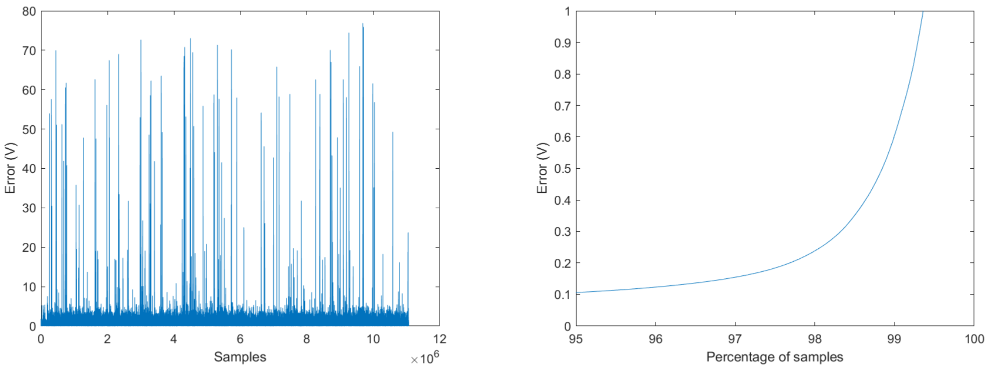

(a) Unsorted error

(b) Sorted error

Fig. A.5.: Error in the cable-data estimation ξ_2^{AB}

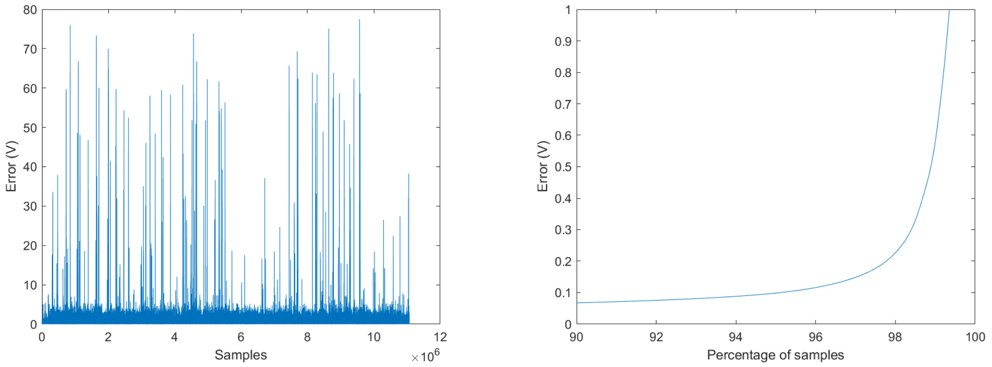

(a) Unsorted error

(b) Sorted error

Fig. A.6.: Error in the cable-data estimation ξ_3^{AB}

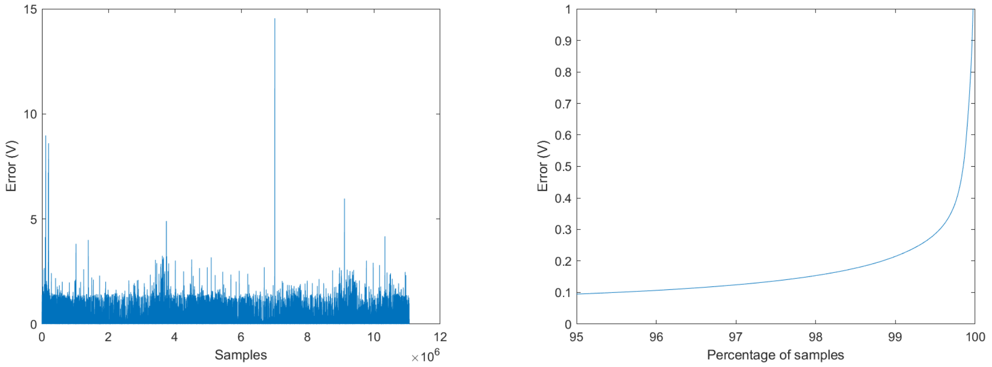

(a) Unsorted error

(b) Sorted error

Fig. A.7.: Error in the cable-data estimation ξ_1^{BA}

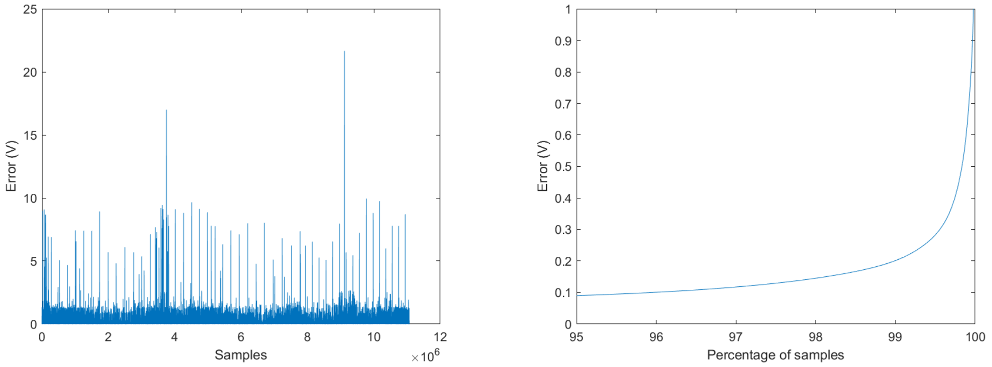

(a) Unsorted error

(b) Sorted error

Fig. A.8.: Error in the cable-data estimation ξ_2^{BA}

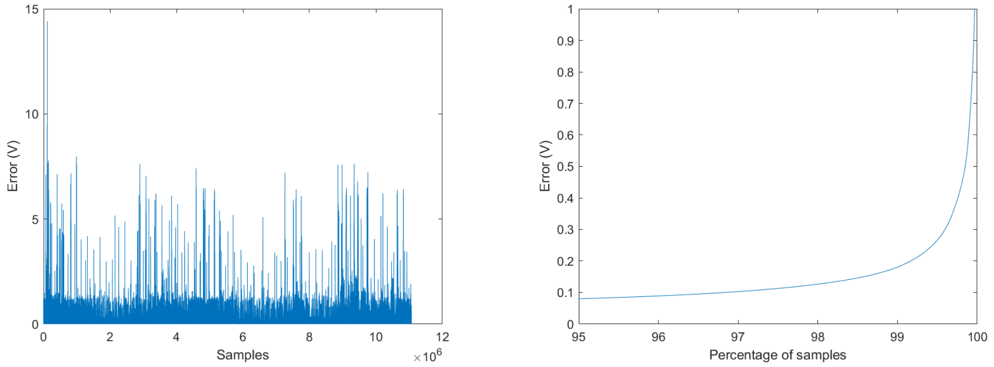

(a) Unsorted error

(b) Sorted error

Fig. A.9.: Error in the cable-data estimation ξ_3^{BA}

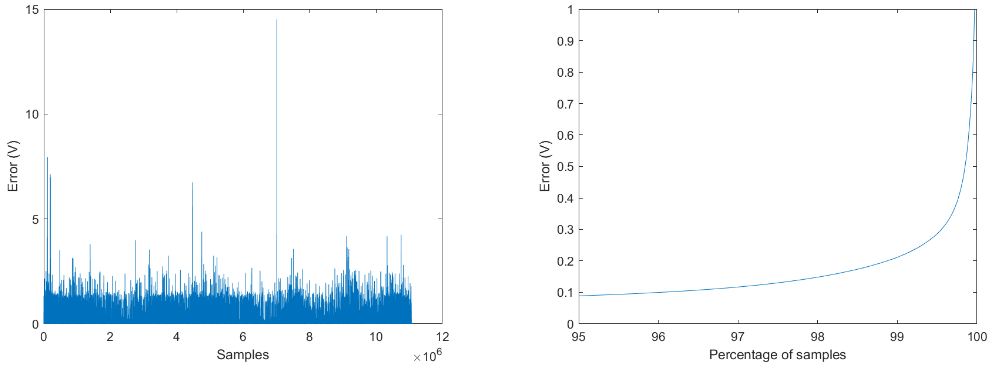

(a) Unsorted error

(b) Sorted error

Fig. A.10.: Error in the cable-data estimation ξ_1^{BB}

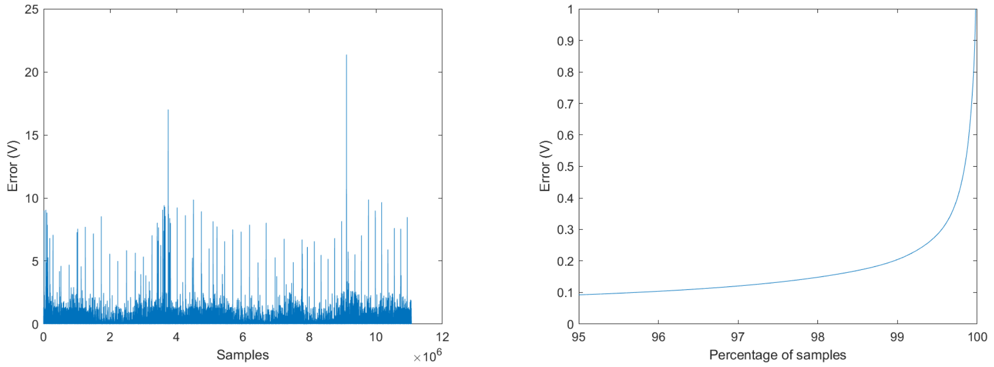

(a) Unsorted error

(b) Sorted error

Fig. A.11.: Error in the cable-data estimation ξ_2^{BB}

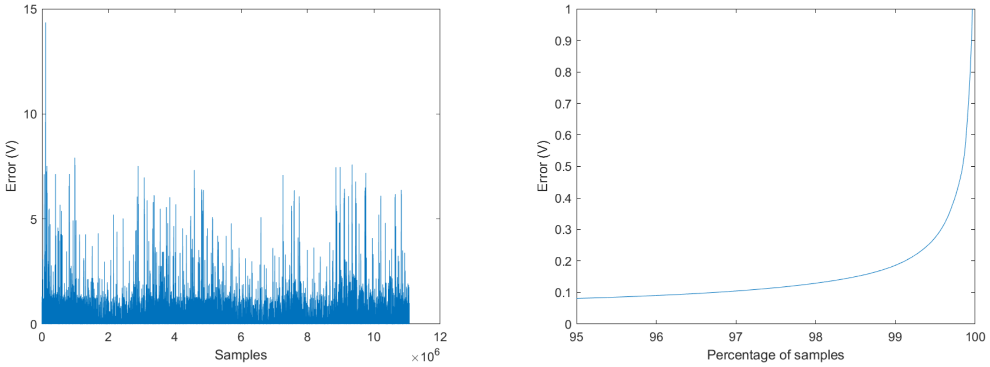

(a) Unsorted error

(b) Sorted error

Fig. A.12.: Error in the cable-data estimation ξ_3^{BB}

A.2 Linear-fit results figures

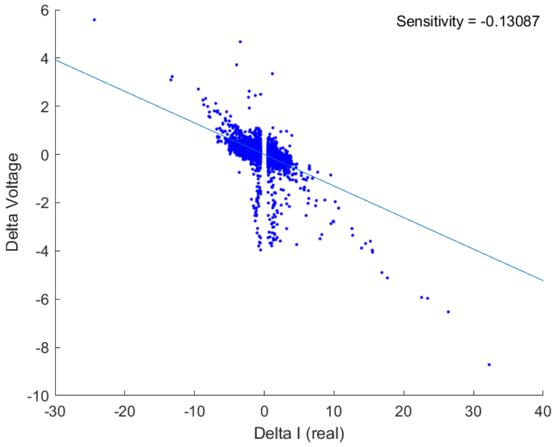

Fig. A.13.: Linear-fit estimation ξ_1^{AA}

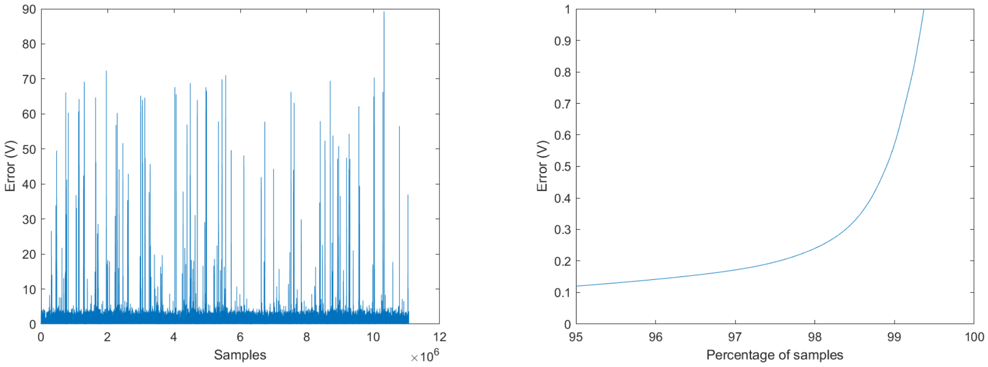

(a) Unsorted error

(b) Sorted error

Fig. A.14.: Error in the linear-fit estimation ξ_1^{AA}

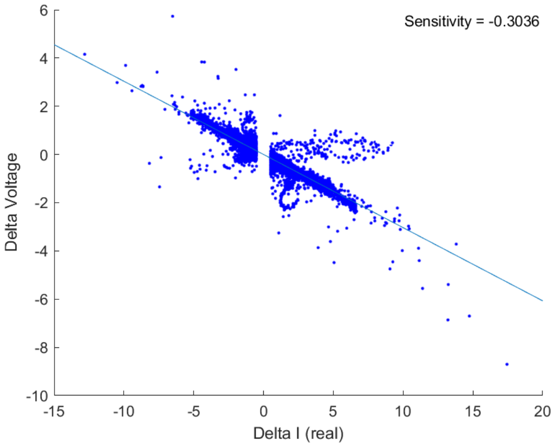

Fig. A.15.: Linear-fit estimation ξ_2^{AA}

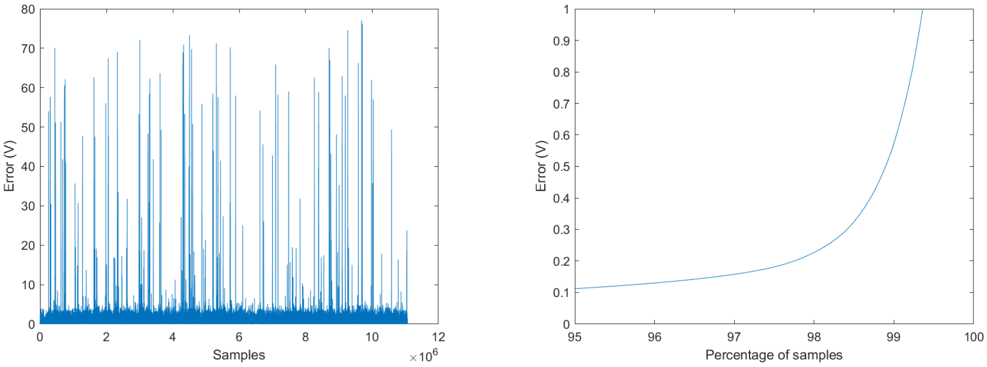

(a) Unsorted error

(b) Sorted error

Fig. A.16.: Error in the linear-fit estimation ξ_2^{AA}

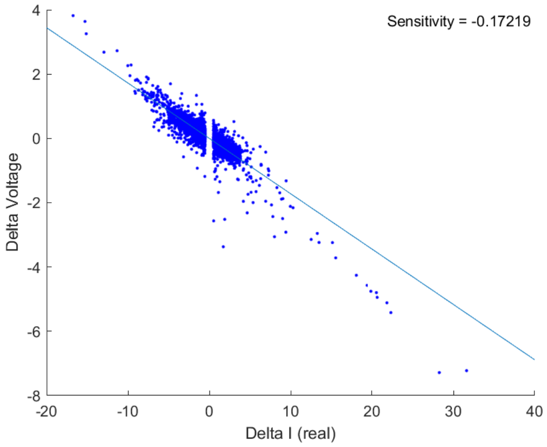

Fig. A.17.: Linear-fit estimation ξ_3^{AA}

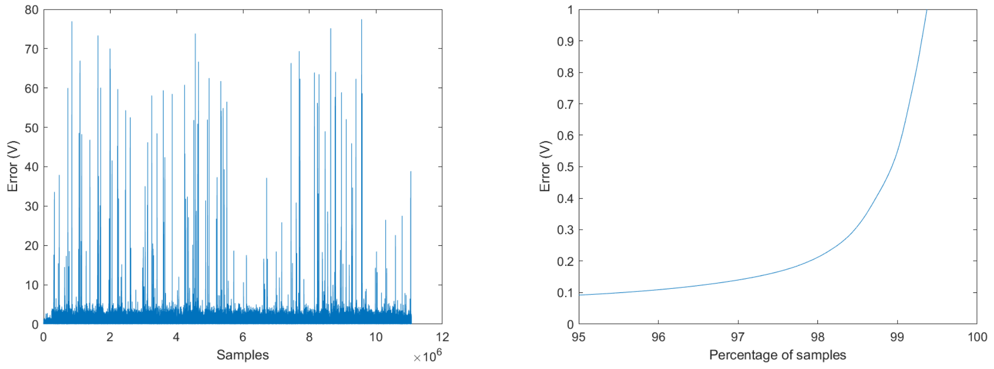

(a) Unsorted error

(b) Sorted error

Fig. A.18.: Error in the linear-fit estimation ξ_3^{AA}

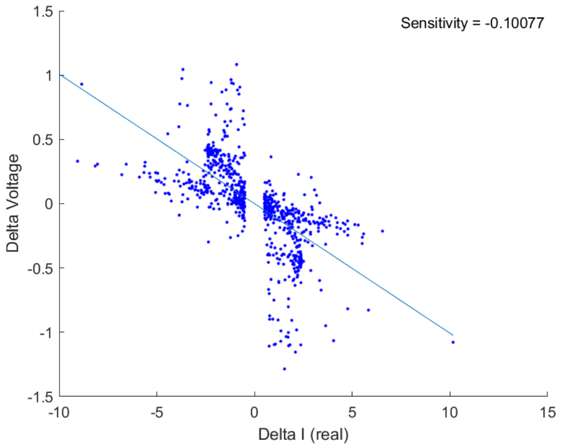

Fig. A.19.: Linear-fit estimation ξ_1^{AB}

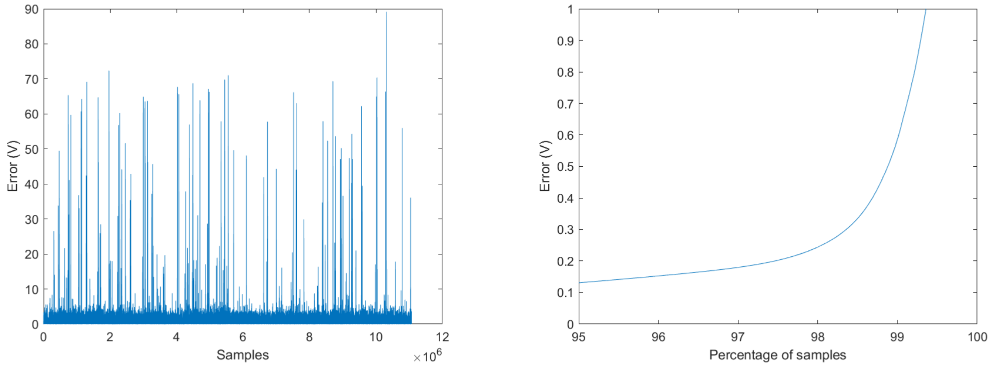

(a) Unsorted error

(b) Sorted error

Fig. A.20.: Error in the linear-fit estimation ξ_1^{AB}

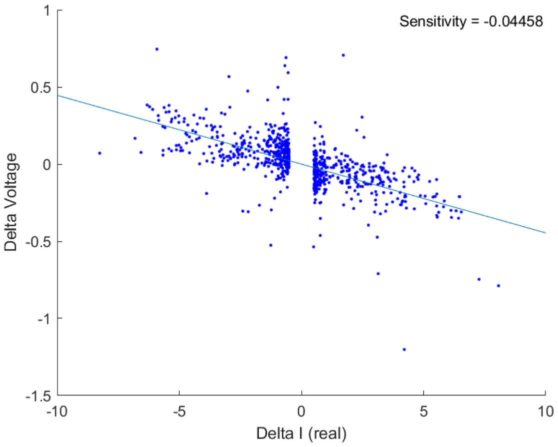

Fig. A.21.: Linear-fit estimation ξ_2^{AB}

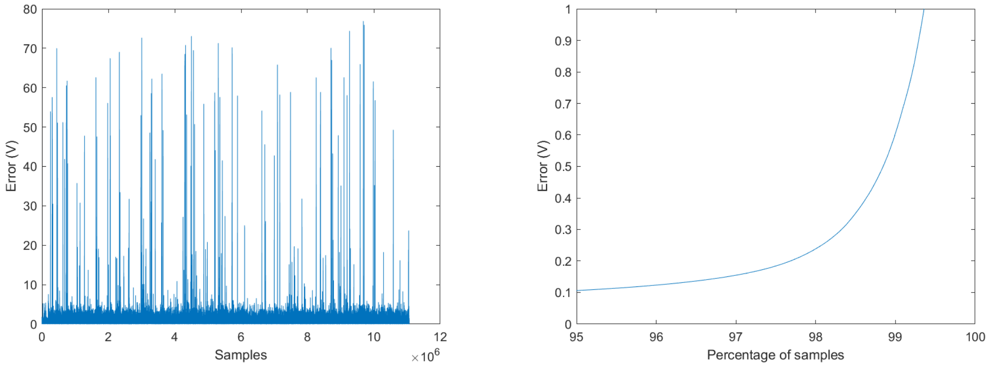

(a) Unsorted error

(b) Sorted error

Fig. A.22.: Error in the linear-fit estimation ξ_2^{AB}

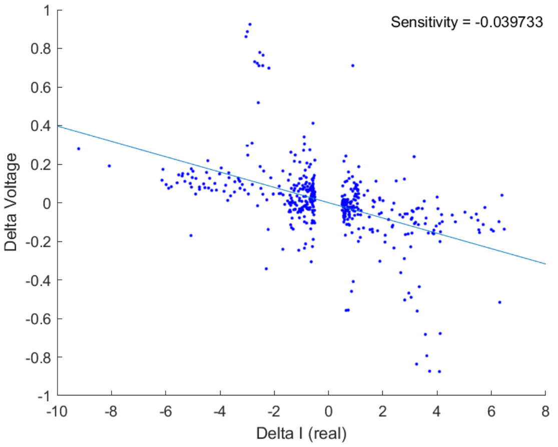

Fig. A.23.: Linear-fit estimation ξ_3^{AB}

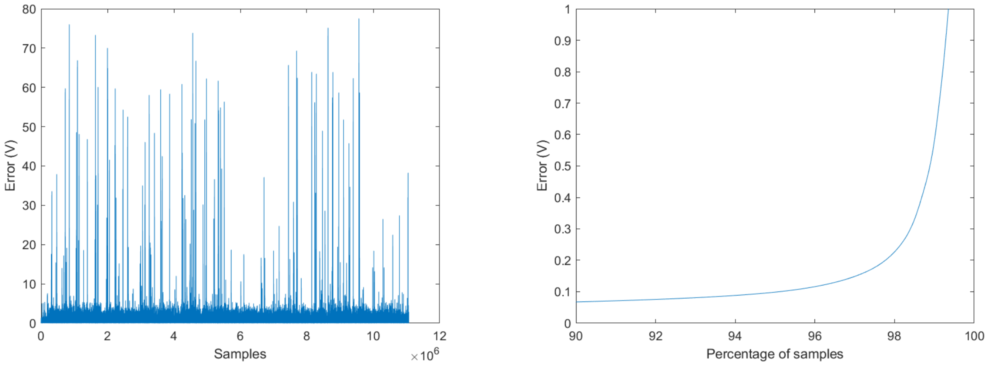

(a) Unsorted error

(b) Sorted error

Fig. A.24.: Error in the linear-fit estimation ξ_3^{AB}

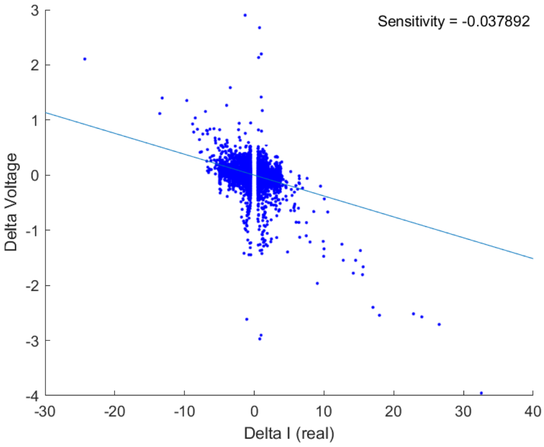

Fig. A.25.: Linear-fit estimation ξ_1^{BA}

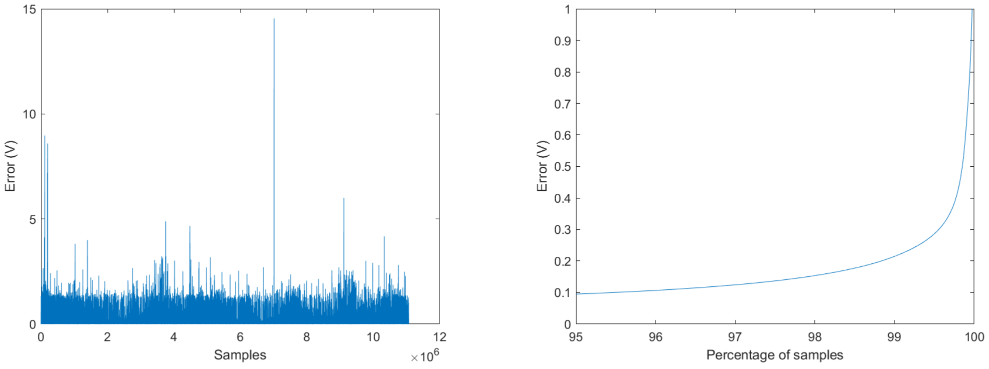

(a) Unsorted error

(b) Sorted error

Fig. A.26.: Error in the linear-fit estimation ξ_1^{BA}

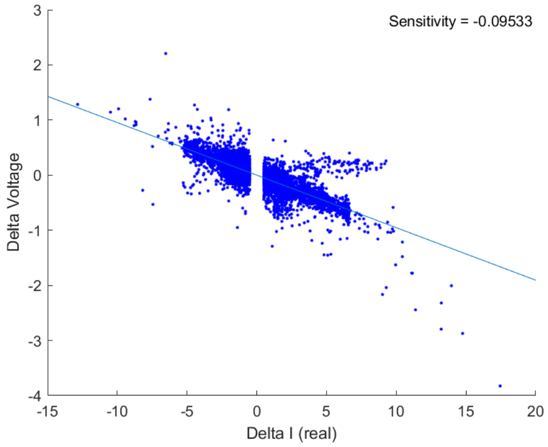

Fig. A.27.: Linear-fit estimation ξ_2^{BA}

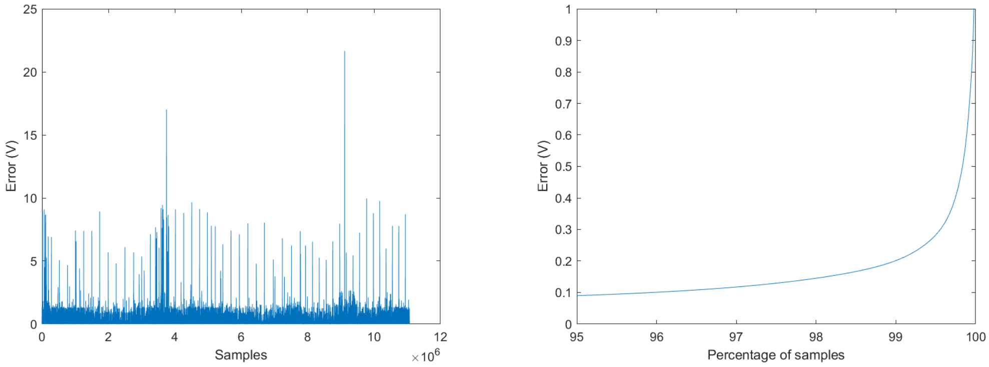

(a) Unsorted error

(b) Sorted error

Fig. A.28.: Error in the linear-fit estimation ξ_2^{BA}

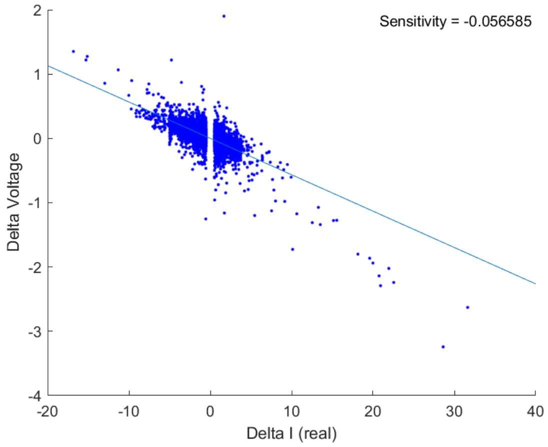

Fig. A.29.: Linear-fit estimation ξ_3^{BA}

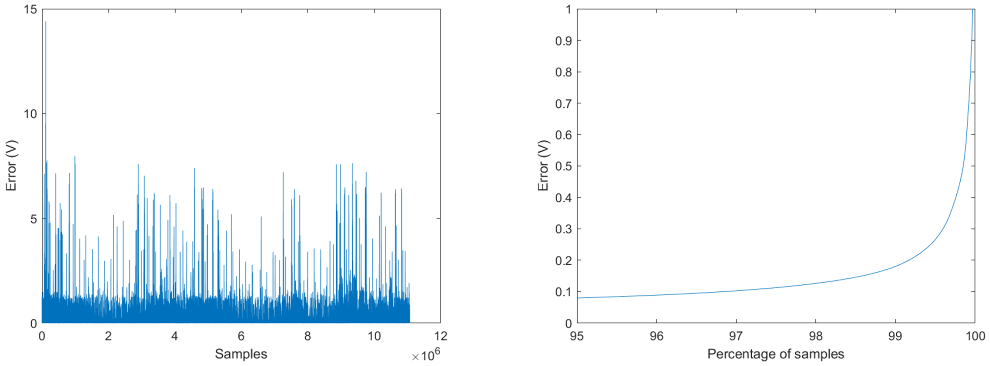

(a) Unsorted error

(b) Sorted error

Fig. A.30.: Error in the linear-fit estimation ξ_3^{BA}

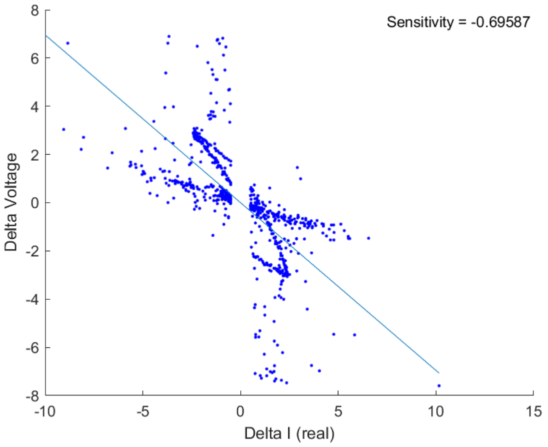

Fig. A.31.: Linear-fit estimation ξ_1^{BB}

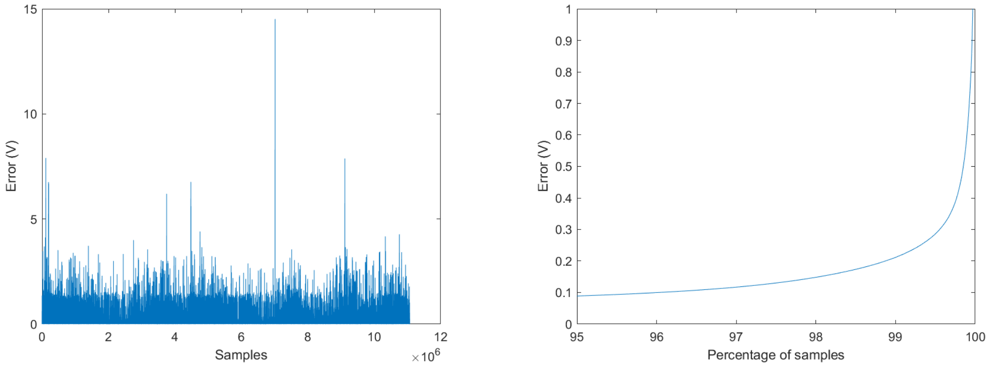

(a) Unsorted error

(b) Sorted error

Fig. A.32.: Error in the linear-fit estimation ξ_1^{BB}

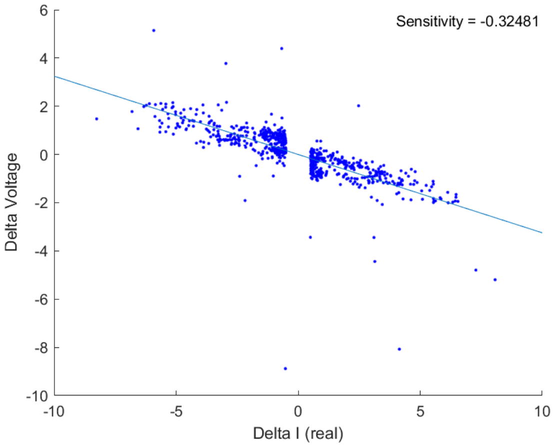

Fig. A.33.: Linear-fit estimation ξ_2^{BB}

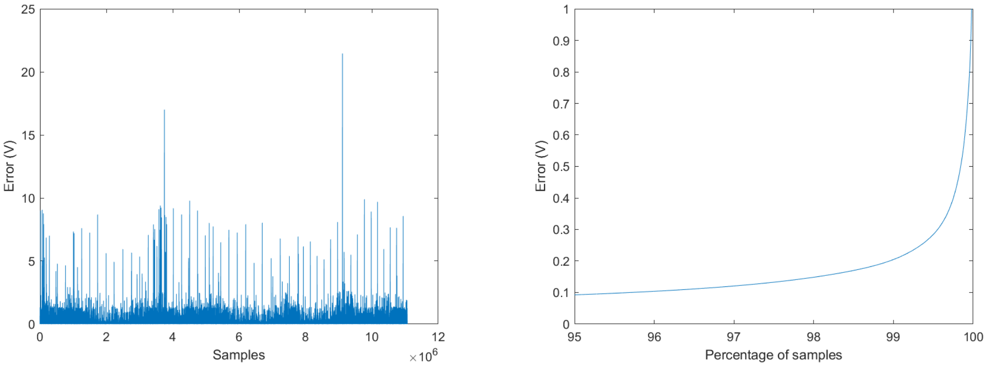

(a) Unsorted error

(b) Sorted error

Fig. A.34.: Error in the linear-fit estimation ξ_2^{BB}

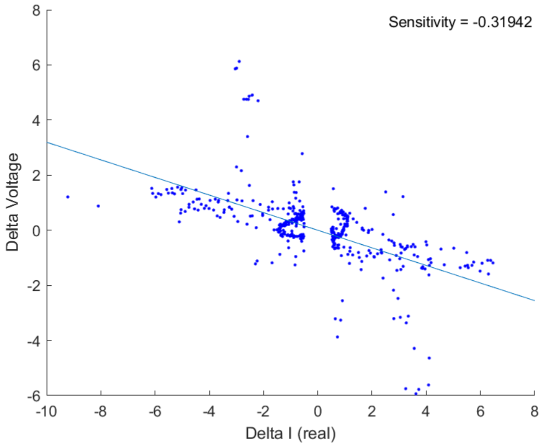

Fig. A.35.: Linear-fit estimation ξ_3^{BB}

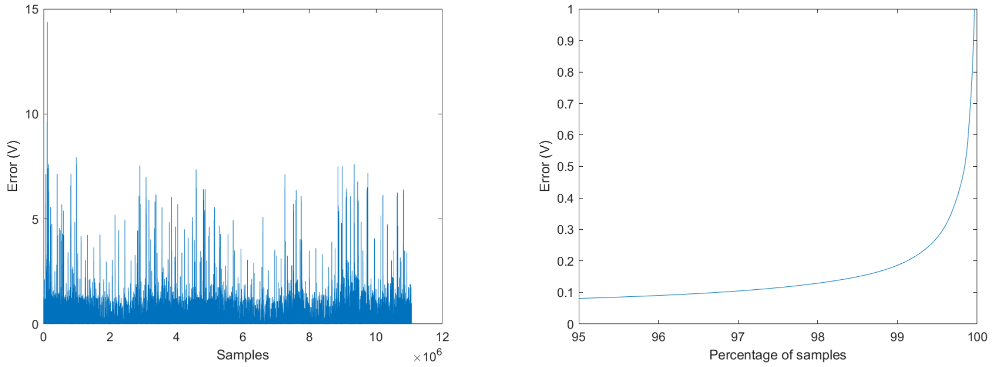

(a) Unsorted error

(b) Sorted error

Fig. A.36.: Error in the linear-fit estimation ξ_3^{BB}

A.3 Online estimator results figures

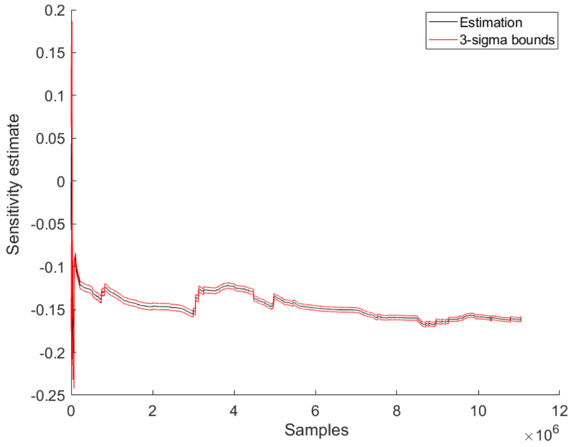

Fig. A.37.: Sensitivity estimate ξ_1^{AA} with 3σ confidence, expected value from cable data: -0.230777

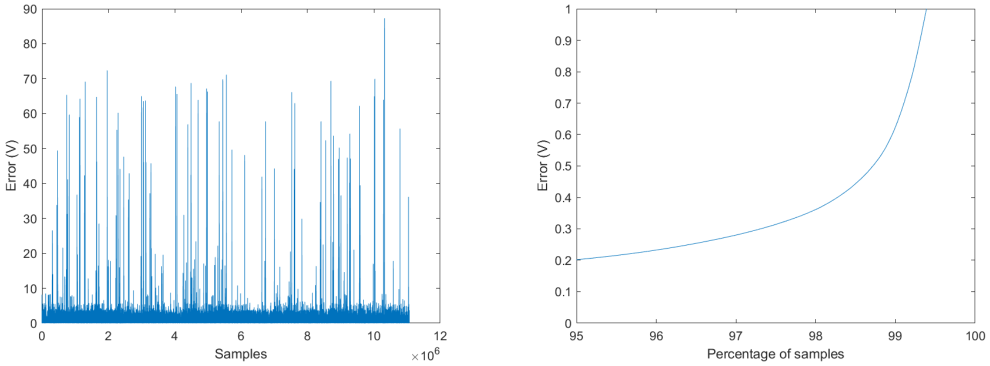

(a) Unsorted error

(b) Sorted error

Fig. A.38.: Error in the online estimation ξ_1^{AA}

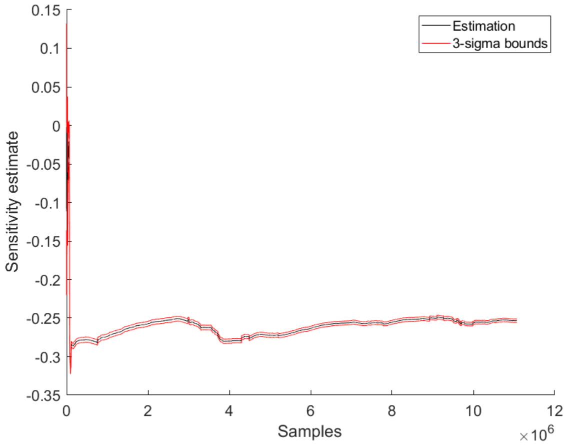

Fig. A.39.: Sensitivity estimate ξ_2^{AA} with 3σ confidence, expected value from cable data: -0.230777

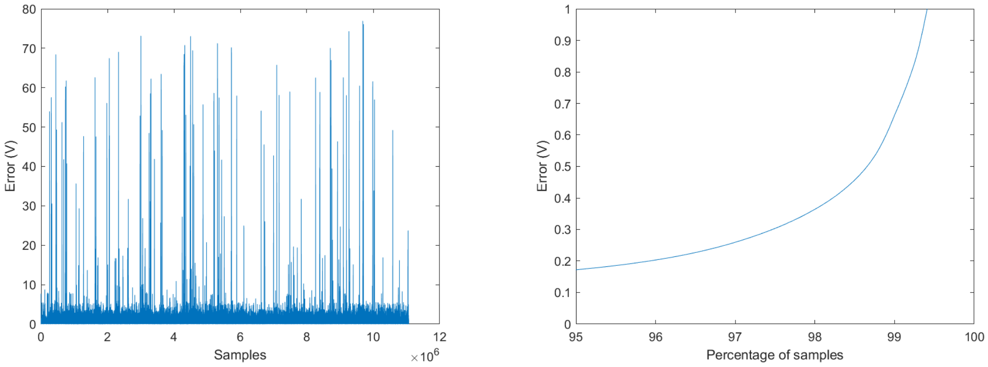

(a) Unsorted error

(b) Sorted error

Fig. A.40.: Error in the online estimation ξ_2^{AA}

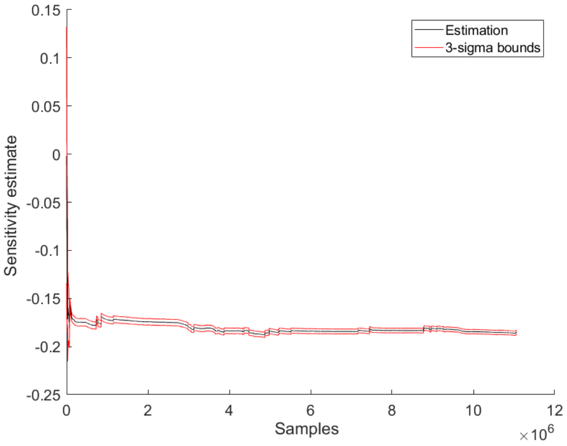

Fig. A.41.: Sensitivity estimate ξ_3^{AA} with 3σ confidence, expected value from cable data: -0.230777

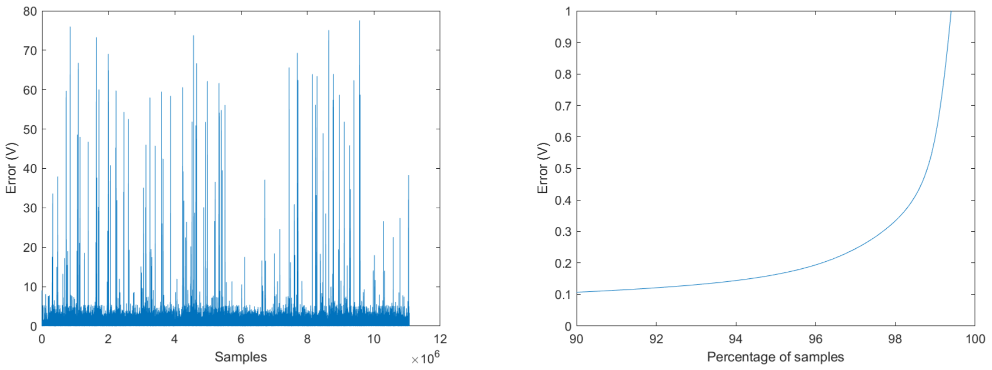

(a) Unsorted error **(b)** Sorted error

Fig. A.42.: Error in the online estimation ξ_3^{AA}

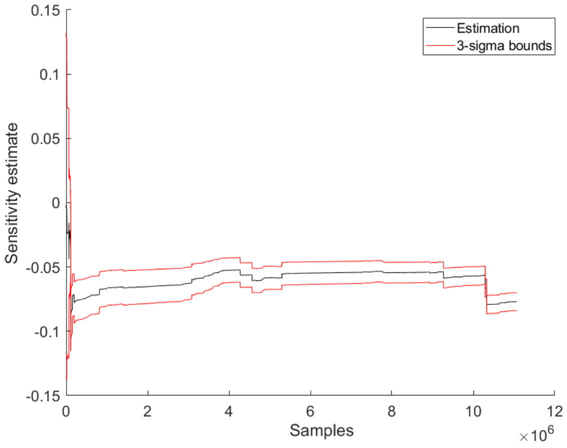

Fig. A.43.: Sensitivity estimate ξ_1^{AB} with 3σ confidence, expected value from cable data: -0.08691

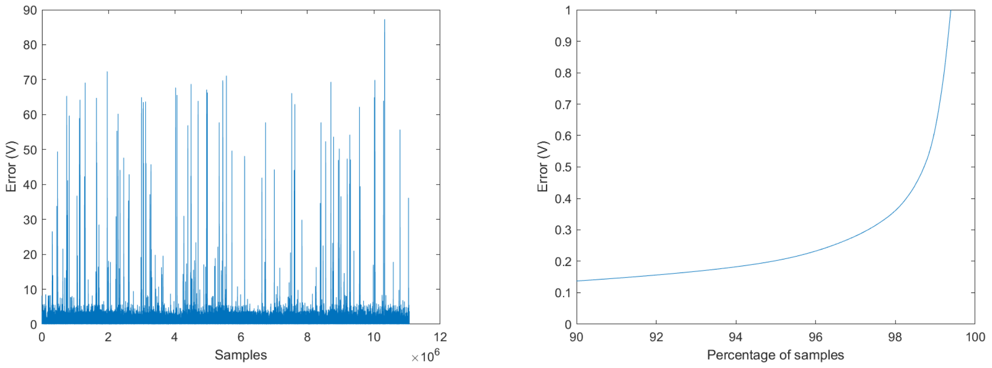

(a) Unsorted error **(b)** Sorted error

Fig. A.44.: Error in the online estimation ξ_1^{AB}

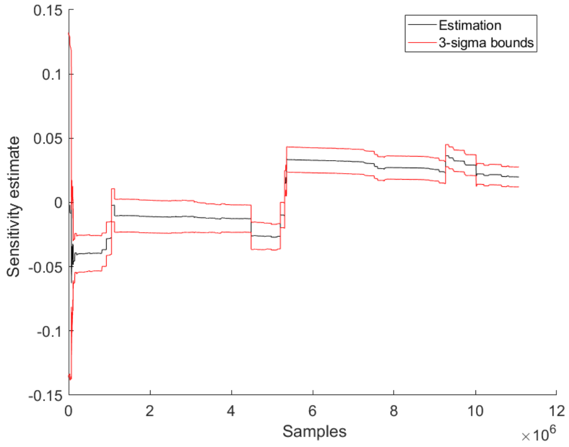

Fig. A.45.: Sensitivity estimate ξ_2^{AB} with 3σ confidence, expected value from cable data: -0.08691

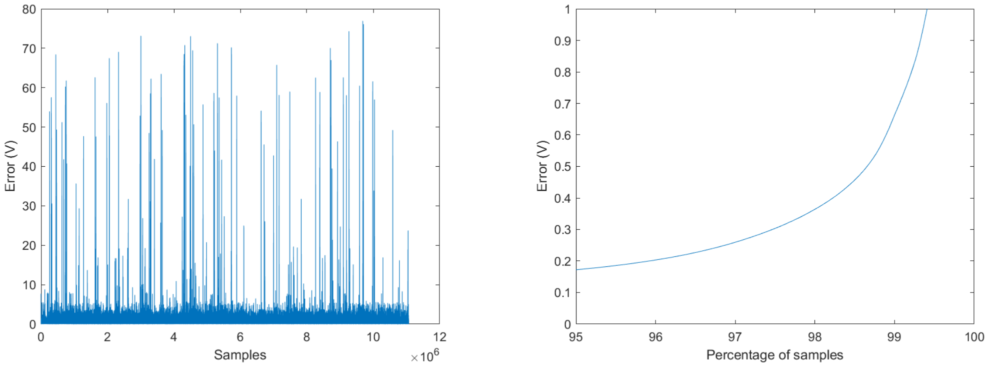

(a) Unsorted error

(b) Sorted error

Fig. A.46.: Error in the online estimation ξ_2^{AB}

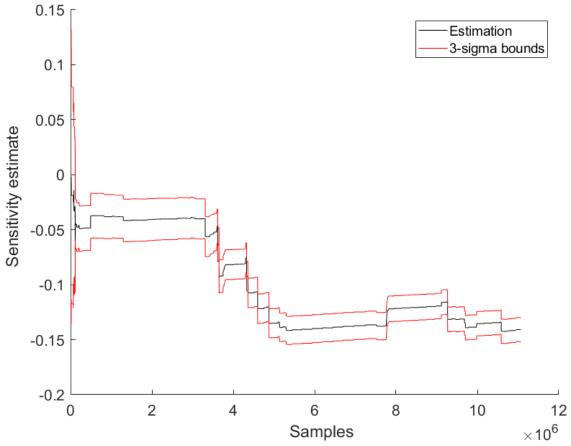

Fig. A.47.: Sensitivity estimate ξ_3^{AB} with 3σ confidence, expected value from cable data: -0.08691

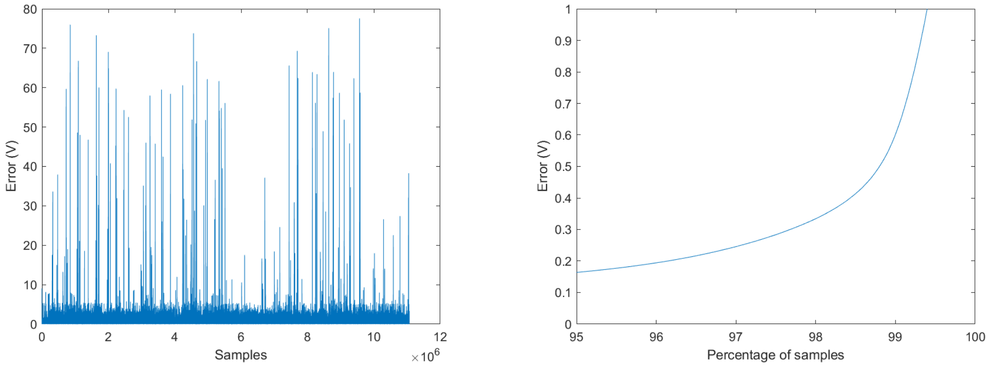

(a) Unsorted error

(b) Sorted error

Fig. A.48.: Error in the online estimation ξ_3^{AB}

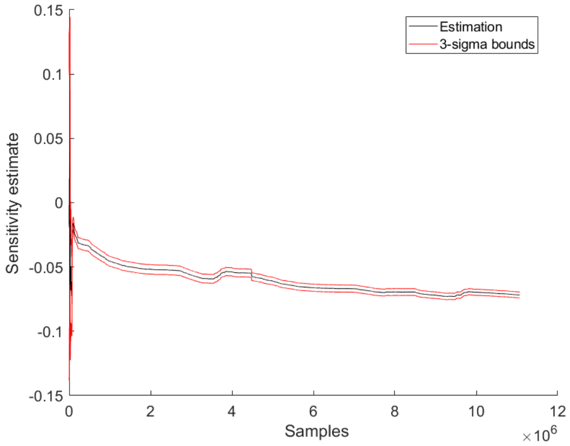

Fig. A.49.: Sensitivity estimate ξ_1^{BA} with 3σ confidence, expected value from cable data: -0.08691

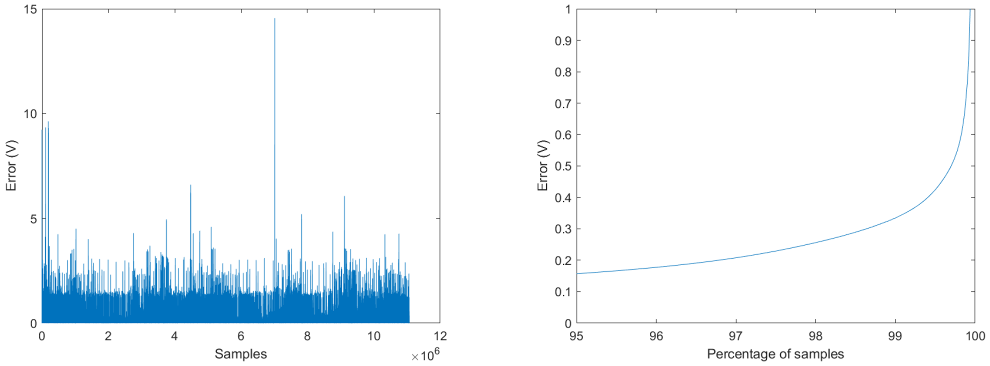

(a) Unsorted error

(b) Sorted error

Fig. A.50.: Error in the online estimation ξ_1^{BA}

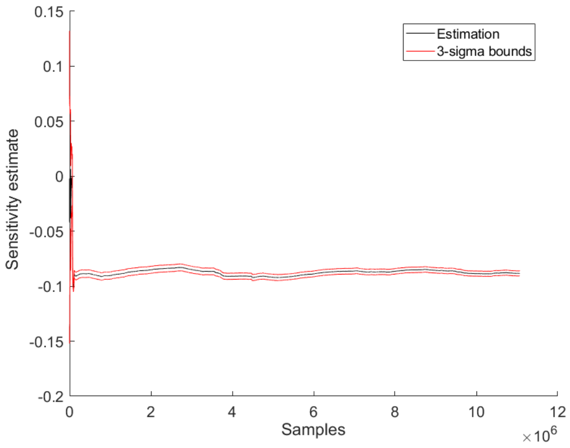

Fig. A.51.: Sensitivity estimate ξ_2^{BA} with 3σ confidence, expected value from cable data: -0.08691

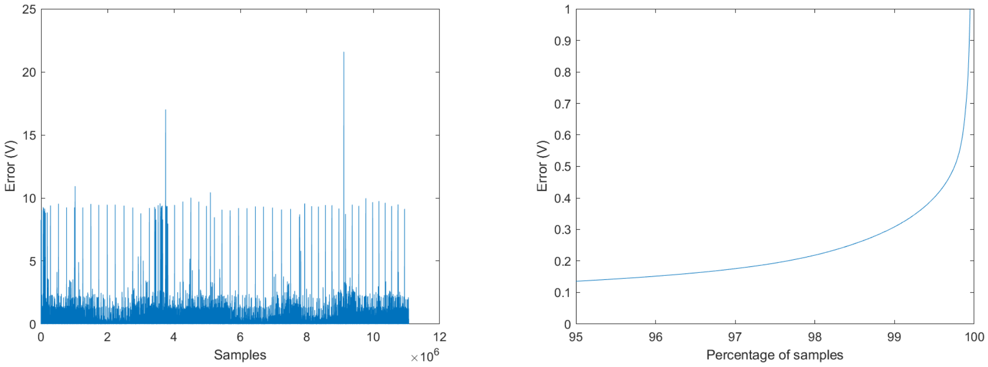

(a) Unsorted error

(b) Sorted error

Fig. A.52.: Error in the online estimation ξ_2^{BA}

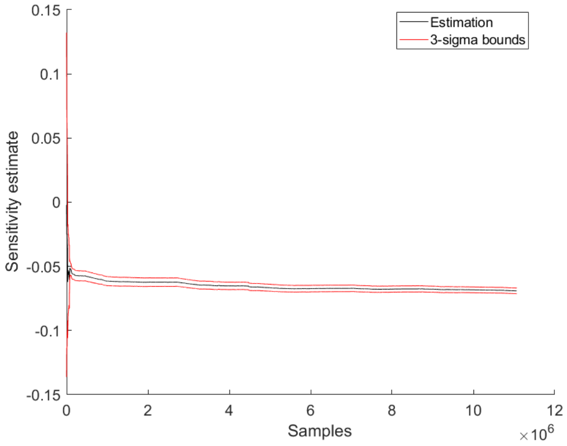

Fig. A.53.: Sensitivity estimate ξ_3^{BA} with 3σ confidence, expected value from cable data: -0.08691

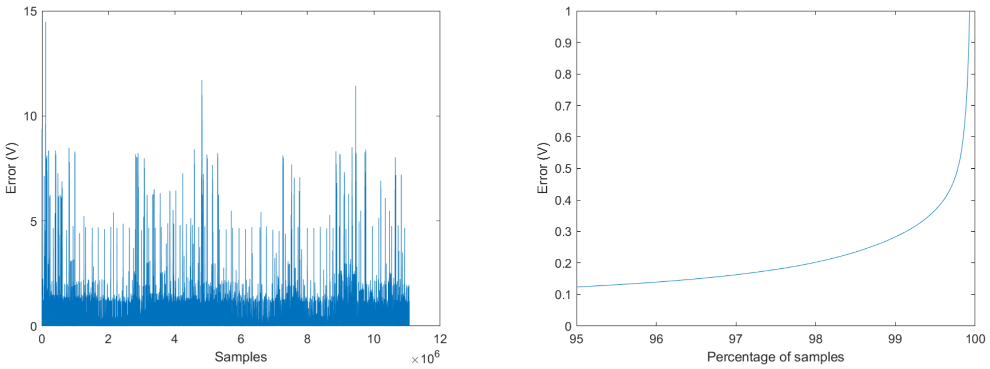

(a) Unsorted error

(b) Sorted error

Fig. A.54.: Error in the online estimation ξ_3^{BA}

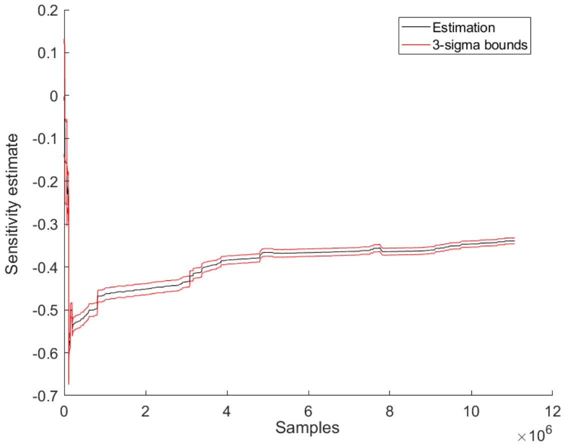

Fig. A.55.: Sensitivity estimate ξ_1^{BB} with 3σ confidence, expected value from cable data: -0.510731

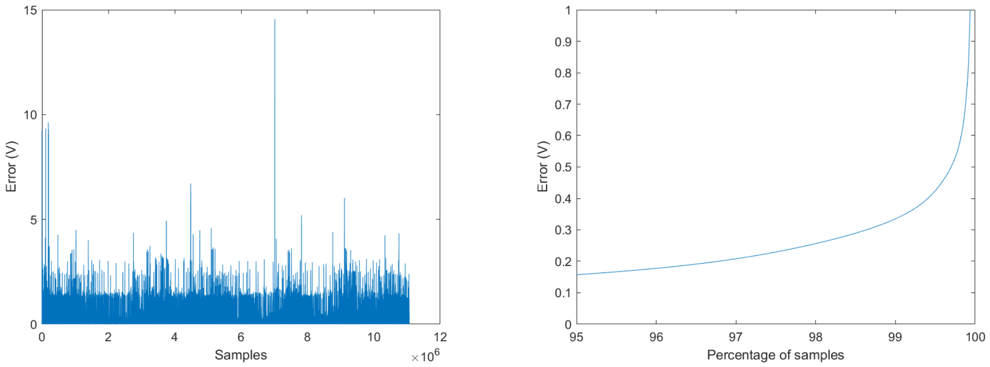

(a) Unsorted error

(b) Sorted error

Fig. A.56.: Error in the online estimation ξ_1^{BB}

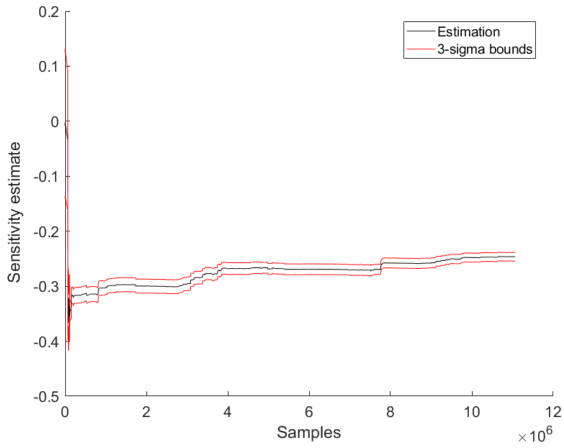

Fig. A.57.: Sensitivity estimate ξ_2^{BB} with 3σ confidence, expected value from cable data: -0.510731

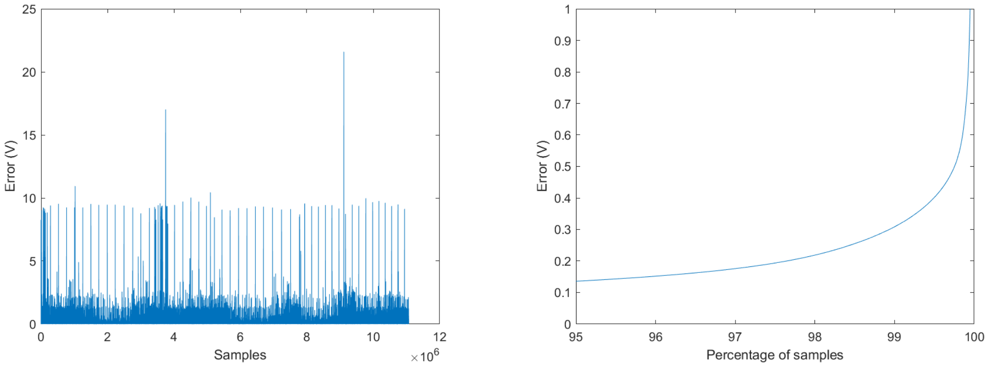

(a) Unsorted error

(b) Sorted error

Fig. A.58.: Error in the online estimation ξ_2^{BB}

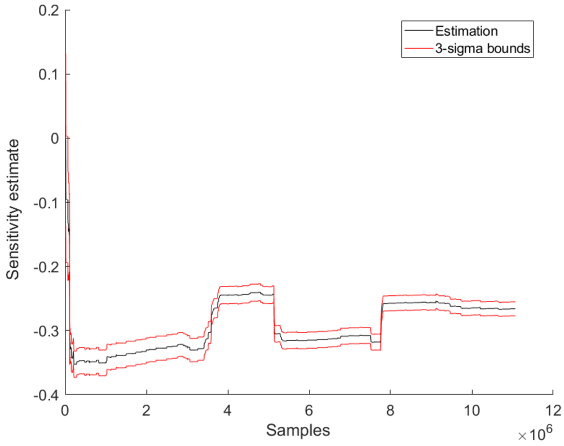

Fig. A.59.: Sensitivity estimate ξ_3^{BB} with 3σ confidence, expected value from cable data: -0.510731

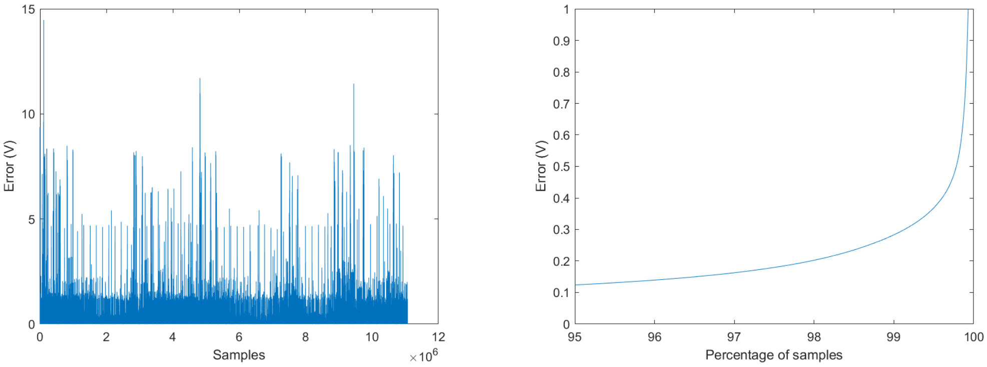

(a) Unsorted error **(b)** Sorted error

Fig. A.60.: Error in the online estimation ξ_3^{BB}

A.4 Errors comparison figures

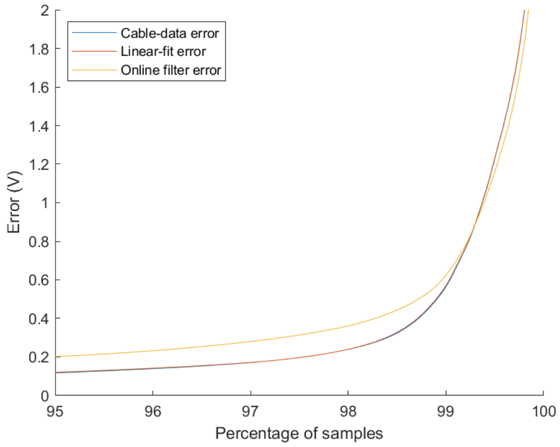

Fig. A.61.: Comparison of the errors for ξ_1^{AA}

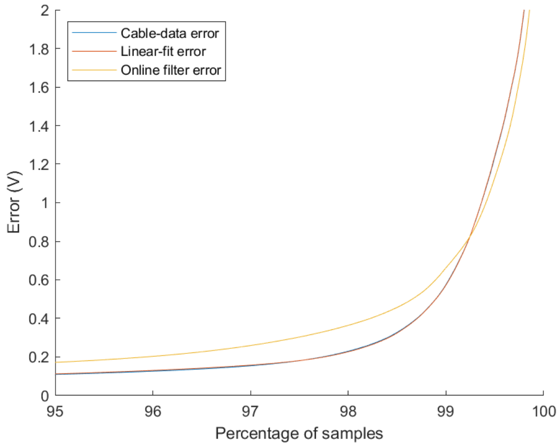

Fig. A.62.: Comparison of the errors for ξ_2^{AA}

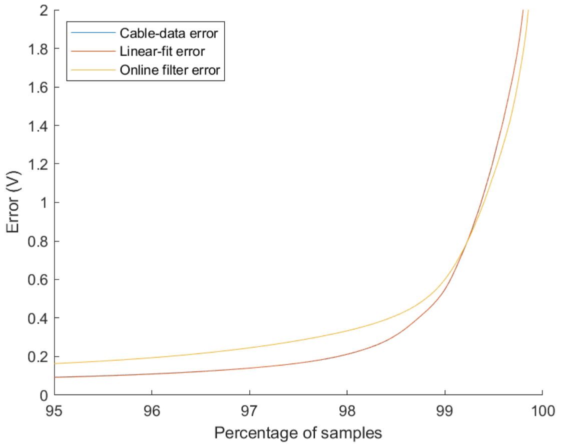

Fig. A.63.: Comparison of the errors for ξ_3^{AA}

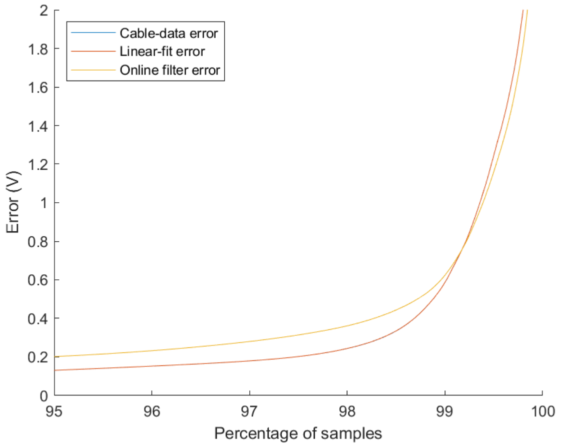

Fig. A.64.: Comparison of the errors for ξ_1^{AB}

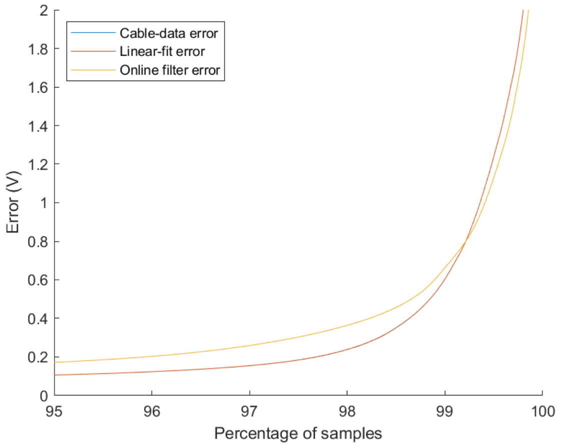

Fig. A.65.: Comparison of the errors for ξ_2^{AB}

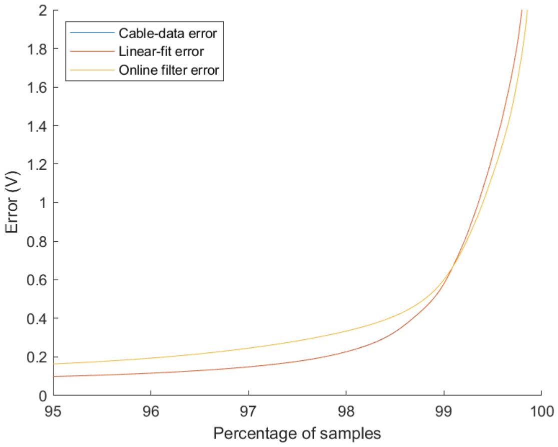

Fig. A.66.: Comparison of the errors for ξ_3^{AB}

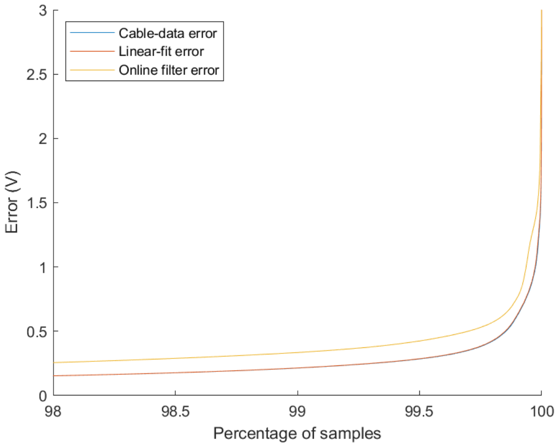

Fig. A.67.: Comparison of the errors for ξ_1^{BA}

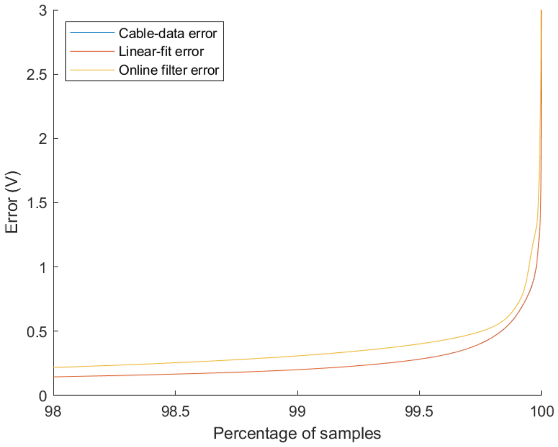

Fig. A.68.: Comparison of the errors for ξ_2^{BA}

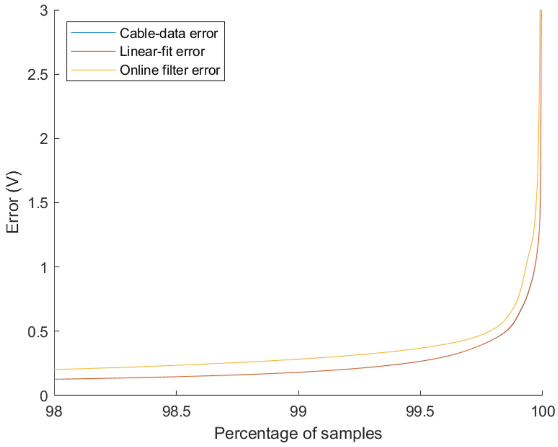

Fig. A.69.: Comparison of the errors for ξ_3^{BA}

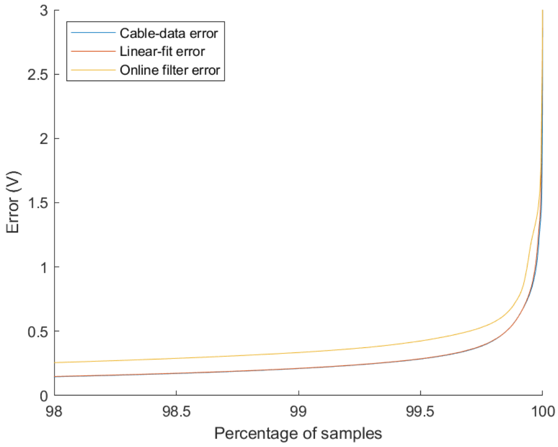

Fig. A.70.: Comparison of the errors for ξ_1^{BB}

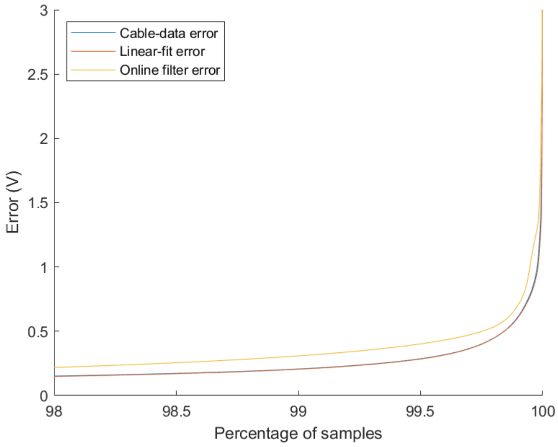

Fig. A.71.: Comparison of the errors for ξ_2^{BB}

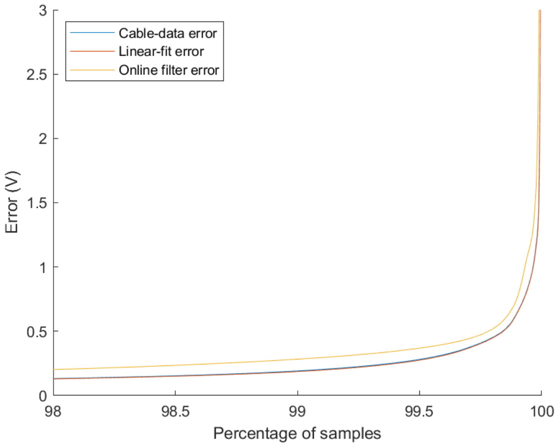

Fig. A.72.: Comparison of the errors for ξ_3^{BB}

Colophon

This thesis was typeset with LaTeX 2$_{\varepsilon}$. It uses the *Clean Thesis* style developed by Ricardo Langner. The design of the *Clean Thesis* style is inspired by user guide documents from Apple Inc.

Download the *Clean Thesis* style at `http://cleanthesis.der-ric.de/`.